UNIVERSITÀ DEGLI STUDI DI BERGAMO

FLOW BOILING OF REFRIGERANTS INSIDE A GLASS MINICHANNEL

Chiara Baldassari
Doctoral Thesis

Dipartimento di Ingegneria
Tesi di Dottorato in Tecnologie per l’energia e l’ambiente

Chiara Baldassari FLOW BOILING OF REFRIGERANTS INSIDE A GLASS MINICHANNEL

ISBN: 978-88-97413-07-3

UNIVERSITÀ DEGLI STUDI DI BERGAMO
Dipartimento di Ingegneria

DOTTORATO DI RICERCA
IN
TECNOLOGIE PER L’ENERGIA E L’AMBIENTE
Tecnologie per l’Energia e l’Ambiente

XXVI Ciclo

Anno 2013

BOILING OF REFRIGERANTS INSIDE A GLASS MINICHANNEL

Doctoral Thesis:

Chiara Baldassari

Supervisor:

Prof. Marco Marengo

Università degli studi di Bergamo. Dipartimento di Ingegneria.
ISBN 978-88-97413-07-3

CONTENT LIST

ACKNOWLEDGEMNTS

First of all, my special thanks are for Prof. Marco Marengo who brightly guided me through the “boiling world” with perseverance, dedication and optimism. Thanks to my family who always support me during these years and especially to Roberto, who hasn’t stop yet to believe and be involved in my multitasking projects. I spent my working time in the Thermal Physics Lab with nice people who always try to help and encourage me; thank you for your availability and kindness and a particular thanks to Mauro, my boss-friend, and Carlo. Make a PhD, and in particular write the PhD thesis, taking care of two children is a demanding experience that “ segna e insegna” (italian joke of words that mean “marks and teaches”). So this thesis has to be dedicated to Marianna and Alessandro, my lovely mini-daughter and micro-son.

NOMENCLATURE

A = Cross sectional area of the pipe [m^2]
Bl = boiling number [-]
Bo = Bond number [-]
Ca = capillarity number [-]
C_D = drag coefficient [-]
c_p = specific heat at constant pressure [J/kg·K]
CHF = critical heat flux [W/m^2]
Cn = convection number [-]
Co = confinement number [-]
d = diameter [m]
D^2 = cross-sectional area of a microchannel [m^2]
D_{hH} = hydraulic diameter based on the heated perimeter, see footnote 23 [m]
Eo = Eötvös number [-]
F = force [N]
fp = triplet frequency [Hz]
g = gravitational acceleration [m/s^2]
G = mass flux [kg/m^{2}s]
Ga = Garimella number, convective confinement number [-]
H = height [m]
h = heat transfer coefficient [W/m^{2}K]

HTC = heat transfer coefficient [W/m^{2}K]
h_{LV} = latent heat of vaporization [J/kg]
j = superficial velocity [m/s]
k = thermal conductivity [W/mK]
K_{emp} = empirical constant [-]
K_1 = Kandlikar first number [-]
K_2 = Kandlikar second number [-]
L = characteristic dimension [m]
l_c = capillary length [m]
l_{drag} = drag length [m]
L_H = axial heated length [m]
p = pressure [Mpa]
P = the total power supplied to the heaters [W]
P' = heat input from unit of length [W/m]
Pf = the net power supplied to the fluid [W]
Pr = Prandtl number [-]
q = mass flow rate [kg/s]
q'' = heat flux [W/m^2]
r = radius [m]
R^2 = linear correlation coefficient
Re = Reynolds number [-]
T = temperature [K]
u = mean velocity [m/s]
We = Weber number [-]
x = vapor quality [-]

Greek

α = thermal diffusivity [m^2/s]
δ_0 = initial thickness of liquid film [m]
δ_{min} = minimum thickness of liquid film [m]
ΔTsh = wall superheat [°C]
ε = void fraction
θ = contact angle [°]
π = pi greco [-]
ρ = density [kg/m^3]
σ = surface tension [N/m]

μ = dynamic viscosity [Pa·s]
μg = microgravity [m/s^2]
ν = kinematic viscosity [m^2/s]

Subscripts

adh = adhesion
adv = advancing
b = bubble
b,critical = bubble, critical
F = fluid
h = hydraulic
i = phase i
in = inlet
L = liquid
LO = total flow (liquid plus vapor) assumed to flow as liquid
LV = liquid vapor
rec = receding
s = surface conditions
sat = saturated conditions
sub = subcooled
th = threshold
V = vapor
VO = total flow (liquid plus vapor) assumed to flow as vapor
W = wall
win = internal of the heated wall

Chapter 1

Introduction

In many industrial applications, two-phase flows are used for heavy-duty and reliable cooling and heating processes. The boiling phenomena are essential for evaporator heat exchangers, such as for refrigerators and electronic cooling. In fact, increased calculation processing speed, miniaturization and higher packing densities of electronic processing chips and higher system performance has lead to the development of high power and high heat flux that require a new, accurate and important thermal management. Convective boiling and two-phase flow heat transfer in microchannels can satisfy this demand and they become dominant parameters in the performance of cooling systems for electronic devices, highly efficient compact heat exchangers, fuel cell and advanced phase-change heat sink systems. In space applications the use of passive thermal components, such as heat pipes, loop heat pipes and future pulsating heat pipes, and active components such miniaturized pumped systems, makes very important the understanding of the flow boiling mechanisms, in order to simulate precisely the heat transfer conditions in satellites and in thermal components for extraplanetary exploration.

Even if the study of boiling is a standard research since a century, there are many aspects that are still under discussion, especially for forced convection boiling in small tubes. The research needs further experimental data for flow patterns, heat transfer coefficients and for the validation of the boiling models.

This work is divided into two parts to follow the real work that has been done during the PhD. The point to focus on at the beginning of the PhD was to critically investigate the state of the art of forced convective boiling and after that there would be the second part corresponding to the experiments. Part I is a critical review on microchannel and microgravity that wants to answer to the necessity to define in the most complete way the status-of-the-art of such an important research field and to critically investigate the successes and the weaknesses of the current scientific literature. The idea to consider the channel microsize together with the microgravity effects in a single review is due to the fact that the transition between confined and unconfined bubble flows may be defined using dimensionless numbers, such as the Eötvös number $Eo = g\left(\rho_L - \rho_V\right)L^2/\sigma$ and its analogues, which are at the same time linked to the tube diameter and the gravity forces. In fact the Eötvös number tends to zero either when the gravity tends to zero or when the tube diameter tends to zero, but physical phenomena appear different considering separately either only the tube size or only the microgravity condition. This part I points out that some literature results are still incongruous and that the global picture of boiling process remains still unclear. Part II contains the experimental investigation of boiling and in particular of onset of nucleate boiling in a glass minichannel using two different refrigerants, R-134a and R-245fa. The original idea was to characterize boiling in a 4 mm internal diameter channel and, after that, to repeat all the experiments using the 1 mm internal diameter channel in order to characterize what it is changing going down with the dimensions according to the critical informations from Part I. During the experimental activity some new interesting trends appeared, linked to the nucleation that always starts from the upper side of the heater and only later from the lower side of the heater. Because of this, new experiments were necessary to investigate the heterogeneous non-uniform boiling of refrigerants inside the glass minichannel and so the experimental section, Part II of this thesis, doesn’t include tests on flow boiling in a glass microchannel. The incipient boiling process, i.e. the analysis of the flow characteristics for very low values of the vapour quality, was investigated thanks to the transparent ITO heater that allow the visualization of the boiling process, such as bubble nucleation, bubble growth, departure and bubble lift-off.

The range of the flow parameters of the results presented in this thesis are: mass flow rate between 50 and 137 kg/m^2 s, the heat flux up to 26 kW/m^2 and the inlet temperature range of the fluid is 18-21° C for R-134a and 25-28° C for R-245fa.

1.1 SUMMARY OF THE THESIS

A brief description of the contents of the chapters that follow is given below:

Chapter 1: introduction.

PART I

Chapter 2: is an overview on non-dimensional numbers employed in two phase flow studies. Maps of the dimensionless number ranges spanned by the literature data in microchannels and microgravity are given.

Chapter 3: it is a review on the micro to macroscale transition criteria; they are compared. A new consideration on the effect of wettability is introduced together with the concept of a “drag length”, i.e. a scale to define when the drag forces can move the growing bubbles from a boiling surface. This number could be particularly interesting for microgravity experiments

Chapter 4: is the state of the art of boiling in microchannel, starting from the mechanisms, going through the models and then to the heat transfer coefficient and flow patterns and maps.

Chapter 5: is the state of the art of boiling in microgravity with a comparison between experiments made in microgravity and terrestrial gravitycharacterized by the same Eötvos number.

PART II

Chapter 6: describes the experimental setup, procedure, data acquisition and post processing elaboration.

Chapter 7: it is a resume on the R-134a experimental analysis, presenting the boiling curves, the flow patterns and heat transfer coefficient obtained.

Chapter 8: it is a resume on the experiments performed with R-245fa; there are the boiling curves and the associated flow patterns and heat transfer coefficients. A comparison among the HTC of the two refrigerants is presented.

Chapter 9: presents the general conclusions and the future works.

PART I: CRITICAL REVIEW

Chapter 2

On non dimensional numbers relevant to two phase flow studies in microchannel and microgravity

The purpose is first to classify, from the point of view of non-dimensional groups, the state of the art of the literature regarding microchannels and microgravity, both characterized from having a low Eötvös number. This review focuses on works done on phase change of a single component fluid and characterized by small Eötvös numbers ($Eo = g(\rho_L - \rho_V)L^2/\sigma < 5$), i.e. small diameters and/or low gravity environment.

The most important dimensionless parameters in phase change heat transfer are listed in section 2.1, while in 2.2 the ranges of the non-dimensional parameters employed in this review are given. Since many papers are using different symbols a great effort to homogenise the various nomenclatures has been done.

2.1 NON DIMENSIONAL NUMBERS RELEVANT TO TWO-PHASE FLOW STUDIES IN MICROCHANNELS

In the following definitions, the velocity is considered as the superficial velocity that is, for the phase *i* [1]: $j_i = \dfrac{q_i}{\rho_i A}$. The superficial velocity of the liquid, j_L, is defined as the ratio of the volumetric flow rate of the liquid phase and the total cross sectional area of the two-phase flow, obtaining $j_L = \dfrac{G}{\rho_L}(1-x)$. In the same way, the superficial velocity of the vapour, j_V, is: $j_V = \dfrac{G}{\rho_V}x$. Also the cross-sectional void fraction e, defined as the ratio between the mean area of the section occupied by the vapour divided by the total tube cross section, $\varepsilon = \dfrac{A_V}{A}$, will be considered.

The non-dimensional numbers relevant to two-phase studies in microchannels are summarized in Table 1.

Non dimensional number	Significance
Boiling number $Bl = \frac{q''}{Gh_{LV}}$	It represents the ratio of the evaporation mass flux to the total mass flux flowing in a channel [3].
Bond number $Bo = \frac{g(\rho_L - \rho_V)d_h{}^2}{\sigma}$	Ratio between gravity and surface tension forces[1].
Capillarity number $Ca = \frac{\mu_L j_L}{\sigma} = \frac{\mu_L G(1-x)}{\rho_L \sigma}$, $Ca_{LO} = \frac{\mu_L G}{\rho_L \sigma}$	Ratio of viscous to surface tension forces
Confinement number $Co = \left[\frac{\sigma}{g(\rho_L - \rho_V)d^2{}_h}\right]^{\frac{1}{2}}$	Ratio between surface tension forces and gravity.
Convection number $Cn = \left[\frac{1-x}{x}\right]^{0.9} \cdot \left[\frac{\rho_V}{\rho_L}\right]^{0.5}$	Modified Martinelli parameter, introduced by Shah [2] in correlating flow boiling data

---

[1] The practical difference between *Bo* and *Eo* is that in the definition of Bo the hydraulic diameter, d_h, is used while in the definition of Eo, L is d_h but also another relevant physical dimension, as underlined in section 2.1.1.

Eötvös number $Eo = \frac{g(\rho_L - \rho_V)L^2}{\sigma}$	Ratio between gravity and surface tension forces
Garimella number – convective confinement number $Ga = Bo^{0.5} \times \mathrm{Re}_{LO}$	Weighted ratio between gravity dot inertia forces and surface tension dot viscous forces
Jakob number $Ja = \frac{c_p(T_s - T_{sat})}{h_{LV}}$	Ratio of sensible to latent energy absorbed during liquid-vapor phase change.
Kandlikar first number $K_1 = \frac{\left(\frac{q''}{h_{LV}}\right)^2 \frac{d_h}{\rho_V}}{\frac{G^2 d_h}{\rho_L}} = \left(\frac{q''}{G h_{LV}}\right)^2 \frac{\rho_L}{\rho_V} = \frac{Bl^2 \rho_L}{\rho_V}$	It represents the ratio of the evaporation momentum force and the inertia force [3].
Kandlikar second number $K_2 = \frac{\left(\frac{q''}{h_{LV}}\right)^2 \frac{d_h}{\rho_V}}{\sigma} = \left(\frac{q''}{h_{LV}}\right)^2 \frac{d_h}{\rho_V \sigma}$	It represents the ratio of the evaporation momentum force and the surface tension force [3].
Prandtl number $\mathrm{Pr} = \frac{\nu}{\alpha}$	Ratio between kinematic viscosity and thermal diffusivity.

Reynolds number $\mathrm{Re}_L = \frac{\rho_L j_L d_h}{\mu_L} = \frac{G(1-x)d_h}{\mu_L}$ $\mathrm{Re}_{LO} = \frac{G d_h}{\mu_L}$ $\mathrm{Re}_V = \frac{\rho_V j_V d_h}{\mu_V} = \frac{G x d_h}{\mu_V}$ $\mathrm{Re}_{VO} = \frac{G d_h}{\mu_V}$	Ratio of inertia and viscous forces
Weber number $We_L = \frac{\rho_L j_L^2 d_h}{\sigma} = \frac{G^2(1-x)^2 d_h}{\rho_L \sigma}$ $We_V = \frac{\rho_V j_V^2 d_h}{\sigma} = \frac{G^2 x^2 d_h}{\rho_V \sigma}$ $We_{LO} = \frac{G^2 d_h}{\rho_L \sigma}$ $We_{VO} = \frac{G^2 d_h}{\rho_V \sigma}$	Ratio of the inertia to the surface tension forces

Table 1 Non dimensional numbers relevant to two-phase studies in microchannels

2.1.1 On the Eötvös number

In the definition of the Eötvös number (Table 1) the characteristic dimension L could be the diameter of the tube or any other physically relevant parameter [3] for the channel size. It is worth noting that in the case of noncircular tubes, Eo is often defined by replacing L with the hydraulic diameter. Given the fact that L should be the characteristic dimension in the direction of the gravitational force - since the Eo number represents the ratio between the buoyancy and the capillary forces - it should be worth to understand in future experiments whether the hydraulic diameter is really the right dimension to consider. For example, for a channel having a rectangular section with length T and width s and inclined at an angle q from the vertical direction, as in Figure 1, the size dimension is $L = \min\left(\frac{s}{\sin\theta};T\right)$ looking at the possible maximum size of the bubbles in gravity direction. If θ is 0°, L becomes equal to T, while if θ is 90°, L is equal to s.

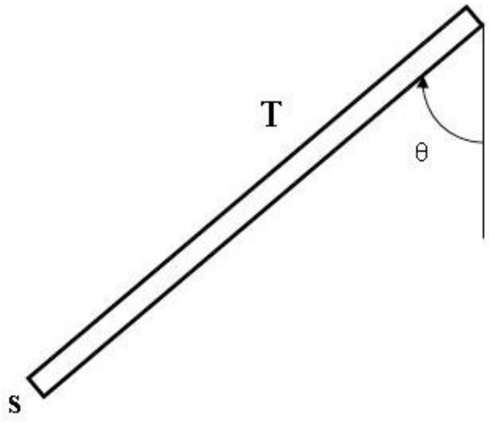

Figure 1 A rectangular channel section, with length T and width s, *inclined at* an angle θ with respect to gravity

In the work of Ravigururajan et al. [4] R-124a is used as test fluid at saturation pressure of 0.3 MPa in a channel size of 270 μm width and a depth of 1000 μm, resulting in a hydraulic diameter of 475 μm. The corresponding Eötvös number is 0.23. If the dimension in the gravity direction, i.e. 1000 μm, is used instead of the hydraulic diameter, the corresponding Eötvös number becomes 1.26, that is 6 times bigger than the value obtained before.

Luciani et al. [5,6] used three different hydraulic diameters: 0.49 mm, 0.84mm, 1.18 mm in their experiments and the corresponding

Eötvös numbers at 0.082 MPa are 1.25 x 10^{-3}, 3.67 x 10^{-3}, 7.25 x 10^{-3}. The dimensions of the minichannel are: 50 mm long, 6 mm wide and the depths, in the gravity direction, are 254 μm, 452 μm or 654 μm corresponding to the three different hydraulic diameters. Considering the three different values of deptht, the corresponding Eötvös number at 0.082 MPa are 3.36 x10^{-4}, 1.06 x 10^{-3}, 2.23 x 10^{-3}, that are 3 times lower than the Eötvös number calculated using the hydraulic diameters.

2.1.2 On the Weber number

Being the Weber number the ratio between inertia and capillary forces, it aims to represent the interaction between vapor and liquid phases and therefore it should be properly defined using the difference between the averaged liquid velocity[2] and the vapor velocity [7], obtaining:

$$We_{LV} = \frac{\rho_L (u_L - u_V)^2 d_h}{\sigma} = \frac{\rho_L d_h G^2}{\sigma} \left[\frac{1}{\rho_L} \left(\frac{1-x}{1-\varepsilon} \right) - \frac{1}{\rho_V} \left(\frac{x}{\varepsilon} \right) \right]^2$$

Unfortunately, in two-phase flow experiments the void fraction ε is seldom declared and therefore further experiments are necessary in order to understand the role of Weber number in flow boiling. The problem related to the lack of data on void fraction in many papers is a serious weakness for a robust comparison of the experimental results in microchannels.

---

[2] u is the mean velocity of an individual phase and is given by the volumetric flow rate of the phase considered over the cross sectional area occupied by each phase, obtaining $u_V = \frac{\dot{Q}_V}{A_V} = \frac{Gx}{\varepsilon \rho_V}$ and

$$u_L = \frac{\dot{Q}_L}{A_L} = \frac{G(1-x)}{\rho_L (1-\varepsilon)}$$

2.1.3 On the Kandlikar numbers

Kandlikar [3] reviewed the existing groups commonly applied in two-phase and boiling applications and introduced two new non-dimensional groups as relevant for the flow boiling in microchannels K_1 and K_2 *(*Table 1).

A higher value of K_1 indicates that the evaporation momentum forces are dominant and are likely to alter the interface movement. For the heat transfer mechanisms, Kandlikar [3] asserted that, from experimental data, the higher values of K_1 correspond to the nucleate boiling dominant region while the K_1 lower values indicate the convective boiling dominant region, as pictured in Figure 2. Since the ratio of liquid and vapour density is always bigger than 1, the lowest value of K_1 corresponds to the lowest value of B_l, obtained when the G value is maximum.

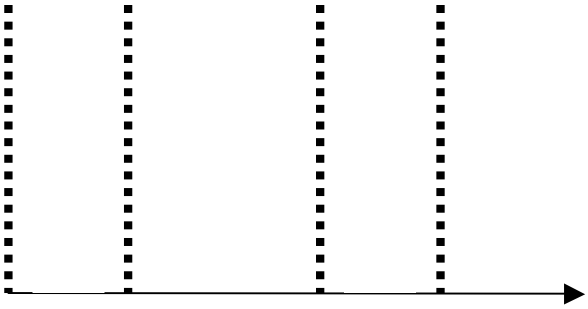

Figure 2 Heat transfer mechanisms *as a* function of the K_1 value [3]

In authors' opinion, Figure 2 is not correct and K_1 it is not able to properly describe the effect of heat transfer. The debate about which mechanism dominates the two-phase flow heat transfer is still open, but it is standardly accepted that the transition from nucleate boiling to convective boiling is linked also to vapor quality and K_1 alone does not include such parameter. For example in Yen et al. [42] bubble nucleation only occurred when $x < 0.4$, hence $x = 0.4$ is to be considered a critical vapor quality to distinguish between nucleate and convective boiling in microchannels. Looking at the K_1 values associated to [42], the range is $1.3*10^{-5}<K_1< 8.32*10^{-4}$, depending on G range (100 kg/(m^2s)<G<800 kg/(m^2s)), and only convective boiling should be observed. In Bao et al. [40] nucleate boiling always dominates, even if the range of K_1 is quite broad, going from $1.6*10^{-8}$ to $7*10^{-2}$, depending on G range (50 kg/(m^2s)<G<1800 kg/(m^2s)). From these few examples, it is clear that K_1 alone cannot describe adequately the heat transfer mechanisms.

K_2 governs the movement of the interface at the contact line; the high evaporation momentum force causes the interface to overcome the retaining surface tension force. The contact angle is not included in the definition of K_2, but it plays an important role in bubble dynamics and should be included in a comprehensive analysis (see paragraph 3.2.1). Nevertheless Kandlikar asserts that the use of the non-dimensional groups K_1 and K_2 in conjunction with the Weber number and the Capillary number (both containing the vapour quality) is expected to provide a better tool for analyzing the experimental data and developing more representative models [3].

2.2 RANGES OF NON DIMENSIONAL NUMBERS EMPLOYED IN MICROCHANNELS FLOW BOILING EXPERIMENTS

The purpose of this section is to present the ranges of the non-dimensional numbers introduced in 2.1.

Starting from the data sets ([8,9,10,11,12,13]) analyzed in 2004 by Kandlikar [3] and adding all the data coming from the other papers listed in this review, a database of microchannel flow boiling experiments was created and in this section we present the ranges of non-dimensional numbers employed in all these experimental investigations. The maximum and minimum values, potentially obtainable with the experimental conditions applied during a specific investigation, are calculated for each non-dimensional number. The thermodynamic and transport properties for the fluids were calculated based on REFPROP version 8.0 of NIST. Furthermore, it must be said that not all the authors specify in a clear way the range of experimental conditions of their tests and a round-robin database is still missing. The data of Huo et al. [14] and Shiferaw et al.[15] are considered together even if the experimental data, which are related to the same experimental setup, are in fact different for many parameters, such as for example the heat transfer coefficients (see for a comparison Figure 6 and 7 in [14] and Figure 2 in [15]).

Figure 3 depicts the literature Eo number values:

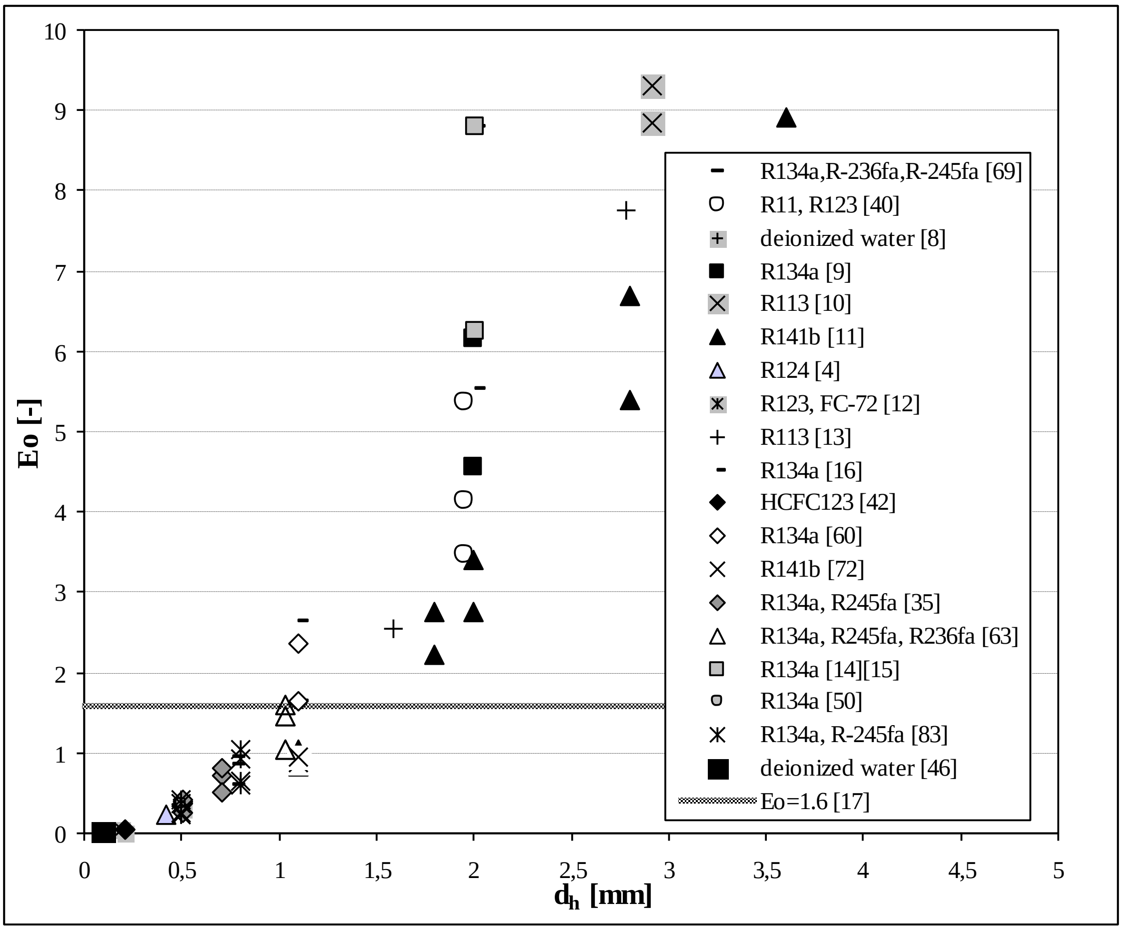

Figure 3 Eötvös number map of data in literature

All the Eötvös numbers have been calculated using the hydraulic diameter as the characteristic dimension L and, if not differently underlined, this is mantained all along the paper in order to assure parameter homogeneity. For the majority of the papers presented in this review Eo is lower than 5.

Note that the experimental data obtained in [16] with dh=2.88 mm and dh=4.26 mm and those obtained in [14,15] with dh=4.26 mm have been not considered in the figure above since Eo≥10. It would be interesting to study boiling in hypergravity conditions for channel having dh ≤ 2 mm (Figure 3); with hypergravity we mean the range from 1 to 20 g which is obtained using for example the Large Diameter Centrifuge (LDC). The hypergravity data fall in regions not yet investigated in the literature and may give interesting information. Notice that not all the considered works can be classified as "microscale flow boiling" according with the threshold value of Eo=1.6 proposed by Ullmann and Brauner [17] for the transition from macroscale to microscale.

In Figure 4, 5, 6, 7, 8, 9, 10 and 11 are presented the ranges of We_{LO}, We_{VO}, Ca_{LO}, Re_{LO}, Re_{VO}, B_l, K_1 and K_2 calculated for the data sets presented in this review.

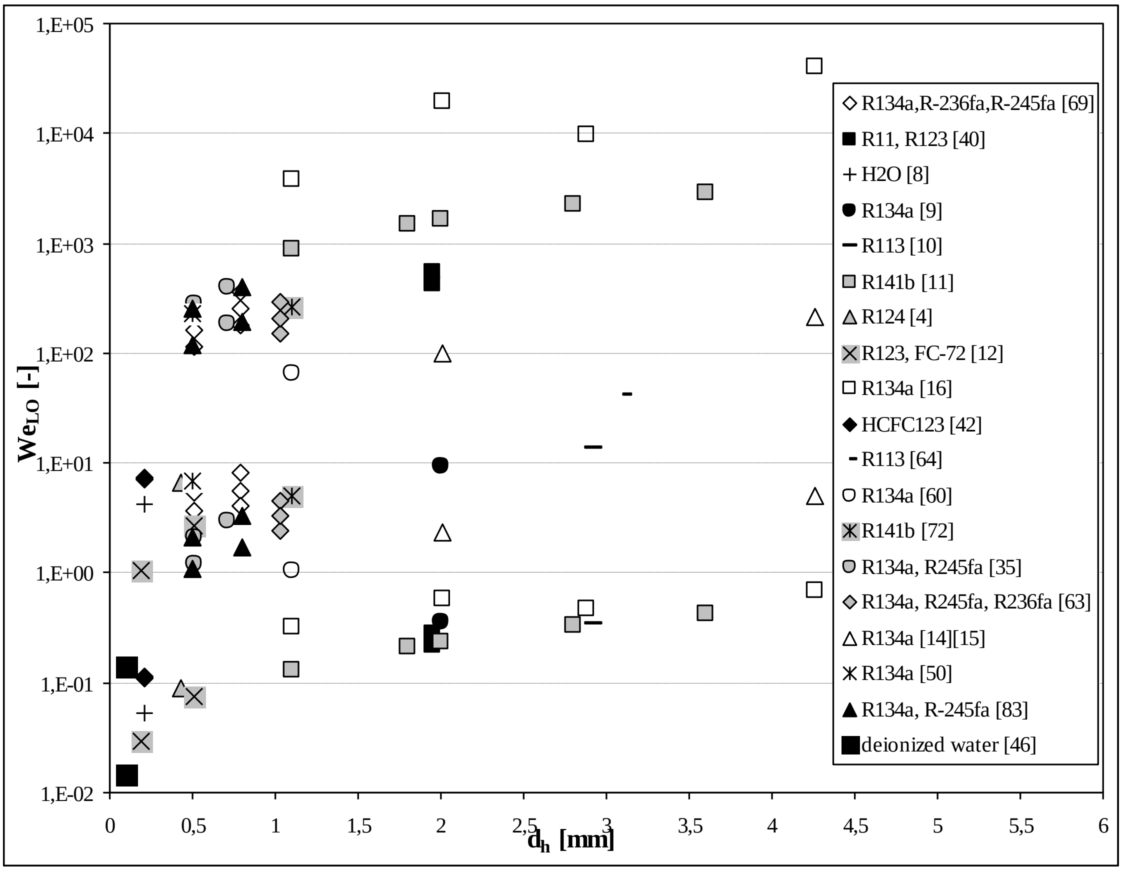

Figure 4 We$_{LO}$ number map of data in literature

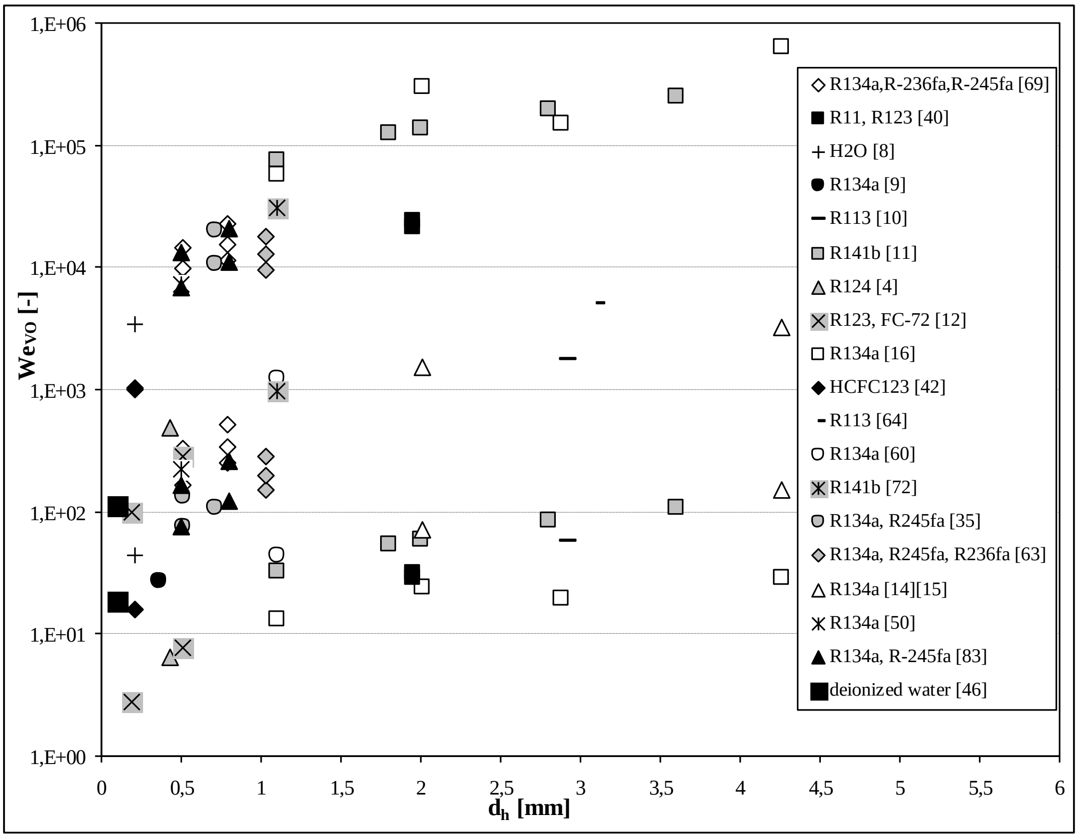

Figure 5 We_{VO} number map of data in literature

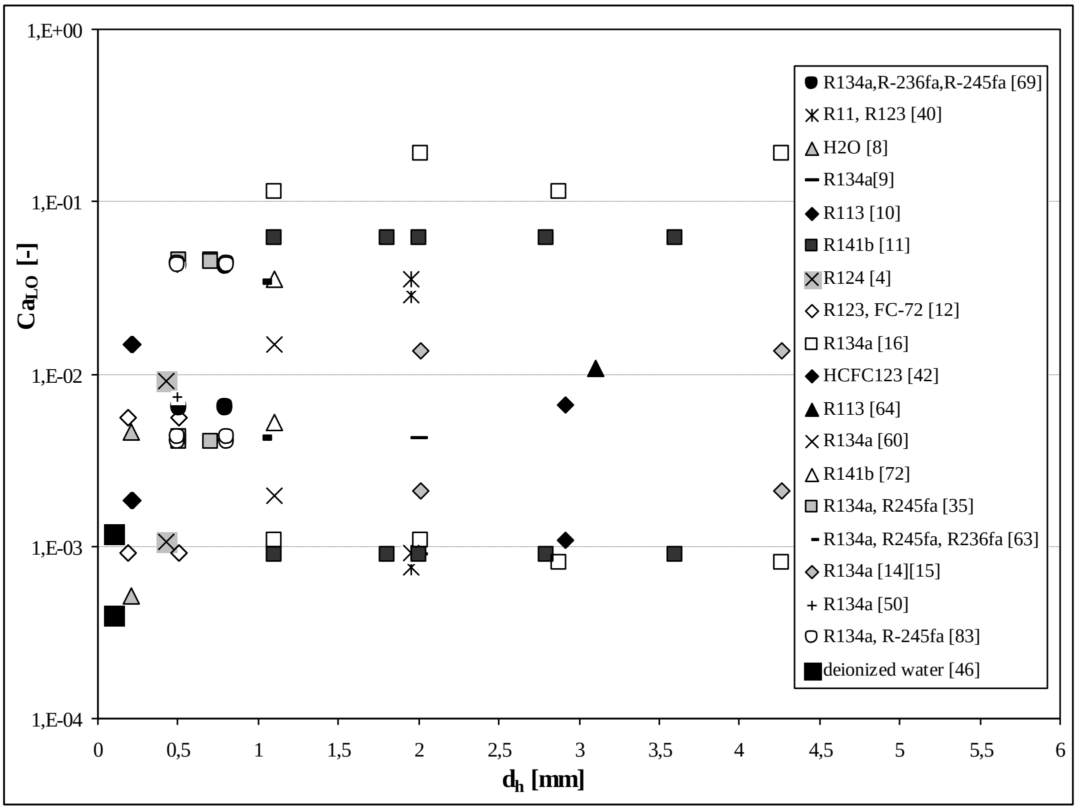

Figure 6 Ca_{LO} map of data in literature

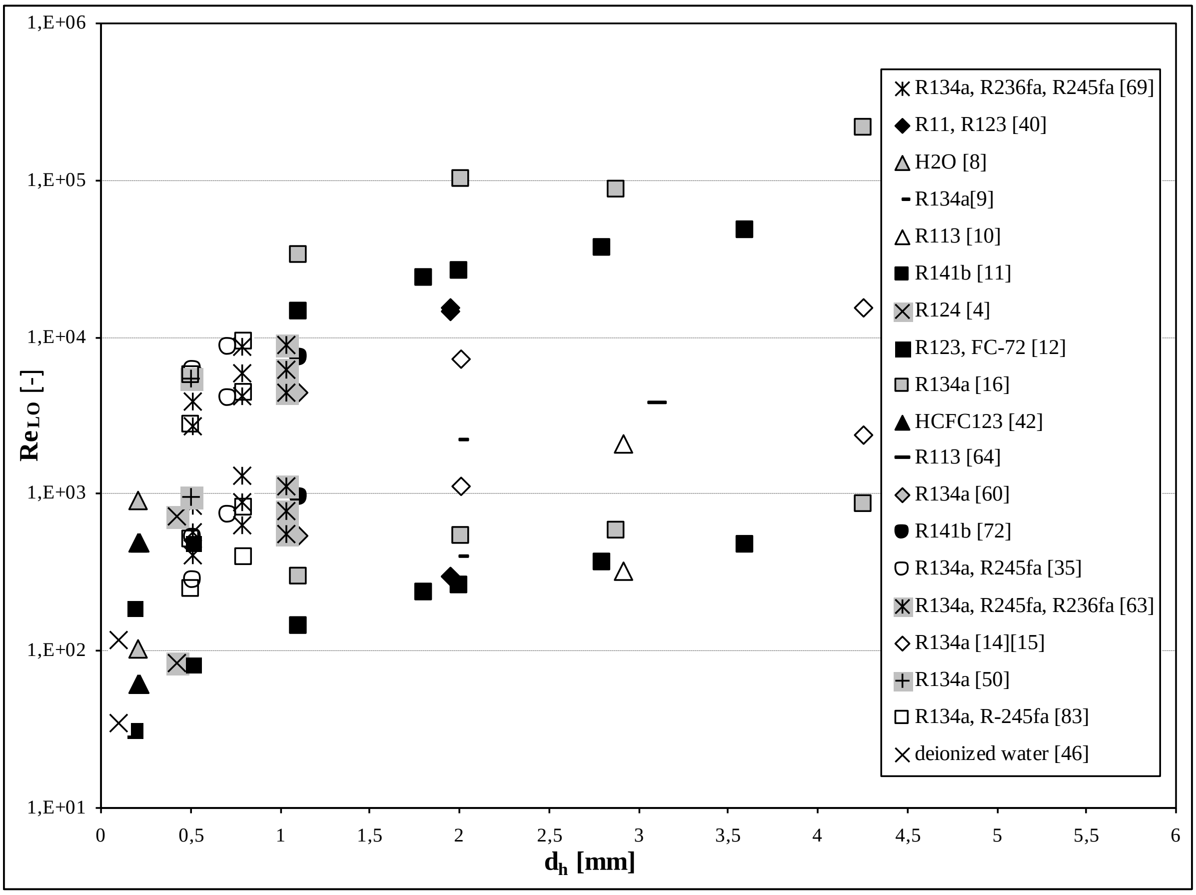

Figure 7 Re$_{LO}$ map of data in literature

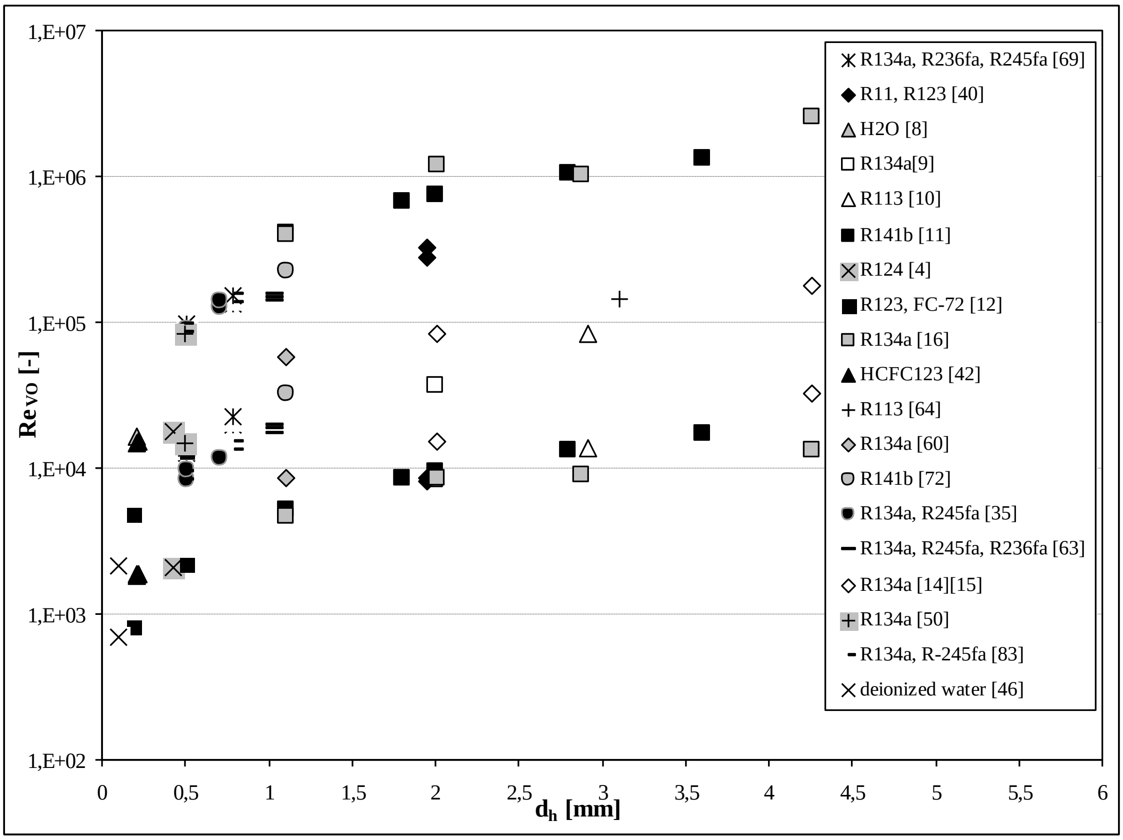

Figure 8 Re_{VO} map of data in literature

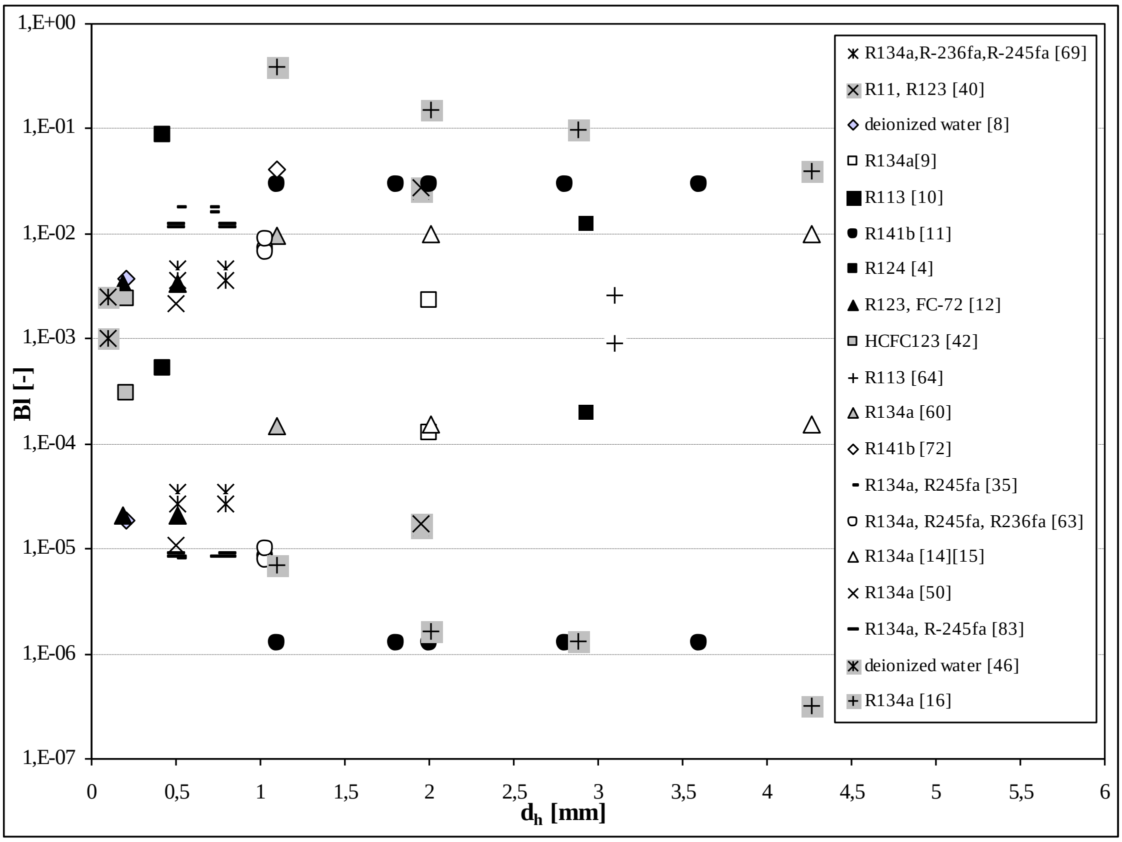

Figure 9 Boiling number map of data in literature

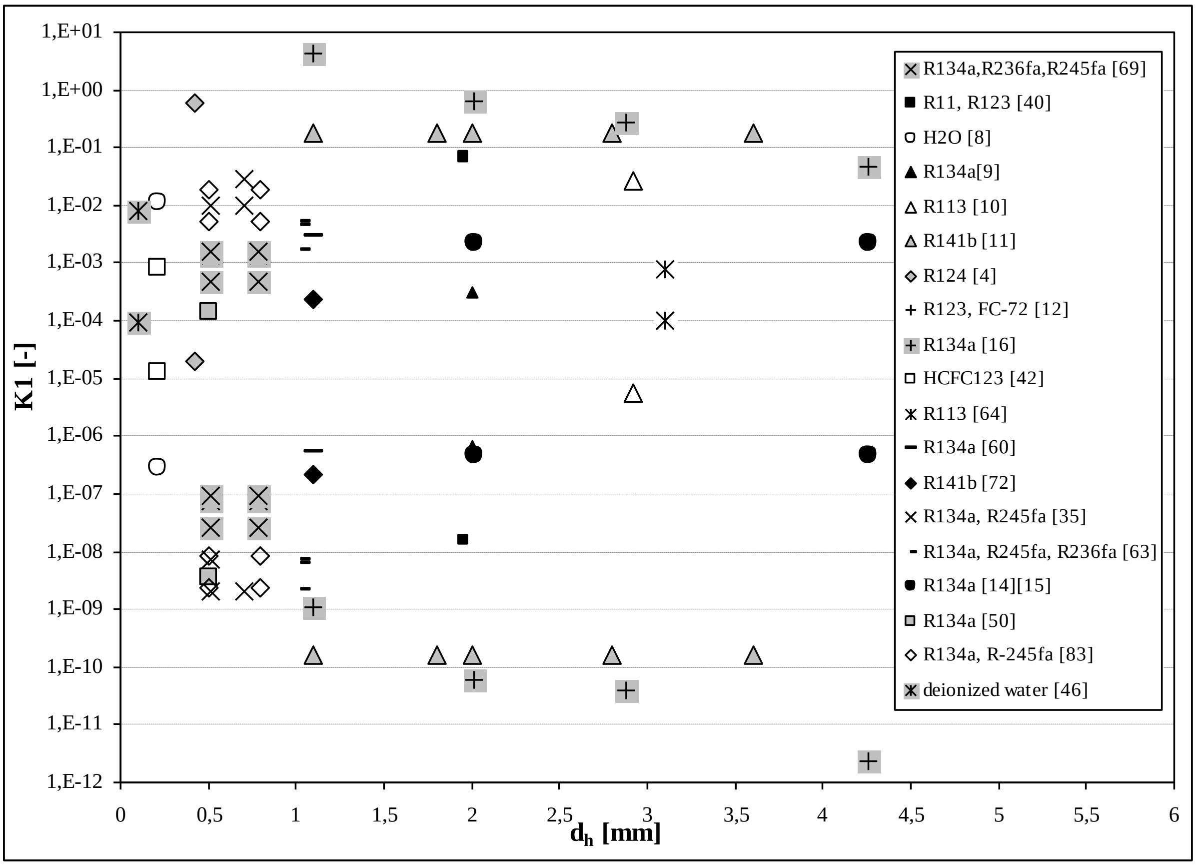

Figure 10 K_1 number map of data in literature

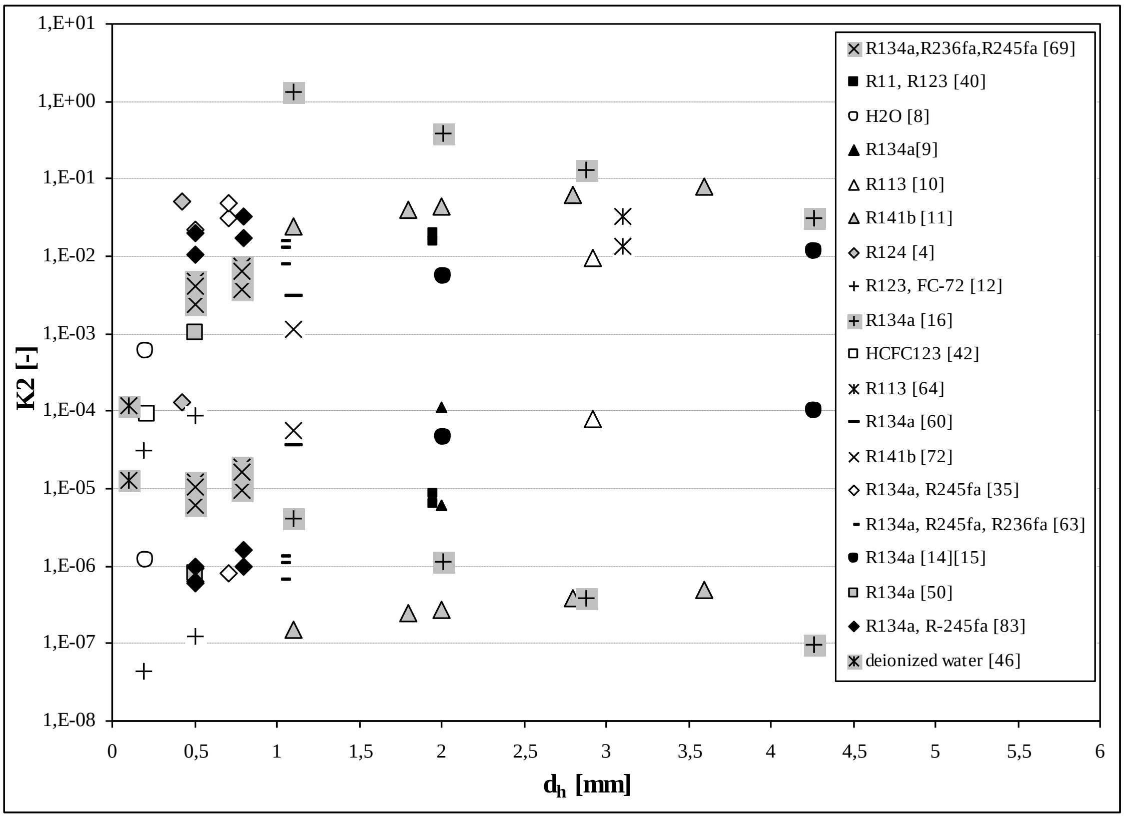

Figure 11 K_2 number map of data in literature

2.3 NON-DIMENSIONAL NUMBERS MAPS EMPLOYED IN MICROCHANNEL FLOW BOILING EXPERIMENTS IN MICROGRAVITY

In this section the ranges of non-dimensional numbers employed in recent experimental investigations in microgravity conditions are presented; the gravity in these tests is reduced thanks to parabolic flight, even if in the works of Ohta [18], [19] and Celata et al. [20], [21] the gravity is set to 0.0981 m/s^2, while Luciani et al. [5], [6] use a gravity value equal to 0.05 m/s^2.

The maximum and minimum values, obtainable from declared experimental conditions, are calculated for each non-dimensional number. The thermodynamic and transport properties for the fluids were calculated based on NIST REFPROP 8.0 except for HFE-7100, since its equation of state is not yet given. For this fluid, the tests were done at 327K [5,6], but the physical properties listed from 3M website are tabulated respectively at: σ at 298 K, h_{LV} at 334 K, while ρ_L and μ_L are plotted also for 327K.

In Figure 12 the ranges of the Eötvös numbers, calculated using the hydraulic diameter as the characteristic dimension L, are presented*:*

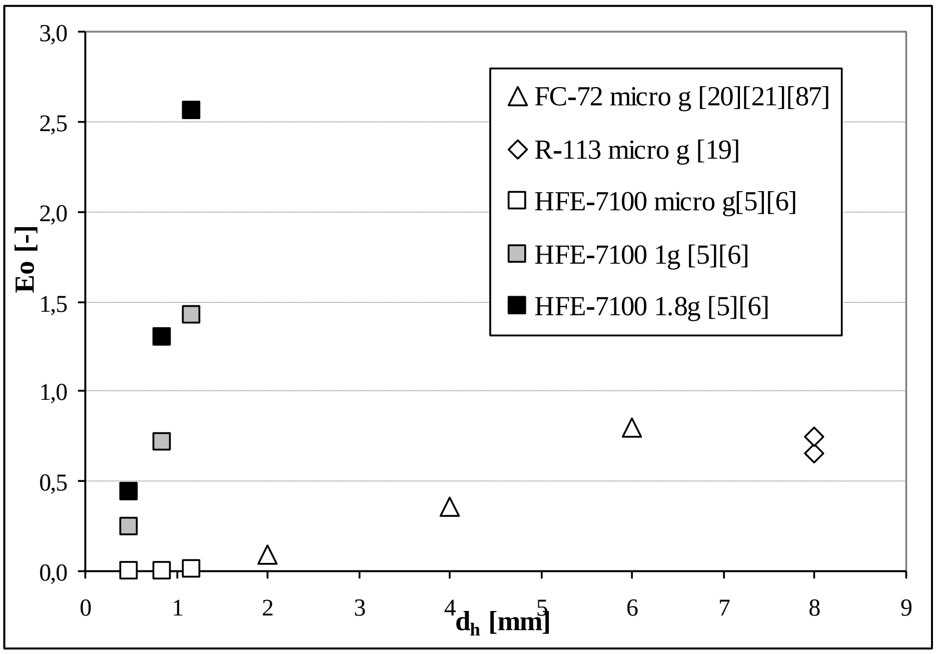

Figure 12 Eötvös number map of microgravity literature data (open symbols)

Note that all the experiments [5, 6, 19, 20, 21, 87] were conducted during parabolic flights in conditions of microgravity, terrestrial gravity and slight hypergravity. In Figure 12 data for Eo≥ 10 obtained in [19, 20, 21, 87] in the case of terrestrial gravity and hypergravity are not included because they are outside of the range of interest of the review. In microgravity conditions, Eo is lower than 1 because the Eötvös number corresponding to a test in microgravity tends to zero. The consequences of such behavior are examinated in section 3.2.

In Figure 13, 14, 15, 16, 17, 18, 19 and 20 are presented the ranges of We_{LO}, We_{VO}, Re_{LO}, Re_{VO}, Ca_{LO}, Bl, K_1 and K_2 calculated only for the microgravity data sets. In Figure 14, 16, 19 and 20 the data from Luciani et al. [5,6] are non included since the vapour density of HFE-7100 is not known to the authors.

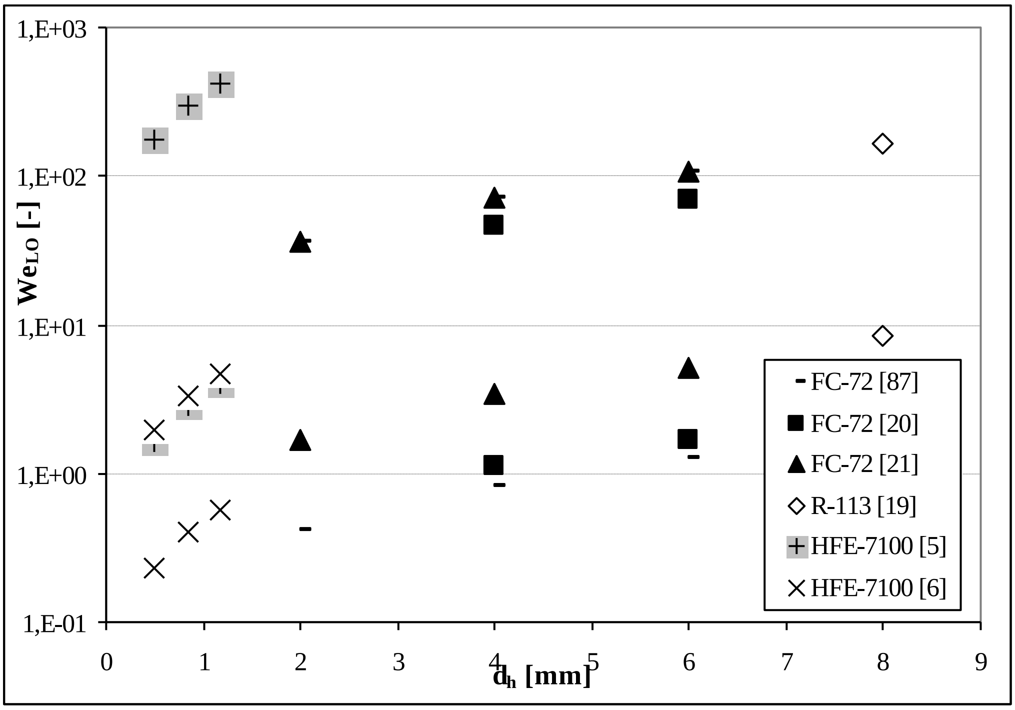

Figure 13 We_{LO} map of only microgravity literature data

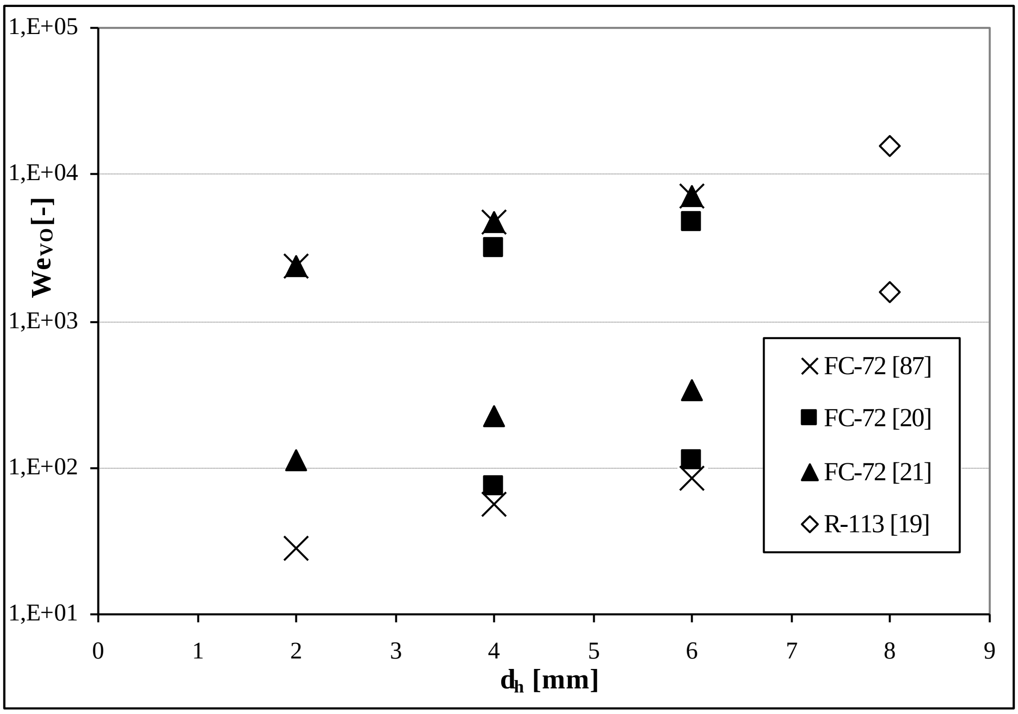

Figure 14 We_{VO} map of only microgravity literature data

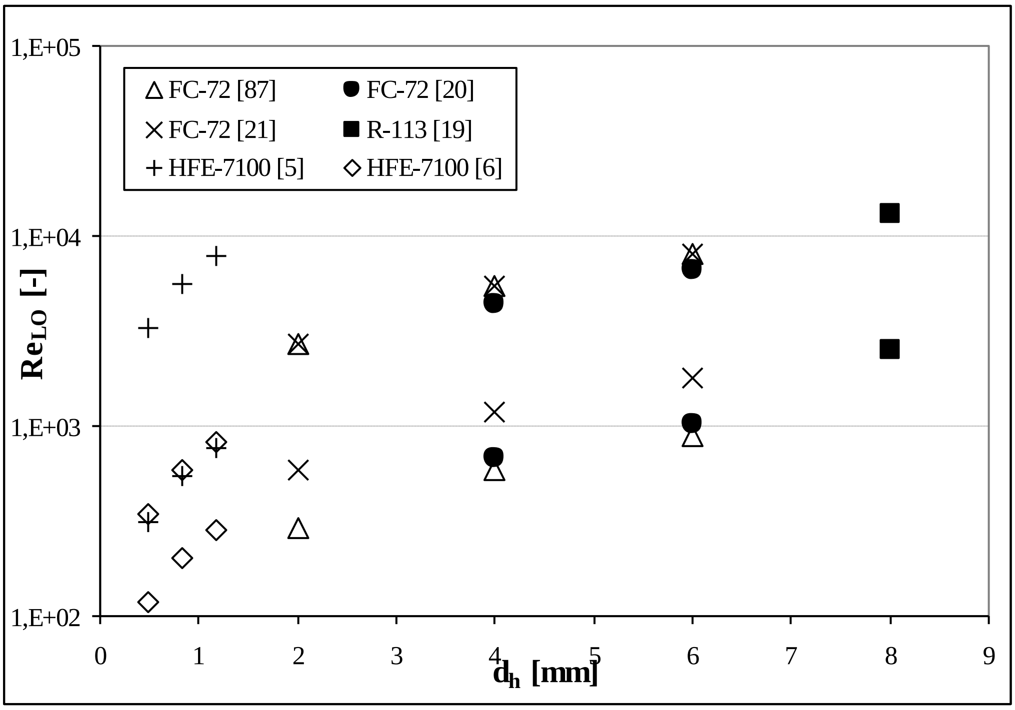

Figure 15 Re$_{LO}$ map of only microgravity literature data

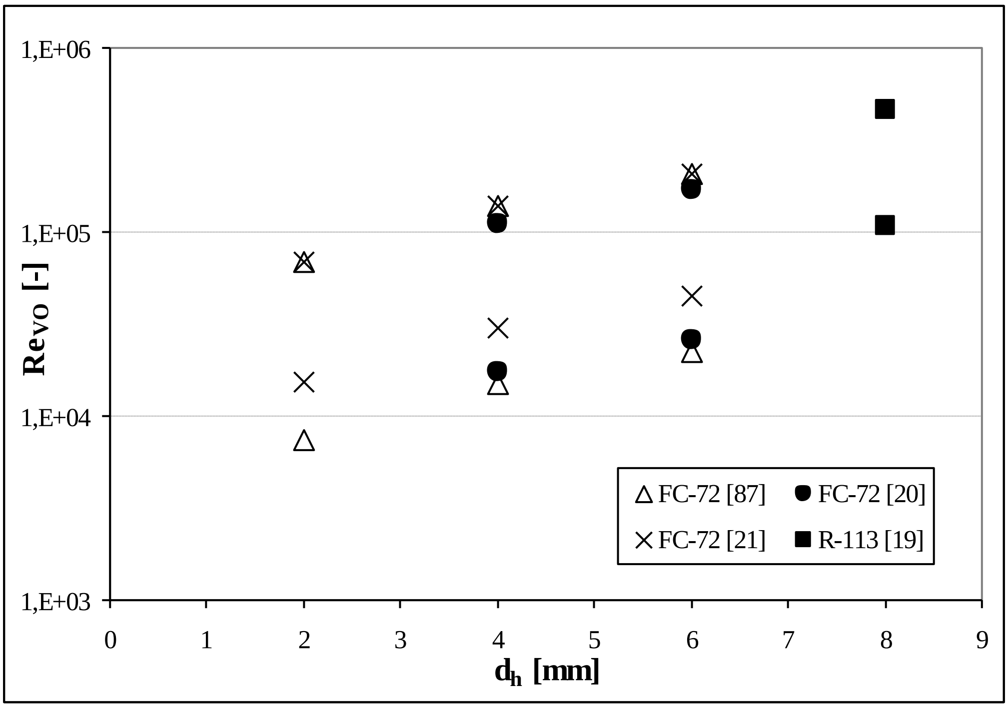

Figure 16 Re_{VO} map of only microgravity literature data

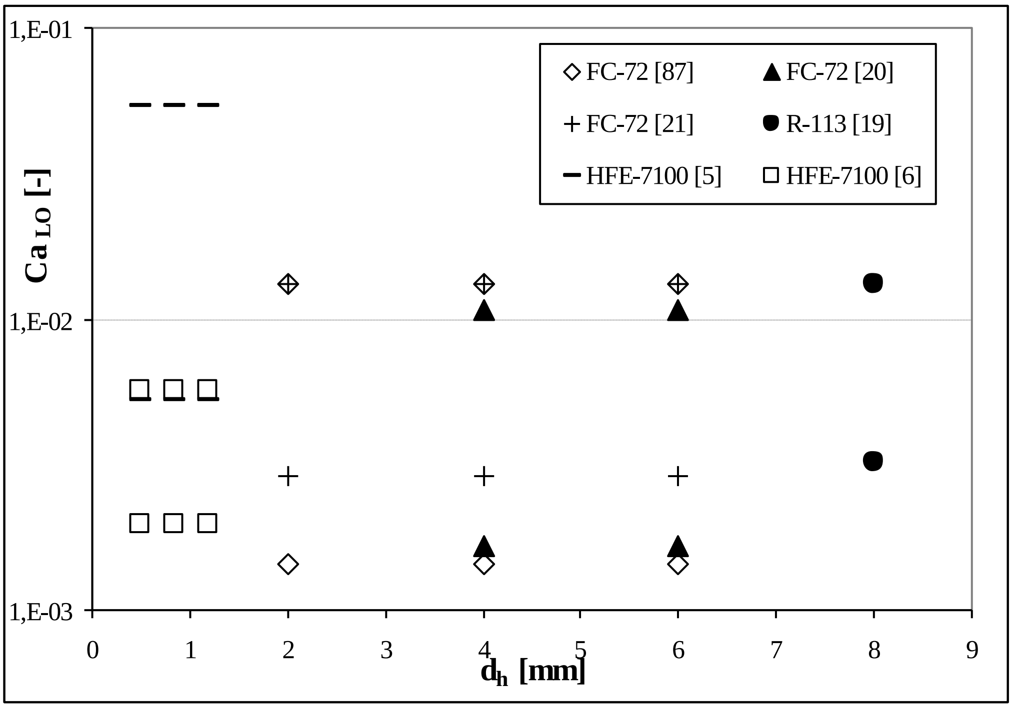

Figure 17 Capillary number map of only microgravity literature data

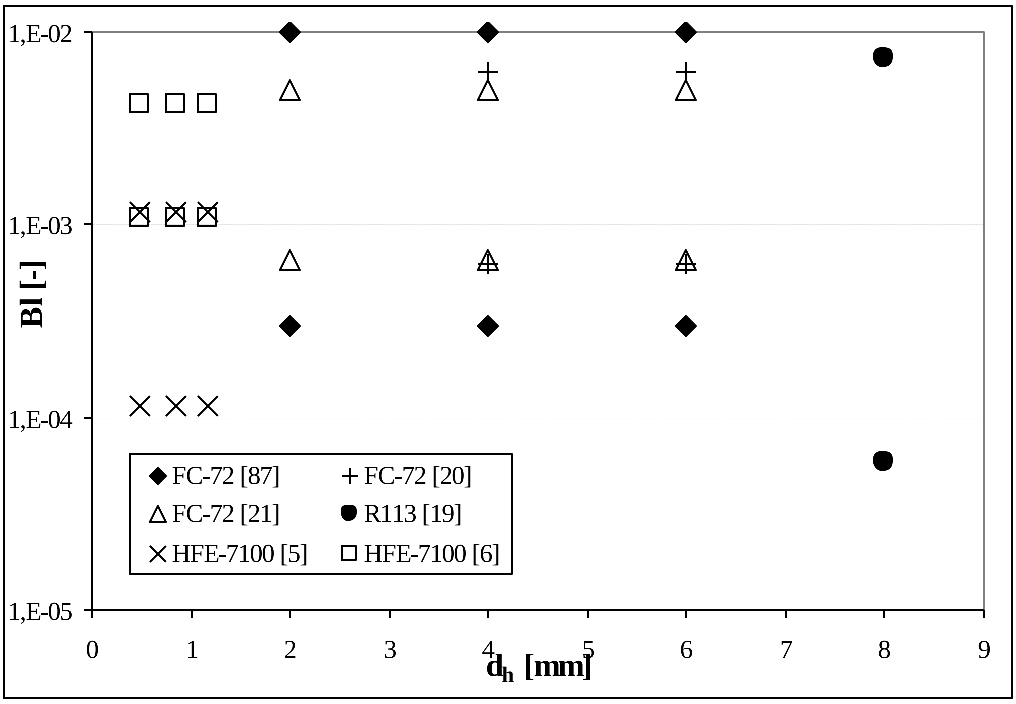

Figure 18 Boiling number map of only microgravity literature data

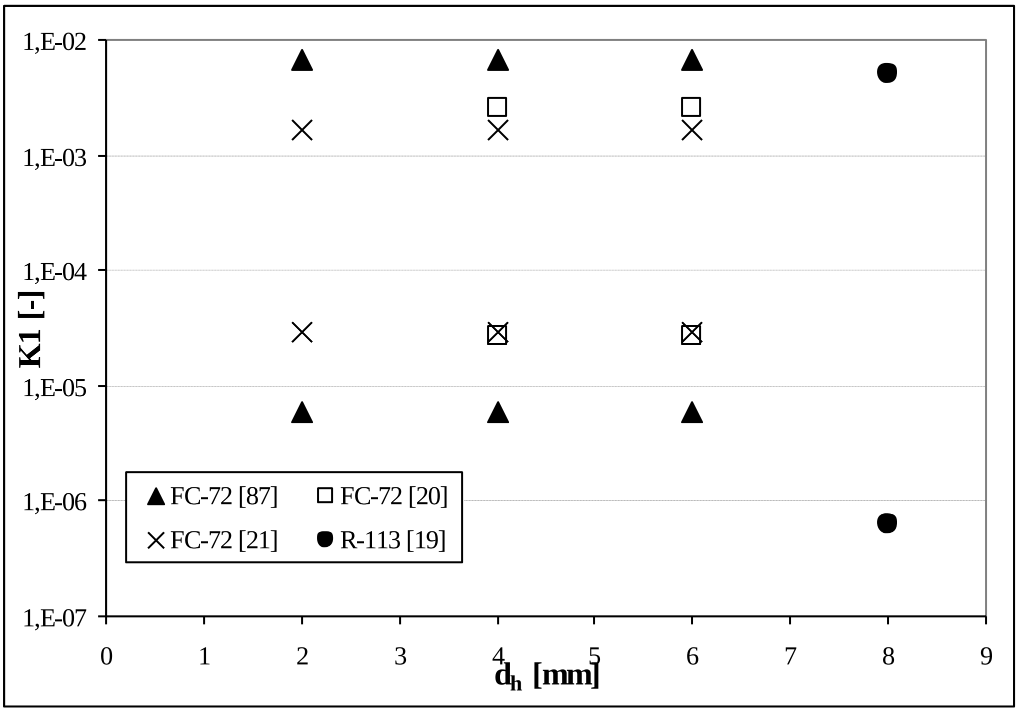

Figure 19 K_1 number map of only microgravity literature data

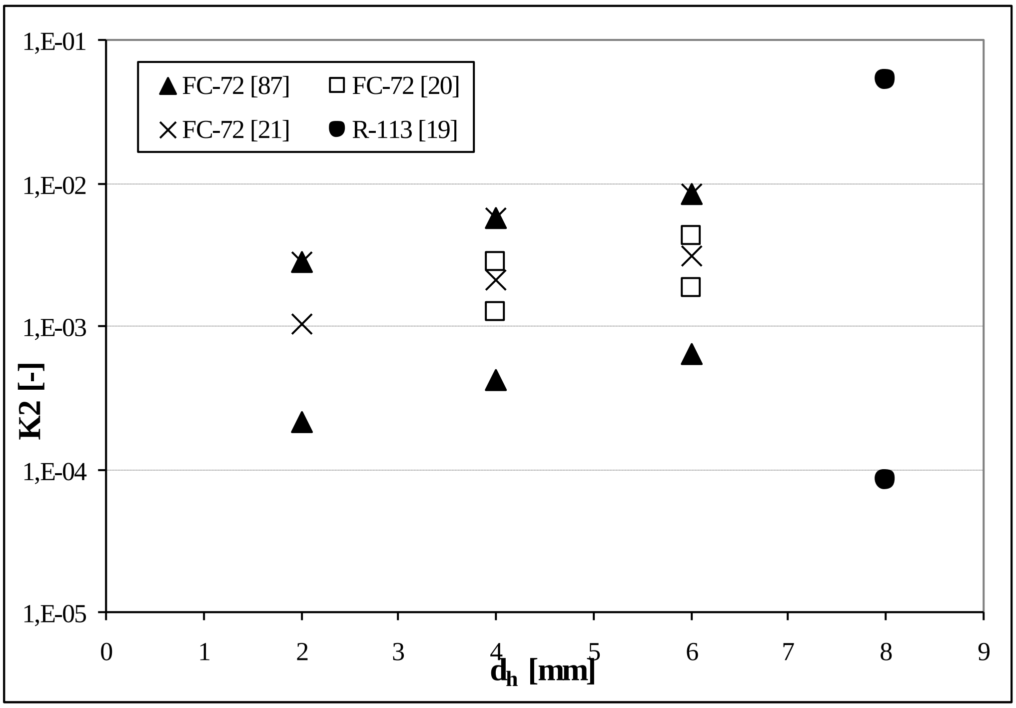

Figure 20 K_2 number experimental map of only microgravity literature data

Chapter 3

Macro to microscale transition in two phase flows

While in single phase heat transfer the threshold between microscale and macroscale can be determined on the basis of scaling effects[3] [22, 23], in flow boiling the transition between micro- and macroscale has not been well defined yet.

---

[3] In single phase heat transfer, after a period of uncertain results (1990-2007), it is nowadays clear that no peculiar physics has been detected in microscale [22], even if some phenomena are not negligible as the scale reduces; these are, for example, the so-called scaling effects in the thermal entrance length, axial conduction and viscous heating. In recent works, such as in [23], it has been found that, taking into account the scaling effects, there is a general agreement with macroscale phenomena. Hence in most of the engineer applications, the use of empirical correlations well known in

In fact a universal accepted criterion for the definition of micro-macro transition does not exist. We also believe that it is not necessary, aside from a practical taxonomy.

In [24] a classification for the transition from macroscale to microscale heat transfer based on the hydraulic diameter d_h was proposed. The size ranges recommended by Kandlikar are: microchannels (50- 600 μm), minichannels (600 μm to 3 mm) and conventional channels (d_h > 3mm). In [25] Thome underlines that “such criterion does not reflect the influence of channel size on the physical mechanisms, as the effect of reduced pressure on bubble sizes and flow transitions”. Furthermore the criterion does not take in consideration the properties of the test fluid and should be rejected as too rough.

Thome [25] asserts that a macro to microscale transition criterion might be related to the bubble departure diameter, which is defined as the point at which the bubble departure size reaches the channel diameter. If the diameter of a growing bubble reaches the internal diameter of the tube before detachment, then the bubble can only grow in length as it flows downstream and the result is that only one bubble can exist in the channel cross-section at a time. Hence, this condition of confined bubble flow[4] is suggested by Thome et al. [26] to be the threshold beyond which macroscale theory is no longer applicable.

We stress that a macro to micro transition also occurs for a fixed channel diameter, when, due to bubble coalescence downstream, there is a point along a tube where the bubble diameters may reach the channel section size. When the bubbles are able to detach from the tube surface with small sizes, any bulk force (as gravity) acting normally or radially is able to drift the bubbles downstreaming combining vectors of the flow drag force and the bulk force. But when the bubbles are

---

macroscale is still possible, when the proper channel size and surface roughness are used.

[4] Confined bubble flow describes the situation where bubbles grow in length rather than in diameter, also known as the elongated bubble regime.

completely filling the tube section, the gravity and other bulk forces are playing a role in the dynamics of the flow, only if they are aligned with the tube or channel axes. Therefore, due to bubble coalescence for example, it is possible that a transition from macro to microscale is occurring along the flow, during its development in the tube for the same tube diameter. Such effects can be also originated by the pressure drop (see paragraph 3.1).

Some evidences of macro to microscale transition are summarized in [27]. From the flow pattern point of view, stratified-wavy and fully stratified flows disappeared in small horizontal channels; in fact no stratified flow exists if the tube diameter is sufficiently small, and this could be an indication of the lower boundary of macroscale two-phase flow. The upper boundary of microscale two-phase flow might be the point in which the effect of gravity becomes negligible, meaning that in microgravity conditions there should be only microscale features. This was proved not to be true (see paragraph 6.1). From the heat transfer point of view, the results in [27] seem to suggest an increase of the heat transfer coefficient passing from the macroscale to the microscale regime defined above.

Rigorously either the microscale has only a simple relation with the channel size, i.e. it is the maximum value of micrometers above which the physical phenomena, given the same fluid and physical flow condition suh as G, x, are showing a rapid variation in terms of patterns, pressure drop and heat transfer, or could be improperly defined as a given scale or a given characteristic length taking into account also the physical properties of the fluid. Under such given size, some of the usual physical phenomena in macroscale (i.e. for a larger scale) should change. For example, the capillary length lc is defined as

$$l_c = \left[\frac{\sigma}{g(\rho_L - \rho_V)} \right]^{\frac{1}{2}}$$

where σ, g, ρ_L and ρ_V are the surface tension, gravitational acceleration and densities of the liquid and vapor at the saturated pressure, respectively; l_c could be useful because the bubble departure diameter usually is considered proportional to the capillary length. This may lead to a reduction in the departure frequency for high surface tension fluids.

In our opinion no physical sharp distiction of a macro and a micro regime occurs, since, until an estremely low value of the channel size, the fundamental physical phenomena are simply the same, i.e. there is no “microscale” or “macroscale”, but only a change of the flow patterns, and therefore of the heat transfer mechanisms, linked to different values of flow parameters and dimensionless numbers. Keeping in mind this observation, we still acknowledge the pratical usefulness of studying which could be the best dimensionless numbers able to follow the effects of length scales on the variations of the main two-phase characteristics, such as flow patterns, heat transfer coefficients, pressure drops and so on. Hence, one should be aware that ethimologically the term “micro” is then used in broadly speaking, since the “microscale” could be reached in channels of millimetric size.

3.1 STANDARD CRITERIA

In literature five different criteria are used to distinguish between microscale and macroscale and in this review they are presented and compared.

Kew and Cornwell [*28*] recommended a confinement number, Co, to distinguish between micro and macroscale. Co, introduced in table 1, is the ratio between the capillary length l_c and the hydraulic diameter. Kew and Cornwell [28] found deviations in the flow regimes from those observed in large channels and that existing flow boiling heat transfer correlations do not perform well when applied to narrow channels having Co >0.5; therefore they set Co =0.5 as the threshold for microscale flows. In [*29*] an experimental microscale heat transfer database was proposed. The considered hydraulic diameters are compared with the threshold diameter criterion of Kew and Cornwell [28], showing that about half of the experimental test sections describe in Table 3 of [29] can be classified as microscale according to such criterion.

In 2003, Li and Wang [*30*] recommended using the capillary length, l_c, to distinguish between micro and macroscale and give the following condensation flow regimes based on the tube diameter d:

- $d > d_{th}$ gravity forces are dominant and the flow regimes are typical of macroscale
- $d < d_c$ the effect of gravity on the flow regime can be ignored completely; the flow is symmetric with respect to bulk forces and it is a microscale flow
- $d_c < d < d_{th}$ gravity and surface tension forces are equally dominant; a slight stratification of the flow distribution was observed.

The values of tube diameter, d_c and d_{th}, in terms of l_c are $d_c = 0.224 l_c$ and $d_{th} = 1.75 l_c$.

In 2006 Cheng and Wu [*31*], based on the critical and threshold diameters obtained by Li and Whang [30], classified phase change heat transfer in channels according to Bo as follows:

- microchannel if $Bo < 0.05$, the effect of gravity can be neglected
- mesochannel if $0.05 < Bo < 3$, surface tension effect becomes dominant and gravitational effect is small
- macrochannel if $Bo > 3$, the surface tension is small in comparison with gravitational force.

Note that this criterion is more stringent than the one given by Kew and Cornwell [28], which observed deviation from macroscale when Bo<4[5], that corresponds to diameters lower than $d_{th}\big|_{Bn=4} = 2\sqrt{\dfrac{\sigma}{g(\rho_L - \rho_V)}}$

A recent and reasonable criterion to identify the threshold has been recently proposed by Ullmann and Brauner [17] on the basis of flow pattern maps, using Eo. On the basis of flow pattern map deviation for experiments in pipes, Ullmann and Brauner proposed a microscale threshold of $Eo \leq 1.6$. Remarking that Kew and Cornwell [28] assumed microscale flow when $Co > 0.5$, it is interesting to note that $Eo \leq 1.6$, according to Ulman and Brauner criterion [17], means $Co \geq 0.79$. For the same fluid, i.e., R134a, at the saturation temperature of 0°C, the two criteria yield the transition between micro- and macroscale of 1.21 mm [17] and 1.92 mm [28], respectively.

In 2010 Harirchian and Garimella [32] developed a new transition criterion based on the fact that bubble confinement depends on channel size and on the mass flux since the bubble diameters varies with the flow rate. Using FC-77 flow visualizations, they divided their experimental values into two groups: confined and unconfined flow, as in Figure 216 where the solid line is a fit of the transition points between these two flows. This transition is represented by the equation:

$$Bo^{0.5} \times \mathrm{Re}_{LO} = \frac{1}{\mu_L}\left(\frac{g(\rho_L - \rho_V\ )}{\sigma}\right)^{0.5} GD^2 = 160$$

and $Bo^{0.5} \times \mathrm{Re}_{LO}$ is called by Harirchian and Garimella "convective confinement number" and is denoted as Ga in this review;

---

[5] In fact $Bo = \dfrac{1}{Co^2}$

[6] In figure Re indicate the Reynolds number calculated using the liquid phase mass flux and so it corresponds to ReLO defined in nomenclature.

when Ga is equal to 160 the threshold between micro and macroscale occurs.

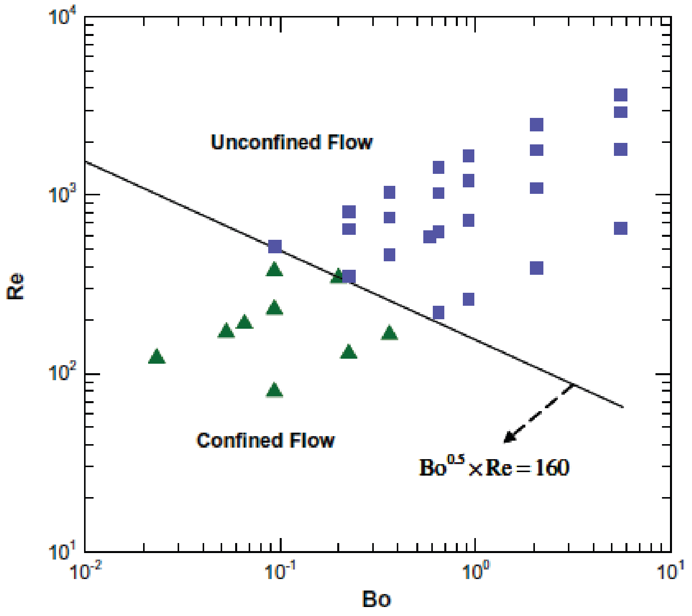

Figure 21 Experimental confined and unconfined flow and the transition between them [31]

This criterion considers as microchannels those channels having Ga<160 while for larger convective confinement numbers, the vapor bubbles are not confined and the channels is considered as a macroscale channel. Harirchian and Garimella criterion [32] seems able to predict the confined or unconfined nature of the flow for experimental observations in literature having water, dielectric liquids and refrigerants as working fluids. In [32] it is underlined that both visualized flow boiling patterns as well as heat flux data are hence necessary to use such criterion. Therefore there is the necessity of more complete tests in order to establish which range of values of the convective confinement number Ga is able to characterize the transition macro to microscale.

Convective confinement number is proportional to mass flux and inversely proportional to liquid dynamic viscosity; expressing the convective confinement number in terms of Eo, the critical Eo number becomes $Eo_{Ga} = \left(\frac{160}{\mathrm{Re}_{LO}} \right)^2$

In 2011 Ong and Thome [99] proposed a macro to microchannel transition criterion based on flow patterns visualizations, film thickness uniformity/nonuniformity and the dominance of the gravity force. The criterion is expressed in terms of the confinement number Co; gravity dominate when Co < 0,34 while surface tension when Co > 1. So there is macroscale for Co<0.34 while for 0.34<Co<1 there is mesoscale and for Co<1 there is microscale.

This criterion is based on the confinement number Co and it rules

Rewriting all the above criteria in terms of the Eötvös number, it is found that Kew and Cornwell criterion [28] corresponds to Eo=4, the Li and Wang threshold [30] to macroscale is Eo=3.06, Cheng and Wu classification [31] to Eo=3, the convection confinement number criterion [32] to $Eo=(160/Re_{LO})^2$ and the Ong and Thome [99] threshold to macroscale is Eo=8.65. From the calculation of the threshold diameter d_{th}, that is the threshold below which there are deviations from macroscale flows, according to the criteria expressed above, it has been obtained:

$d_{th} = 2\sqrt{\frac{\sigma}{g(\rho_L - \rho_V)}}$ that corresponds to Co=0.5 (Eo=4) [28]

$d_{th} = 1{,}75\sqrt{\frac{\sigma}{g(\rho_L - \rho_V)}}$ that corresponds to d_{th}=1.75 l_c (Eo=3.06) [30]

$$d_{th} = \sqrt{3}\cdot\sqrt{\frac{\sigma}{g(\rho_L - \rho_V)}}$$ that corresponds to Bo=3 (Eo=3) [31]

$$d_{th} = \sqrt{1{,}6}\sqrt{\frac{\sigma}{g(\rho_L - \rho_V)}}$$ that corresponds to Eo=1.6 [17]

$$d_{th} = \frac{160}{\mathrm{Re}_{LO}}\sqrt{\frac{\sigma}{g(\rho_L - \rho_V)}}$$ that corresponds to $Eo=(160/Re_{LO})^2$ [32]

$$d_{th} = 8.65\sqrt{\frac{\sigma}{g(\rho_L - \rho_V)}}$$ that corresponds to Co=0.34 [99]

In Figure 23 and Figure 24 the macro to microscale transition criteria listed above are applied to R134a and water. The threshold diameter is presented as a function of the reduced pressure7; it becomes smaller as the saturation pressure increases. In order to estimate the threshold diameter for the convection confinement number criterion [32], we consider 102<ReLO<105 as from the map of literature data presented in Figure 7. This means that the threshold diameters associated to these ReLO values are:

$$d_{th} = 1.6\sqrt{\frac{\sigma}{g(\rho_L - \rho_V)}} \quad for\ Re_{LO} = 10^2$$

$$d_{th} = 1.6\cdot 10^{-3}\sqrt{\frac{\sigma}{g(\rho_L - \rho_V)}} \quad for\ Re_{LO} = 10^5$$

that corresponds, respectively, to Eo=2.56 and Eo=2.56 $\cdot 10^{-6}$. It must be underlined that $\mathrm{Re}_{LO} = 10^5$ characterizes a turbulent flow, which is very difficult in a microchannel; so the threshold diameter

---

[7] The reduced pressure is $p_{red} = \frac{p_{sat}}{p_{crit}}$

corresponding to this value of Re_{LO}, that would be in the order of few μm, cannot have any comparison with the present data. Figure 22 and Figure 23 present the threshold diameter below which deviations from macroscale flows occur.

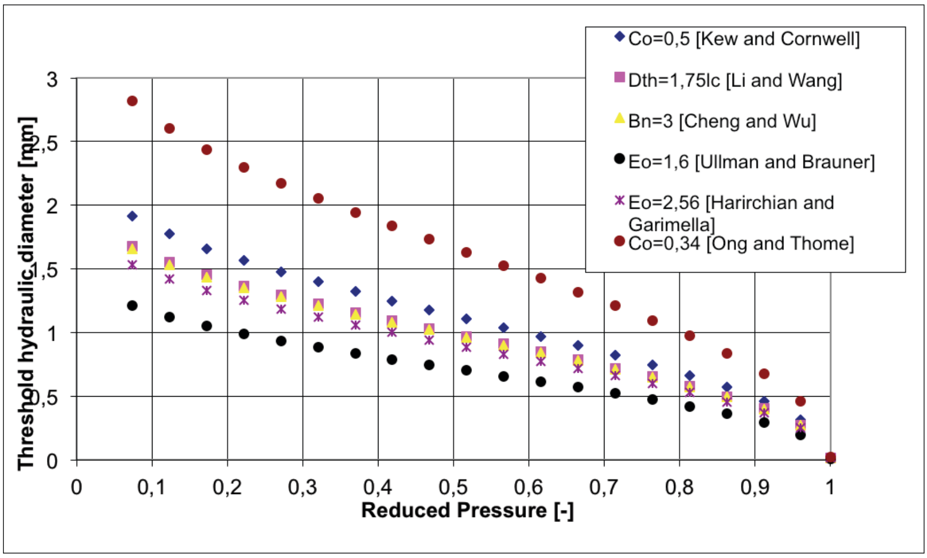

Figure 22 Comparison of selected macro to microscale transition criteria for R134a as a function of reduced pressure

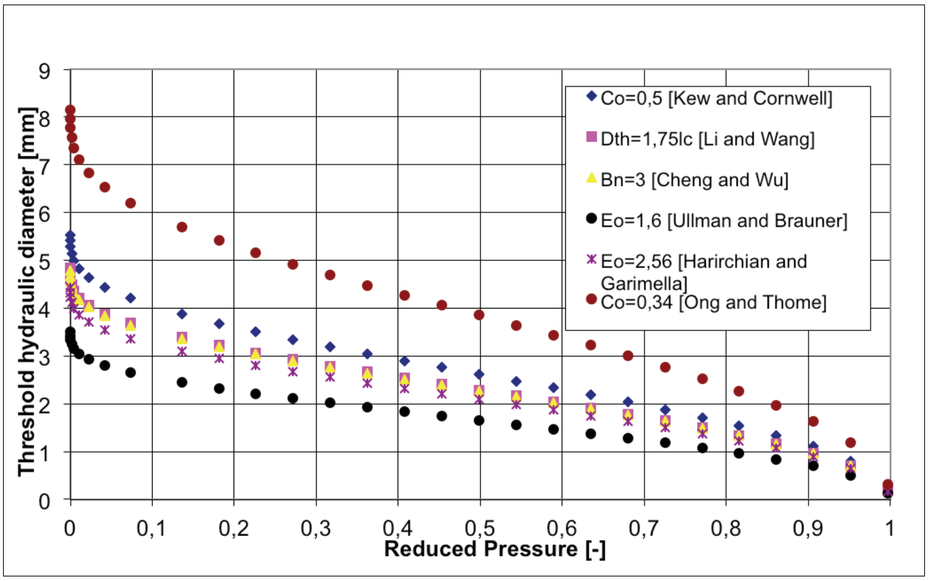

Figure 23 Comparison of selected macro to microscale transition criteria for water as a function of reduced pressure

To understand which of the experiments cited in this paper could be classified as microscale according to [*17*], Figure 24 plots the ratios between the hydraulic diameters used in some of the cited papers and the threshold diameter calculated according to [17].

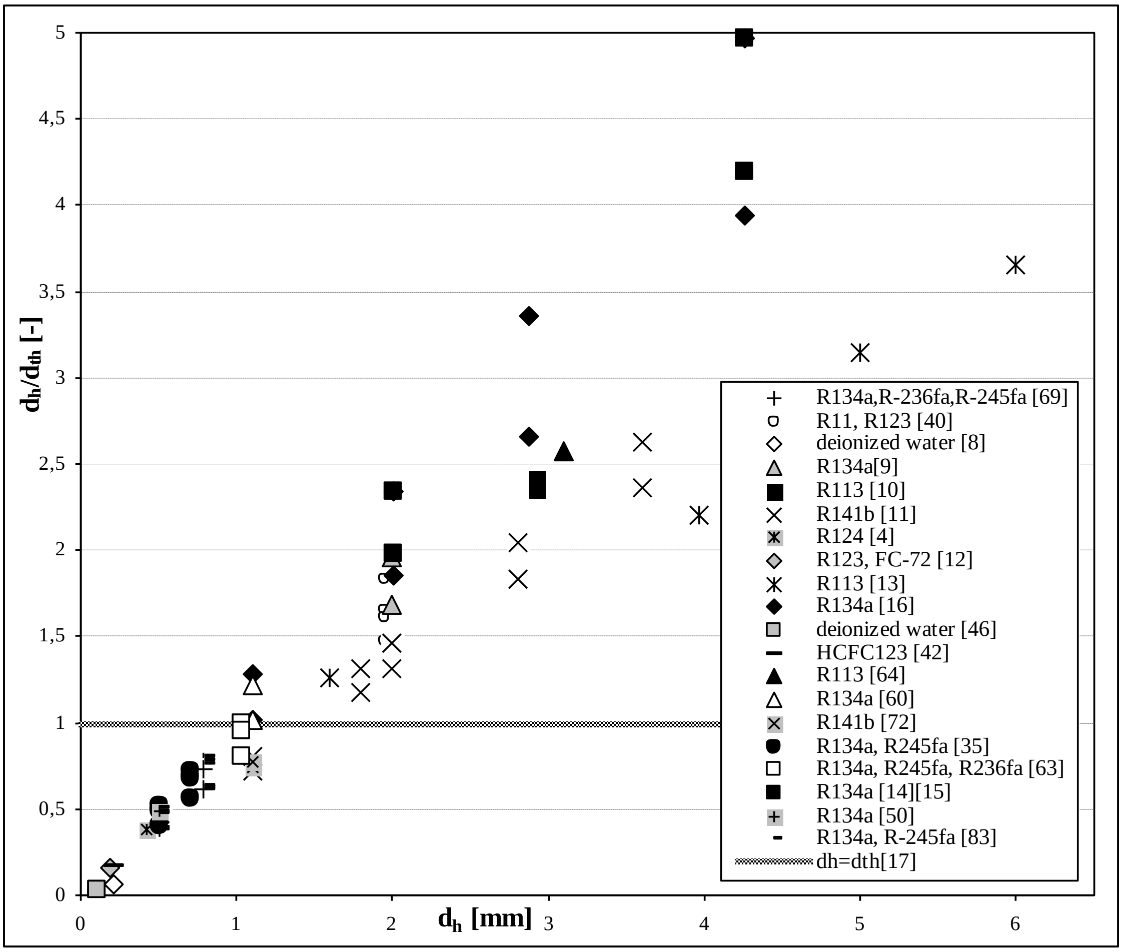

Figure 24 Comparison between the experimental hydraulic diameters and the threshold diameter of Ullman and Brauner [17]

For a specified hydraulic diameter, there are different values since the authors made experiments with several pressure/temperature values and so the threshold diameters are different. Twelve papers out of twenty have a ratio between hydraulic diameter and the threshold diameter lower than 1 and so can be classified as microscale according to [17].

Plotting in Figure 25 Eo and Ga numbers associated to the database presented in this work, it emerges that eight papers out of ninenteen can be considered as microscale according to both criteria based on Eo [17] and Ga [32]. There are four papers where the experimental conditions for microscale [63,70,72,50] satisfy the Eo criterion but not the Ga criterion; in Figure 25 there are some experimental works that can be classify as microscale or as macroscale depending on the specific testing conditions.

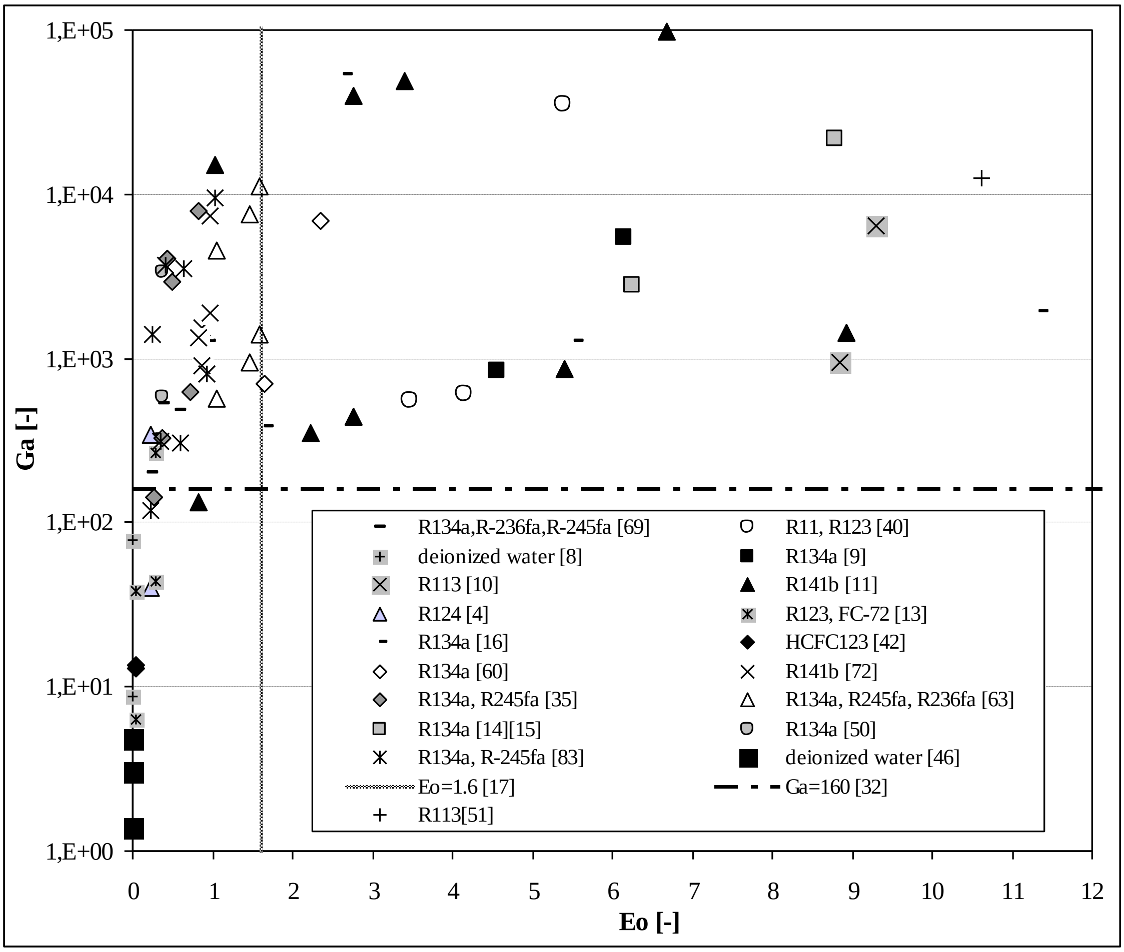

Figure 25 Convective confinement number Ga vs. Eötvös number map for literature data

As concluding remarks of this “macro to micro” section, it is necessary to underline that since the micro-to macroscale threshold has been practically associated with bubble confinement, a more refined correlation is still necessary to define a univocal and universal criterion for the transition from unconfined to confined bubble flow. Better characterized experimental data are necessary to improve the knowledge in this field and some effects, like bubble confinement, the prevalence of surface tension over buoyancy and the importance of inertial forces in the force balance, have still to be investigated and analysed in detail.

Finally it is also evident that, since the pressure drop in microchannels is very significant, a transition from an unconfined to a confined flow may appear along the tube or the channel due to the decrease of the local pressure. Such transition is not yet investigated in the literature. In order to clarify this issue, the Lockhard and Martinelli approach [*33*] as generalized by Chisholm [*34*], is here used to calculate the pressure drop for R-134a in the experimental conditions described in [35]. The threshold diameters obtained, in agreement with [17] are plotted as a function of the length of the channel in Figure 26 and in Figure 27. In Figure 26 the authors decided to consider a reasonable maximum channel length of 450 mm; the resulting pressure drop is not very important, due to the low value of G. In Figure 27 indeed, due to the higher value of G, the channel length considered *was* 300 mm for the lower vapor quality while it decreases as the vapor quality increases since the pressure drop becomes too high. The maximum pressure drop considered *is* 0.59 MPa.

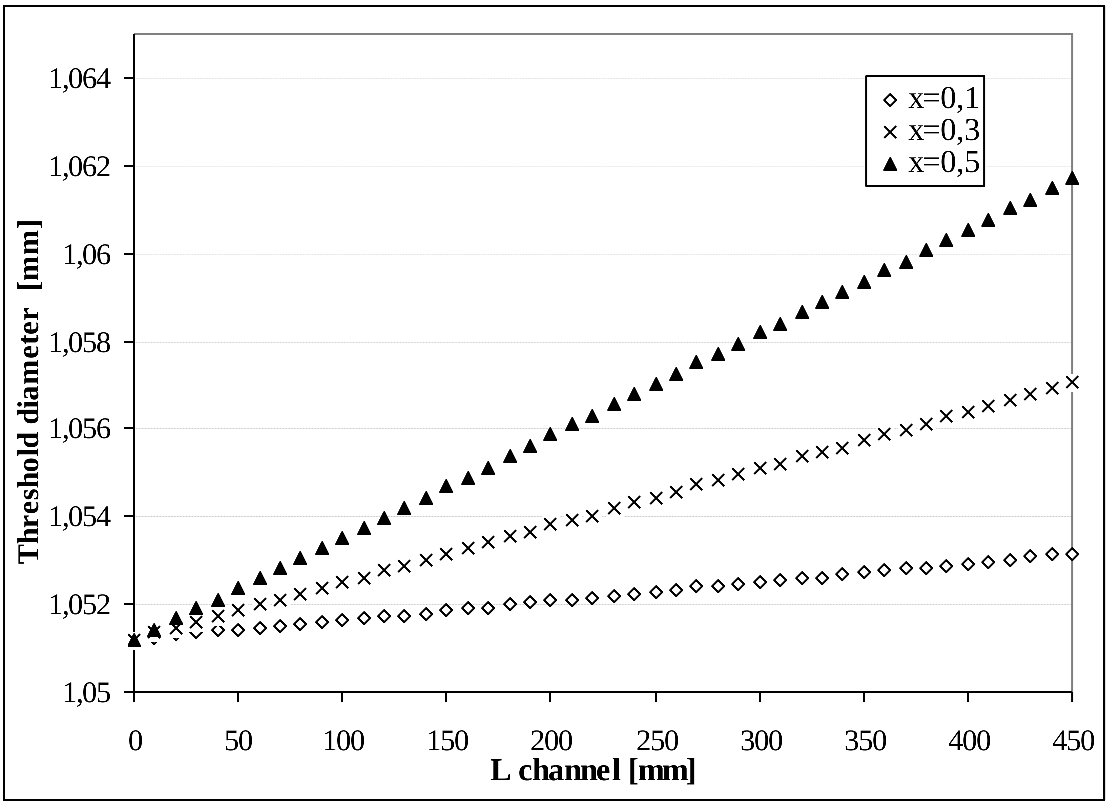

Figure 26 Increasing threshold diameter along the channel for R-134a with G=200 kg/m^{2}s, p_{sat}=0.69 MPa, d_h=0.509 mm and different inlet vapour quality (x=0.1, x=0.3, x=0.5), based on the recommendation of [17]

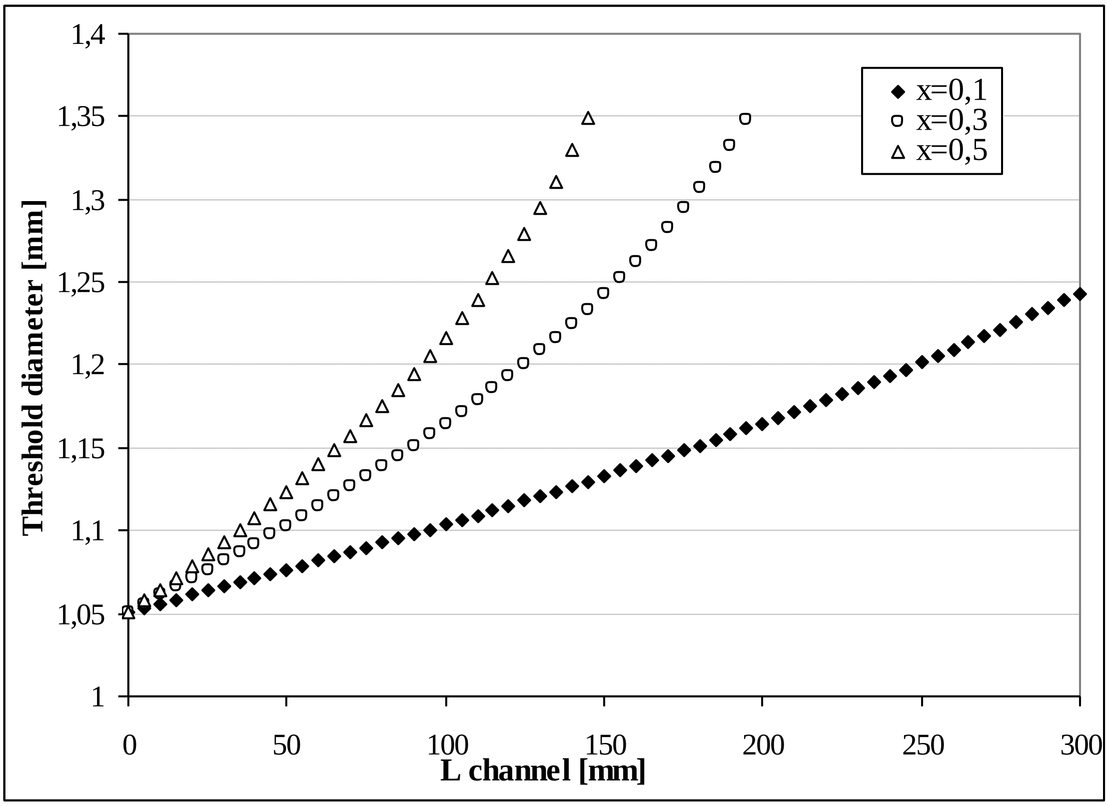

Figure 27 Increasing of the threshold diameter along the channel for R-134a with G=2094 kg/m^{2}s, p_{sat}=0.69 MPa ,d_h=0.509 mm and different inlet vapour quality (x=0.1, x=0.3, x=0.5), based on the recommendation of [17]

To summarize the behaviour of the threshold diameter [17] along the channel, due to the pressure drop, the authors decide to calculate where, in a R-134 a channel having d_h=1mm and p_{sat}=1 MPa, there is a macro to micro transition, according to [17], for different G values. This is represented in Figure 28 for inlet vapor quality x=0.1, x= 0.3 and x= 0.5.

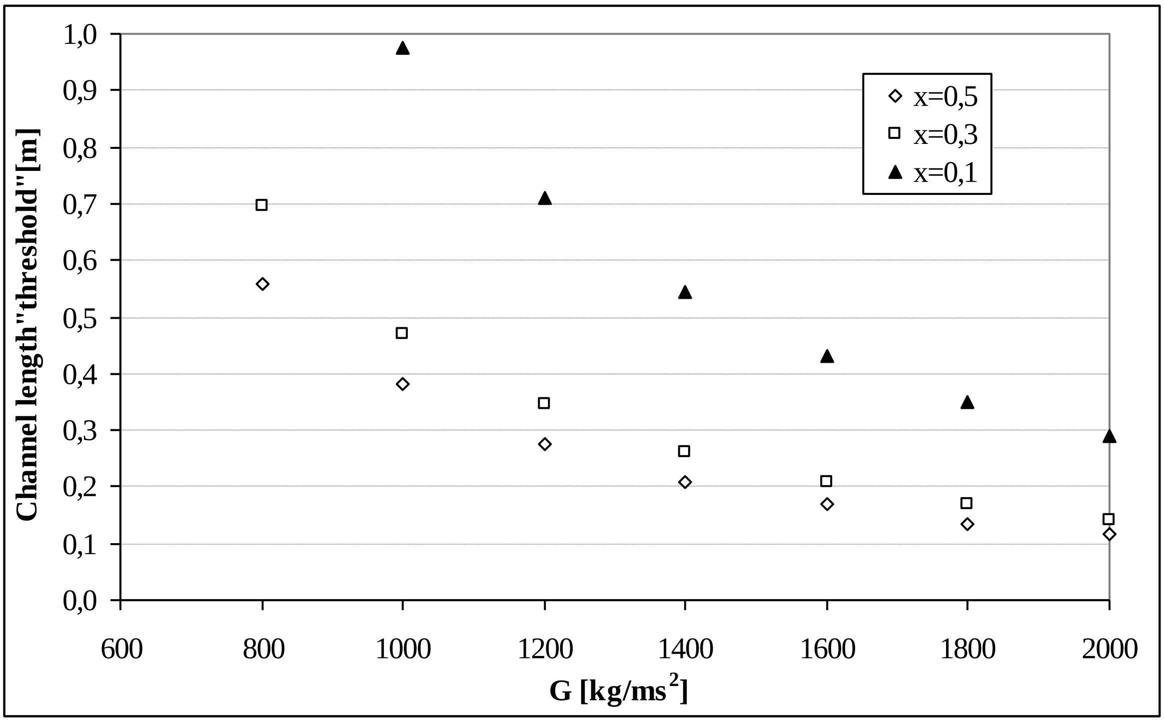

Figure 28 Location of “macro to micro” transition along a channel with d_h=1 mm [17], as function of G for R-134a, p_{sat}=1 MPa and for three different inlet vapor quality (x= 0.1, x=0.3, x=0.5)

It must be noted that for x=0.1 and G≤800 kg/ms^2, d_h=1 mm can not be considered as “microchannel”, according to [17], until the channel length of 1 m. For x=0.3 the transition to confined bubble flow occurs (at 70 cm after the inlet for G≤800 kg/ms^2) and the same for x=0.5 (at 55 cm after the inlet for G≤800 kg/ms^2).

3.2 MICROGRAVITY CONDITIONS

Although the criterion based on Eötvos number [17] seems a good idea for identifying the threshold between micro- and macroscale (or better confined and unconfined bubble flow), simply it does not work in microgravity. In fact when g tends to zero, Eo is by definition less than 1.6. In Figure 29 and in Figure 30 the threshold diameters between macro and micro, calculated in according to the Eötvos number criterion [17], are presented with a residual gravity equal to 0.01g.

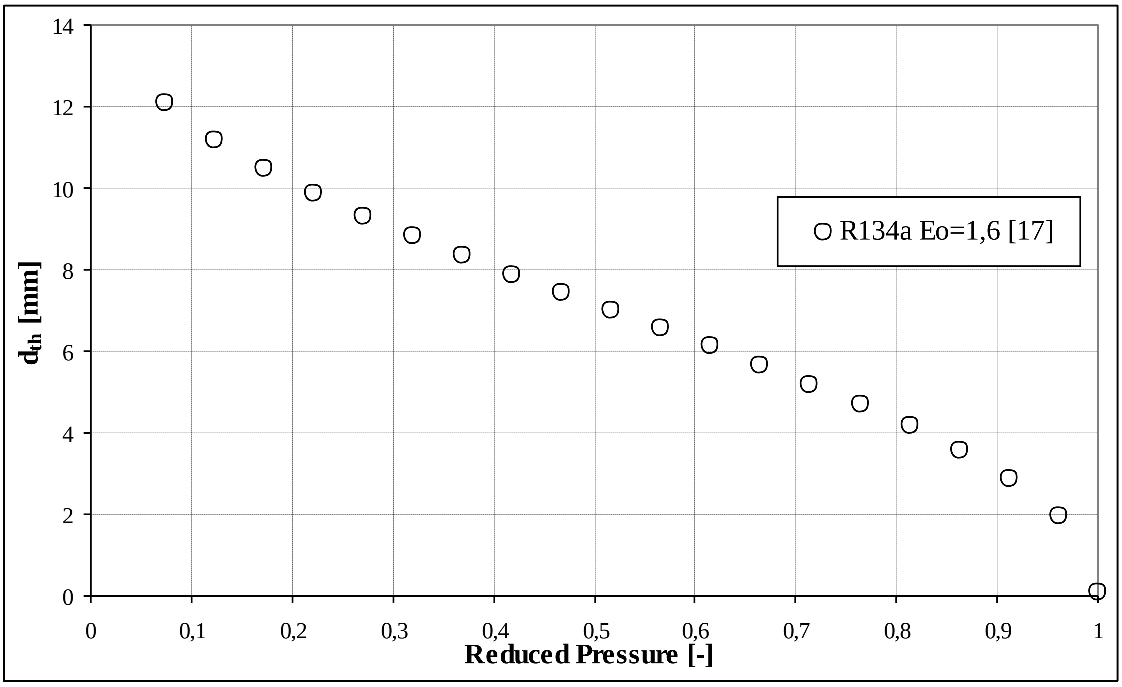

Figure 29 Threshold hydraulic diameter, calculated according to the Ullman and Brauner criterion [17] *as a* function of reduced pressure for R-134a with a residual gravity equal to 0.01 g

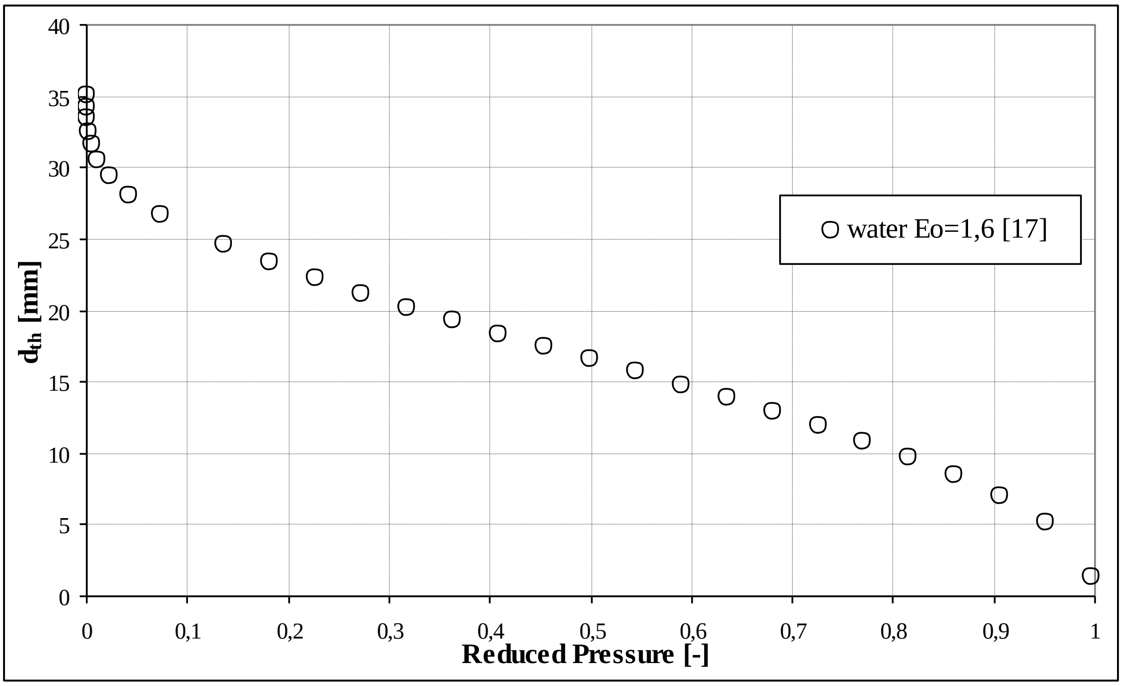

Figure 30 Threshold hydraulic diameter, calculated according to the Ullman and Brauner criterion [17], *as a* function of reduced pressure for water with a residual gravity equal to 0.01 g

It is paradoxically to see from Figure 30 that in microgravity, with water, the “microscale” regime should occur for a channel diameter of 30 thousands microns, confirming that the actual distinction between micro and macroscale has to do more with flow patterns than with real scales.

Applying the criterion based on Eötvos number [17] for classify the micro to macro transition, in Figure 31 appears that all the microgravity experimental tests examined in this review have an hydraulic diameter that is below the threshold diameter.

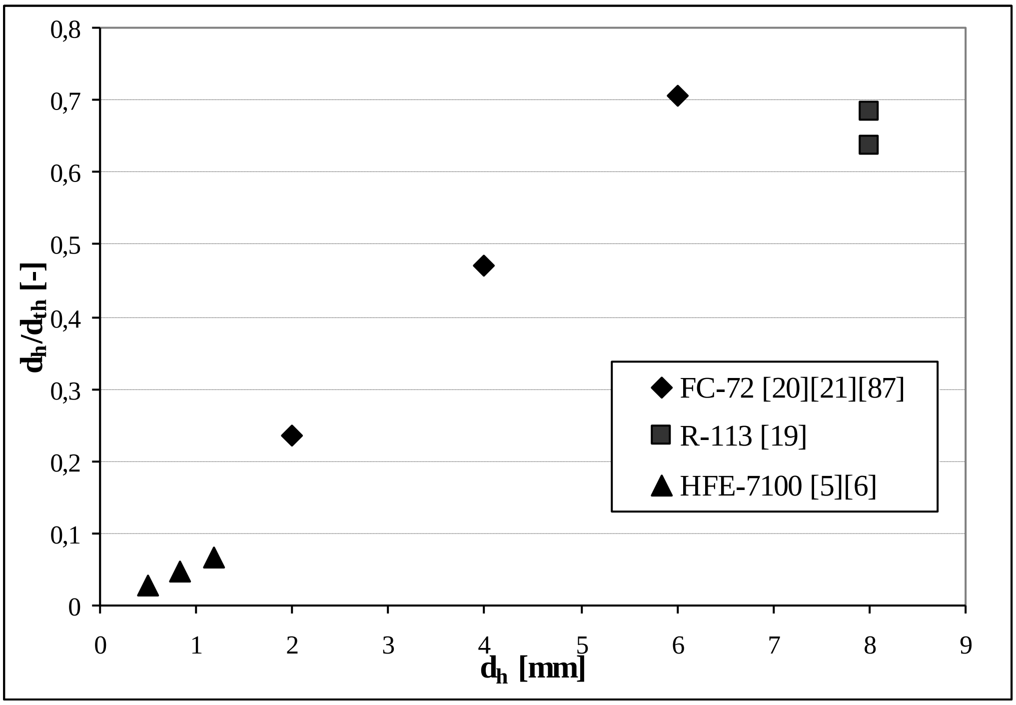

Figure 31 Comparison between the experimental hydraulic diameters and the threshold diameter of Ullman and Brauner [17]

The Ullman and Brauner criterium for macro to micro transition [17] is not valid in microgravity; in fact recent experiments of flow boiling in microgravity by Celata et al. [20] have evidenced that there are also macroscale behaviour in microgravity.

In order to understand if the Ga criterion could be considered valid in microgravity conditions, Figure 32 presents the Eo and Ga numbers associated to the microgravity database presented in this paper.

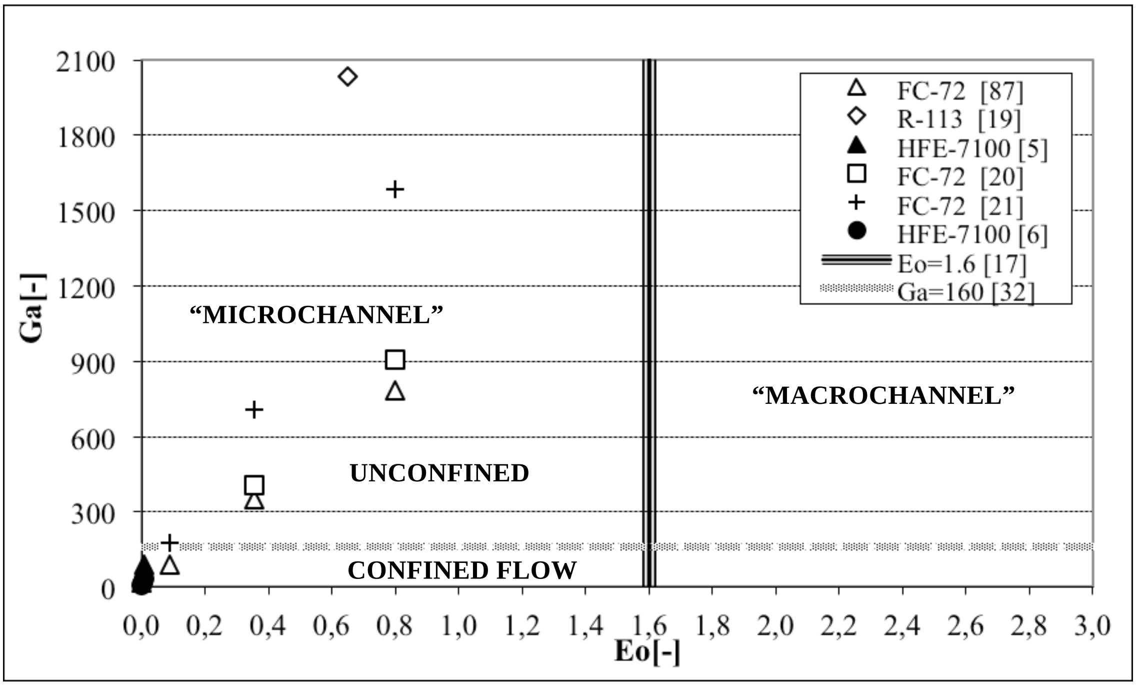

Figure 32 Convective confinement number vs. Eötvös number map for microgravity literature data.

It emerges that only the experimental data from Luciani et al. [5, 6] can be considered as microscale according to also Ga criterion [32]. The experimental work by Celata et al. [21,87] can be classify as microscale or as macroscale depending on the specific testing conditions; in fact only the data corresponding to the lower internal diameter, i.e. 2 mm, satisfy the convective confinement number criterion [32].

In [5] there is no flow pattern investigations while in [6] Luciani et al. observed only an evolution of the bubble structure from slug to churn flow in microgravity conditions and no more flow patterns. Celata et al. in [21,87] do not evidenced the flow pattern correspondent to the 2 mm internal diameter and so it is not possible to verify if it corresponds to the confined flow according to the Ga criterior.

This criterion seems to be valid in microgravity, but there is still the necessity of more complete tests in order to establish if the range of values of Ga that is able to characterize the transition macro to microscale could be applied to microgravity to characterize the confined flow.

3.2.1 The wettability effect and a new dimensionless number: the ratio between the adhesion and drag forces

A new dimensionless number, defining the ratio between the adhesion force and the drag force is proposed here in order to better represent the effect of drag on bubble nucleation, i.e. to help understanding when the drag force is enough strong to detach a bubble. In microgravity situations in particular, where the drag force is the only responsible force for the detachment, such dimensionless number is correlated with the possibility that a bubble departs from the nucleate site. The drag force is defined as $C_D \frac{\pi}{2} \rho_L r_b^2 j_L^2$ where $C_D \approx \mathrm{Re}_L^{-1}$ while the adhesion force is $2\pi r_b \sigma \left| \cos\theta_{adv} - \cos\theta_{rec} \right|$[8], where the contact angles are represented in Figure 33.

---

[8] θ_{adv} e θ_{rec} are the advancing and receding contact angles as in Figure 33.

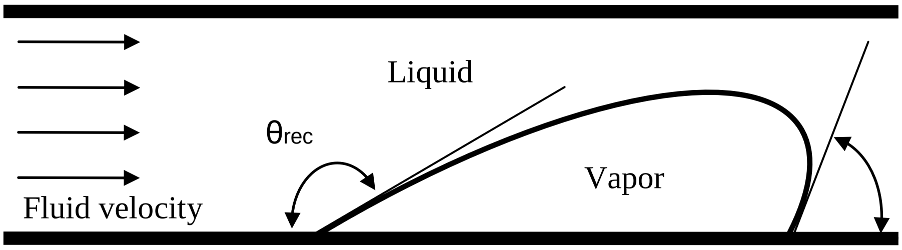

Figure 33 Advancing and receding contact angles

The ratio between these two forces is therefore:

$$\frac{F_{adh}}{F_{drag}} = \frac{2\pi r_b \sigma \left|\cos\theta_{adv} - \cos\theta_{rec}\right|}{C_D \frac{\pi}{2} \rho_L r_b^2 j_L^2} = \frac{4\sigma \left|\cos\theta_{adv} - \cos\theta_{rec}\right| \mathrm{Re}_L}{\rho_L j_L^2 r_b} = K_{emp}$$

When $2r_b \approx d_h$ it is possible *to push* the bubble for almost any liquid velocity, but when $\frac{d_h}{r_b} >> 1$ the adhesion force may dominate and the bubble scarcely moves under the drag force effect. In *the* case of large tubes, it is the local liquid velocity around the bubble which plays the determinant role, together with any bulk force such as gravity.

Setting the ratio between the adhesion and drag forces equal to unity (K_{emp} =1), it is possible to define a “drag length” or “critical bubble radius” as:

$$l_{drag} = r_{b,critical} = \frac{4\sigma \left|\cos\theta_{adv} - \cos\theta_{rec}\right|}{\rho_L j_L^2} \mathrm{Re}_L$$

The authors call $r_{b,critical}$ the bubble radius for which K_{emp} is equal to 1. K_{emp} will be a function of the liquid flow dynamics around the bubble and should be defined in future studies; therefore l_{drag} will be considered here as more adapt to a general discussion. If $r_b > l_{drag}$ the bubble detaches from the surface, that means that drag force plays the dominant role, while when the adhesion force dominates, $r_b < l_{drag}$ and the bubbles can not move only under the drag force. Physically for a bubble moving in a channel having hydraulic diameter d_h, $r_b \leq d_h$. Using the expressions defined in section 2.1.2 and 2.1.4. for Re_L and j_L, l_{drag} can also be calculated as:

$$l_{drag} = \frac{4\sigma \left|\cos\theta_{adv} - \cos\theta_{rec}\right| \rho_L d_h}{\mu_L G(1-x)}$$

Remembering that, since the maximum size of the bubble cannot exceed the channel diameter, $l_{drag} \leq d_h$, hence it is possible to study the detachment of the bubble due to the drag force only for $l_{drag}/ d_h \leq 1$, i.e. for enough high values of G(1-x), while for $l_{drag}/ d_h > 1$ only bubbles with the same radius as the channel diameter can be dragged away. In Figure 33 the behaviour of l_{drag}/d_h is plotted as a function of G(1-x). The region with very small values of l_{drag}/ d_h will correspond to bubbly flow regime even in microgravity conditions since the bubbles nucleate and the drag force can detach them. In Figure 34 T_{sat} and θ_{adv} e θ_{rec} are fixed. For an increasing surface tension, the drag length increases.

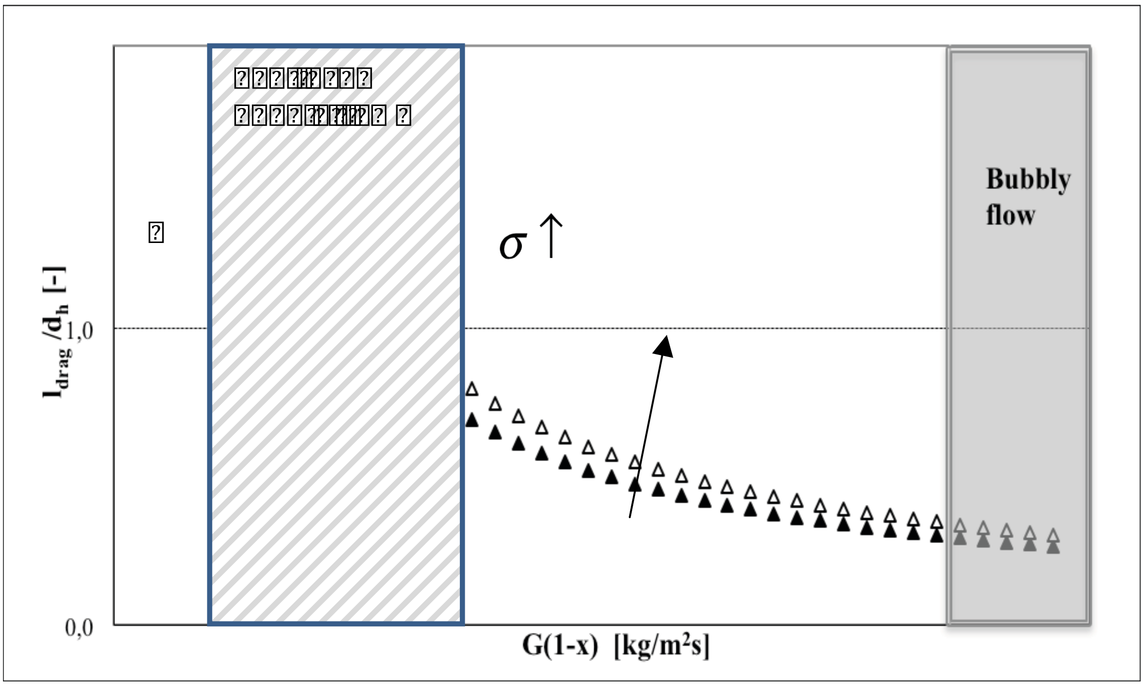

Figure 34 Qualitative behaviour of l_{drag}/ d_h as function of G(1-x) with the increase of the surface tension. When the dimensionless bubble radius r_b/d_h is higher than l_{drag}/ d_h the bubbles will detach under the effect of liquid drag only. In the box on the left the condition is that the minimum bubble size to have drag detachment becomes equal to the channel diameter.

In Figure 35 the behaviour of l_{drag}/d_h is plotted for different fluids and also the maximum value of this ratio is represented. The fluids considered are R134a and R245fa [35], FC-72 [20], with properties correspondent to temperatures of 308 K, 308 K and 348 K respectively, and advancing and receding contact angles values of 6° and 3° for an interface refrigerant-glass [36].

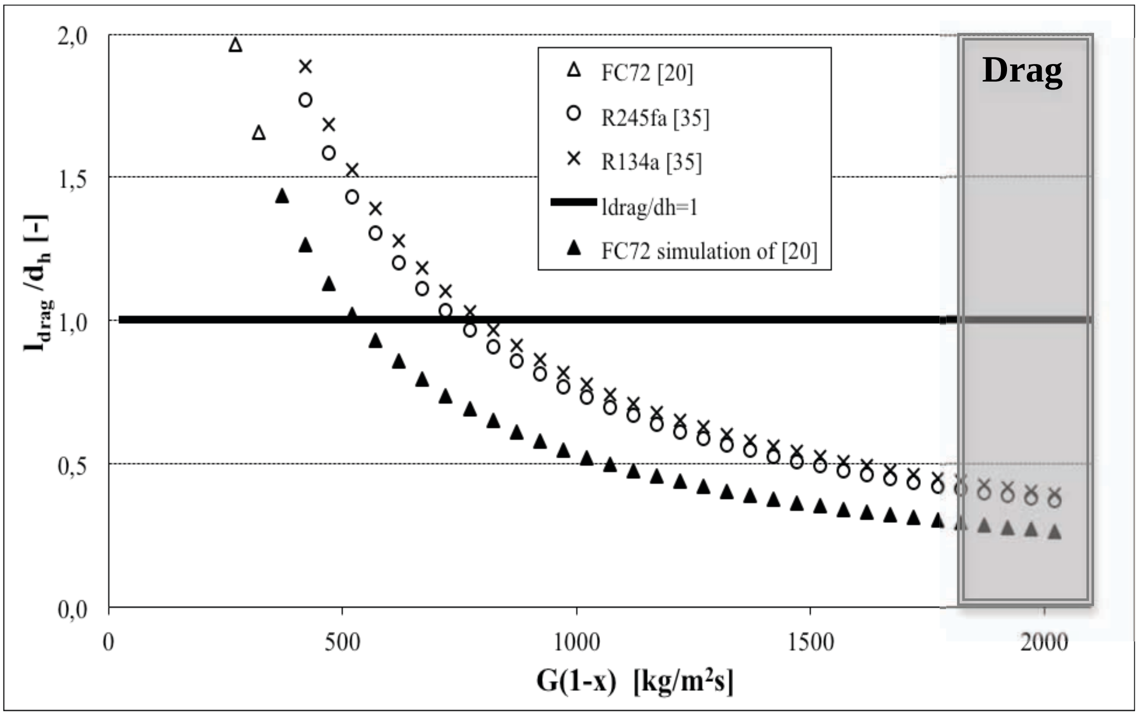

Figure 35 The behaviour of l_{drag}/ d_h plotted for different fluids as function of G(1-x), considering advancing and receding contact angles values of 6° and 3° typical for a refrigerant on glass.

In Figure 35, the very small values of l_{drag}/ d_h correspond to the region where the drag force largely dominates; in Figure 34 it is also evidenced that in this same region bubbly flow occurs, since the drag force can immediately detach the bubbles. For FC-72 the bubble cannot detach from the surface for the mass flux values used in the experiment [20], i.e. G<355 kg/m^{2}s. In the range 355<G<2000 kg/m^{2}s the solid triangles symbols are only simulated. From the simulations, below G<500 kg/m^{2}s the bubbles will not detach. The use of advancing and receding contact angles values of 6° and 3° for refrigerants-glass, stress the importance of *a* low value of hysteresis [37] to obtain that the drag force can dominate the adhesion force.

In order to understand the relative importance of drag forces with respect to buoyancy, future experiments in microgravity should be carried on with the aim of mapping slug and bubbly flows as a function of l_{drag} for the different experimental conditions.

In 2007 Celata et al.[20] provided evidence that there is also macroscale behaviour in microgravity; they describe the results of an experimental investigation on the flow patterns of FC-72 with two different inner diameters of the test section; a Pyrex tube 4 mm and 6 mm in diameter. The absence of buoyancy force among the forces acting on a bubble during their nucleation, growth and detachment on the heated wall, causes a longer period of growth and, therefore, a larger diameter at the detachment. Therefore, the gravity level affects both bubble size and shape, but such functional dependence is also interrelated with vapor quality and with fluid velocity. In 2008 Celata [38] suggested that a further parameter, the drag force, should be taken into account for a wider validity of the threshold identification. In fact if drag force is predominant over buoyancy, bubble size in microgravity is expected to be similar to the terrestrial gravity value. If these two forces are of the same order of magnitude the bubble size has to be larger to allow the drag force to detach the bubble, considering also that buoyancy is missing in microgravity. Gravity level is therefore expected to have an impact on bubble size and shape when fluid velocity is lower than a critical value while when the fluid velocity is bigger than this value, the gravitational effects becomes unimportant.

We may also consider that in microgravity, for experiments with water, which has an inherent high hysteresis on many materials and high surface tension, the flow will be mostly a confined bubble flow, since the l_{drag} will tend to be large, i.e. the bubbles will nucleate and then grow until to fill the whole size of the channel. Only very high mass flow rates G are likely able to produce bubbly flows.

Chapter 4

Flow boiling heat transfer in microchannels

Differently from single-phase flow heat transfer, the current knowledge of flow boiling heat transfer in macroscale cannot be extended tout-court to microscale, where bubble confinement plays a more relevant role with the decreasing of the channel size. It is then necessary to use a new heat transfer method that incorporates features of the physical process of microchannel flow and evaporation.

4.1 HEAT TRANSFER MECHANISMS

Flow boiling heat transfer consists of a nucleate boiling component, resulting from the nucleating bubbles and their subsequent growth and departure at the heated surface, and a convective boiling component, resulting from the convective dynamic effect. In Kandlikar's opinion [3] these two mechanisms are closely interrelated.

Presently, researchers are divided into two groups, one considering that nucleate boiling is prevailing and the other asserting that convective boiling is the dominant heat transfer mechanism. Several recent studies try to shed light on this dispute and they are summarized in [29,*39*], but until now the dominant heat transfer mechanism inside mini and micro channels is still an open question. Since the two-phase flows are often in a non-equilibrium conditions (oscillation, regime variations, lack of fully developed conditions) it could be better to define a time and space averaged coefficient, called HTC, heat transfer coefficient, rather than a convection coefficient, which is directly linked to the Newton laws, i.e to equilibrium, stationary conditions. Since many papers are referring in any case to a convection coefficient, we respect this tradition, underlining that the meaning of “h” is, for flow boiling, not appropriate.

In the nucleate boiling regime the heat transfer coefficient is a function of the heat flux and system pressure, but is independent of vapor quality and mass flux. In the convective boiling regime the heat transfer coefficient depends on vapor quality and mass flux, but is not a function of heat flux.

In [29] there is a microscale heat transfer database including the heat transfer trends; in most of the papers included in the database, nucleate boiling has been suggested to be the dominant heat transfer mechanism in microscale channels. Thome [27] asserts that this last statement is not true and originates from the misconception that an evaporation process depending on the heat flux necessarily means that nucleate boiling is the controlling mechanism. Thome underlines also that another diffuse inaccuracy is to simple label microchannel flow boiling data as being nucleate boiling dominated, only because this seems to be the case for the bubbly flow regime, which occurs at very low vapor qualities [27]. Furthermore experimental flow boiling studies, reporting that nucleate boiling was dominant at low x, equally show that the flow regime observed at such conditions was elongated bubble flow and such two conclusions are then contradictory. Many empirical prediction methods for boiling in microchannels are essentially modifications of macroscale flow boiling methods and thus assume that nucleate boiling is an important heat transfer mechanism without proof of its existence as the two principal microchannel flow regimes are in fact slug and annular flow [27].

Also Celata [38] asserts that many researchers have addressed their experimental results in microscale as governed by the nucleate boiling or the convective boiling regime, depending on the heat transfer coefficient trend only as a function of thermal-hydraulic parameters. Table 2 gives a summary of the microscale flow boiling heat transfer mechanisms available in literature.

Author	**Heat transfer mechanisms active during boiling in microchannels**
Kandlikar [3]	Nucleate boiling dominate heat transfer during flow boiling, the role of the convective boiling mechanism is diminished.
Bao et al. [40]	Nucleate boiling
Lin et al. [41]	Nucleate boiling dominated at low x, convective boiling at high x.
Yen et al. [42],	Bubble nucleation only occurred when x < 0.4. x = 0.4 is considered to be the x critical for nucleate and convective boiling dominance in microchannels.
Jacobi and Thome [43]	Transient evaporation of a thin liquid films in slug flow
Thome [27]:	- In bubbly flow, nucleate boiling and liquid convection - In slug flow, the thin film evaporation of the liquid film trapped between the bubble and the wall. The liquid convection to the slug and vapor

	convection, when there is a dry zone present, are also important, depending on their relative residence times. - In annular flow, convective evaporation across the liquid film - In mist flow, vapor phase heat transfer with droplet impingement
Cheng et al. [44]	- Nucleation mechanism near the onset of boiling at upstream of the microchannels - Film vaporization (convective boiling) in the Taylor bubble and annular flow at downstream.
Lee et al. [39]	- Heat transfer is associated to different mechanisms depending on the vapor quality - Nucleate boiling occurs at low qualities (x<0.05) - Annular film evaporation dominate at medium quality (0.05<x<0.55) and at high quality (x>0.55).
Harirchian and Garimella [45]	- Nucleate boiling for unconfined flow - Evaporation of the thin liquid film dominate in the confined flow

Table 2 Summary of heat transfer mechanisms in microscale flow boiling as described in literature

Jacobi and Thome [43] have shown that nucleate boiling is not the dominant heat transfer mechanism and that the heat flux effect can be explained and predicted by the thin film evaporation process occurring around elongated bubbles in the slug flow regime without any nucleation sites. They states that transient evaporation of a thin liquid films surrounding elongated bubbles is the dominant heat transfer mechanism in slug flow and the model described in [26] is able to predict the heat transfer data for different liquids without including nucleate boiling. The mechanisms concerning the development and the progression of a liquid-vapor interface through a minichannel are still unclear; hence, the complete picture of the "heat transfer map" for flow boiling heat transfer in microchannel has not yet been established [25].

In [46] the experimental heat transfer coefficient for deionized water in a single microchannel (d_h=100μm) is found to be independent on G and vapor quality. Though this behaviour seems to suggest nucleate boiling as the dominant heat transfer mechanism, the major flow pattern is similar *to* annular flow, which does not present *h* independent of *G* and *x*. This discrepancy is attributed to the fast and long elongated bubbles that grow from single bubbles in a microchannel; the continuous supply of heat through the thin liquid film speed up the continual growth of elongated bubbles and finally create an annular flow [46]. There are other visual investigations which testify the occurrence of the annular flow regime, which would not support the nucleate boiling mechanism, even for low values of the vapour quality (this being interrelated with the size of the diameter), such as Revellin and Thome [47], who conducted experiments of flow visualization of R-134a and R-245fa inside 0.5 and 0.8 mm diameter pipe.

In 2008 Celata [38] underlined that there are still a number of open issues which have to be addressed in order to have a clearer picture of the boiling heat transfer mechanisms in microchannel; they can be so summarized *as*:

- If nucleate boiling is the dominant regime, then the surface finish of the microchannel should be measured and reported due to its importance on the heat transfer;
- data benchmark with the same fluid, same tube diameter, same test conditions, has to be carried on to double check the universality of the data;
- if the pressure drop is large in the test sections, as it is often the case, then the flashing effect on the enthalpy change has to be taken into account when determining and reporting the local vapor quality;

- the influence of the test section fluid inlet conditions on the measured data has not yet been thoroughly ascertained; two-phase flow structure inside the microchannel can be affected by subcooled boiling prior the test section entrance;
- most of the data regarding the visualisation study in two-phase flow comes from the adiabatic part of the glass transparent tube[9]. It would be useful having more information about the phenomena occurring inside the diabatic zone of the tube from the visualization of boiling heat transfer; using indium-tin-oxide coating, enabling joule effect heating and simultaneous visualisation, is encouraged for a better physical insight.

In 2011 Harirchian and Garimella [48] summarize their recent experimental investigations and analyses on microchannel flow boiling. They gave answers to some of the issues above and from [48] it emerges the importance of extensive experimental work in order to reach a more comprehensive understanding of the microchannel flow boiling. This include heat transfer mechanisms, flow regime maps based on flow pattern visualizations, quantitative criteria for the transition macro to microscale, the effects of important geometric and flow parameters on flow regimes and heat transfer coefficient. A state of the art of the research on these points is the purpose of the next sections.

4.2 BOILING MODELS

As already remarked in paragraph 3.1, Jacobi and Thome [17] demonstrated that the transient thin film evaporation and not nucleate boiling is the dominant heat transfer mechanism. Moreover they showed that the heat flux dependence of the heat transfer coefficient can be explained and predicted by the thin film evaporation process occurring around elongated bubbles in the slug flow regime without

---

[9] Usually the heaters are opaque; hence the camera for visualization is positioned just after the heater

any nucleation sites. They proposed an analytical “two-zone” model to describe evaporation in microchannels in the elongated bubble (slug) flow regime and they showed that the thin film heat transfer mechanism along the length of the bubbles was very dominant compared to the liquid convection occurring in the liquid slugs; their model predicted that the two-phase flow boiling heat transfer coefficient is proportional to q^n, where q is the heat flux and n depended on the elongated bubble frequency and initial liquid film thickness laid down by the passing bubble. So the thin film evaporation heat transfer mechanism, without any local nucleation sites in slug flows, yields the same type of functional dependency as the boiling curve. Afterwards Thome et al. [26] and Dupont et al. [**49**] developed a new three-zone elongated bubble flow model for slug flow. They proposed the first mechanistic heat transfer model to describe evaporation in microchannels with a three-zone flow boiling model that describes the transient variation in the local heat transfer coefficient during sequential and cyclic passage of (i) a liquid slug, (ii) an evaporating elongated bubble and (iii) a vapor slug when film dryout has occurred at the end of the elongated bubble.

The main assumptions that have been made in developing the model for the elongated bubble flow are:

- the d_0, the initial thickness of the liquid film, is very small if compared with the inner radius of the channel;
- vapor and liquid travel at the same velocity;
- the heat flux is uniform and constant;
- the fluid is saturated liquid at the entrance of the channel;
- vapor and liquid remain at saturation temperature, neither the liquid nor the vapour is superheated.

This phenomenological model contains five empirical constants: three to predict the bubble frequency, one to set the film dryout thickness dmin, and one to correct the method they use to predict the initial film thickness do. Their values were determined using a broad heat transfer database derived from the literature covering seven fluids[10]. The model has three adjustable parameters that will be determined from comparison with experimental data: dmin[11], assumed to be on the same order of magnitude as the surface roughness – mainly unknown in the experimental studies, Cdo, the empirical correction factor on the prediction of do, fp, the triplet frequency[12], that is a complex function of the bubble formation and coalescence process. Figure 36 depicts a schematic of the model that illustrates the strong dependency of heat transfer on the bubble frequency, the length of the bubbles and liquid slugs and the initial liquid film thickness and its thickness at dryout.

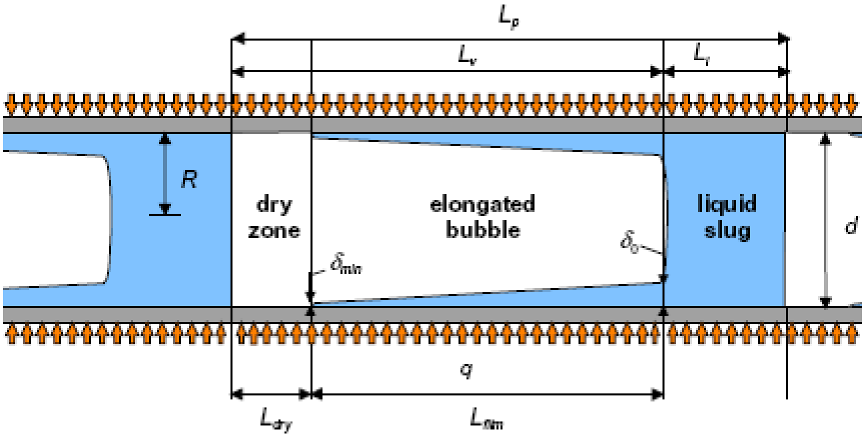

Figure 36 Three-zone heat transfer model for elongated bubble flow regime in microchannels: diagram illustrating a triplet comprised of a liquid slug, an elongated bubble and a vapor slug.

In the three-zone, film evaporation is postulated as originating by pure conduction through the film thickness with no presence of bubble nucleation. Thus the authors claimed that the slug flow heat transfer coefficient is governed by thin film evaporation. The three-zone model

---

[10] R-11, R-12, R-113,R-123, R-134a, R-141b, CO_2.

[11] From [49] the specific values of δ_{min} ranged from 0.01 to 3 μm.

[12] See note 4 to understand the meaning of “triplet”.

predicts the heat transfer coefficient of each zone and the local time-averaged heat transfer coefficient of the cycle13 at a fixed location along a microchannel during evaporation of an elongated bubble, at a constant, uniform heat flux boundary condition [27]. The input parameters required by the model are: the local vapor quality, the heat flux, the internal diameter, the mass flow rate and the fluid physical properties at the local saturation pressure. This model so far only covers heat transfer in the elongated bubble (slug) flow regime with and without intermittent dryout; even if this is the most dominant flow regime in microchannels, there are other patterns, such as the annular flow, and so further extensions of the model at least to annular flow are necessary (see also section 5.3 for a comparison of the different regimes).

Visual investigations showed the occurrence of the annular flow regime even for low values of the vapor quality [50] and Agostini and Thome [51] have made a preliminary extension to annular flow. Harirchian and Garimella [52] proposed flow regime-based models for prediction of heat transfer coefficient in the annular and annular/wispy-annular regions while they suggest the empirical correlation of Cooper [53] for the bubbly flow and a modified three zone model of Thome et al. [26] for the slug flow region. In the modified model [52] the value of the surface roughness are used for dmin and the values of the other four parameters are optimized; the predictions of this modified model show good agreement with the slug flow experimental data [52].

A physical and mathematical heat transfer model for constant wall temperature and constant heat flux boundary conditions has been developed by Whan Na and Chung [54] for annular flow. Cioncolini and Thome are working on the development of the heat transfer model in annular flow; in 2011 they present a turbulence model [55] that is part of a unified annular flow modeling suite that includes methods to

---

[13] The cycle is: a liquid slug, an elongated bubble and a vapor slug; it is a sort of “triplet” and a new cycle begins with the next liquid slug.

predict the entrained liquid fraction [56] and the axial frictional pressure gradient [57].

Several comparison of the three-zone flow boiling model have been made against independent experimental results; in Figure 37 and in Figure 38 from [49], the results of Bao et al. [40] are well predicted by the model.

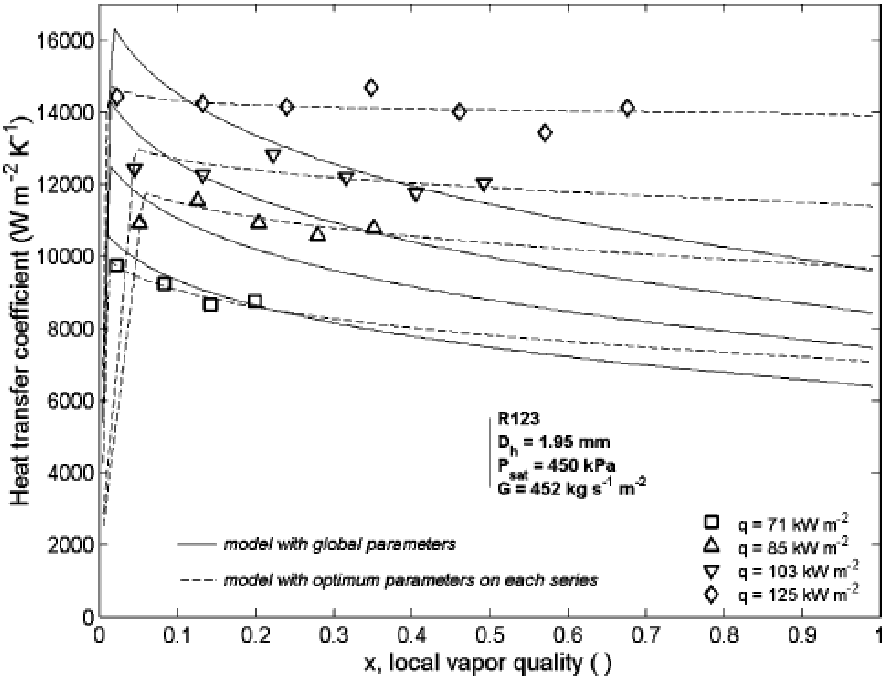

Figure 37 The experimental measurements of local heat transfer coefficient as a function of vapor quality for R-123 in 1.95 mm tube [40] are compared with the prediction of the model [26] **Eo=5.18**

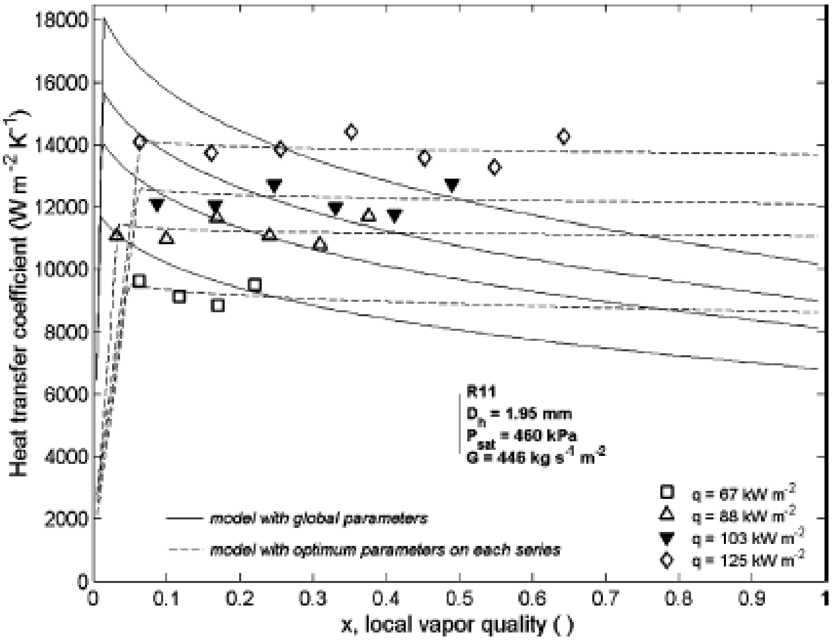

Figure 38 The experimental measurements of local heat transfer coefficient as a function of vapor quality for R-11 in 1.95 mm tube [40] are compared with the prediction of the model [26] **Eo=4.26**

However in [29] and [58] it is evidenced that this model, with its general empirical constants [49], only predicts 45% of the experimental points within ±30%. Future works, carried on as a combined two-phase flow/two-phase heat transfer study are still necessary [58].

Some others comparison between experimental data and three-zone model prediction are reported in [15], [59], [60]. The observed characteristics of the heat transfer coefficient h in [15], see Table 3 in 4.3.1, are similar to those conventionally interpreted as evidence that flow boiling in large tubes is dominated by nucleate boiling; however, the three-zone evaporation model [26] suggests that, for small channels, the same behaviour can be explained if transient evaporation of the thin liquid film surrounding elongated bubbles, without nucleate boiling contribution, is the dominant heat transfer mechanism.

In [15] it is underlined that the mechanistic three-zone evaporation model [26] for higher vapor quality x, the heat transfer coefficient h becomes independent of q'' and it decreases with x; this could be caused by partial (intermittent) dryout but the model [26] does not predict the conditions of the decreasing of h, which experimentally occurred at high x as for example in Figure 39. In this figure [15] the experimental measurements of local heat transfer coefficient as a function of x are compared with the prediction of the model [26]. Althought the three zone model [26] should only be used in the slug flow regime for which it was developed, it was found [15] that the model [26] can make satisfactory predictions at qualities expected to be in the annular flow regime, up to the onset of partial dryout. The churn/annular transition boundary shown in Figure 39 is predicted by Chen et al. regime maps [16] and it indicates the extension of the model prediction in the annular regime; further investigation *is* required because there may be some differences between the flow conditions within the heated test section [15] and those observed in an adiabatic section following the test section [16]. The model overpredicts h for the 4.26 mm tube for the entire range, with the difference between the experimental and model data that increases with increasing q''. The effect of q'' on the experimental h gets smaller as q'' is increased; this is not well predicted by the model. Also for the 2.01 mm tube, the prediction is better at lower heat flux values and the data is again over-predicted as q'' increases.

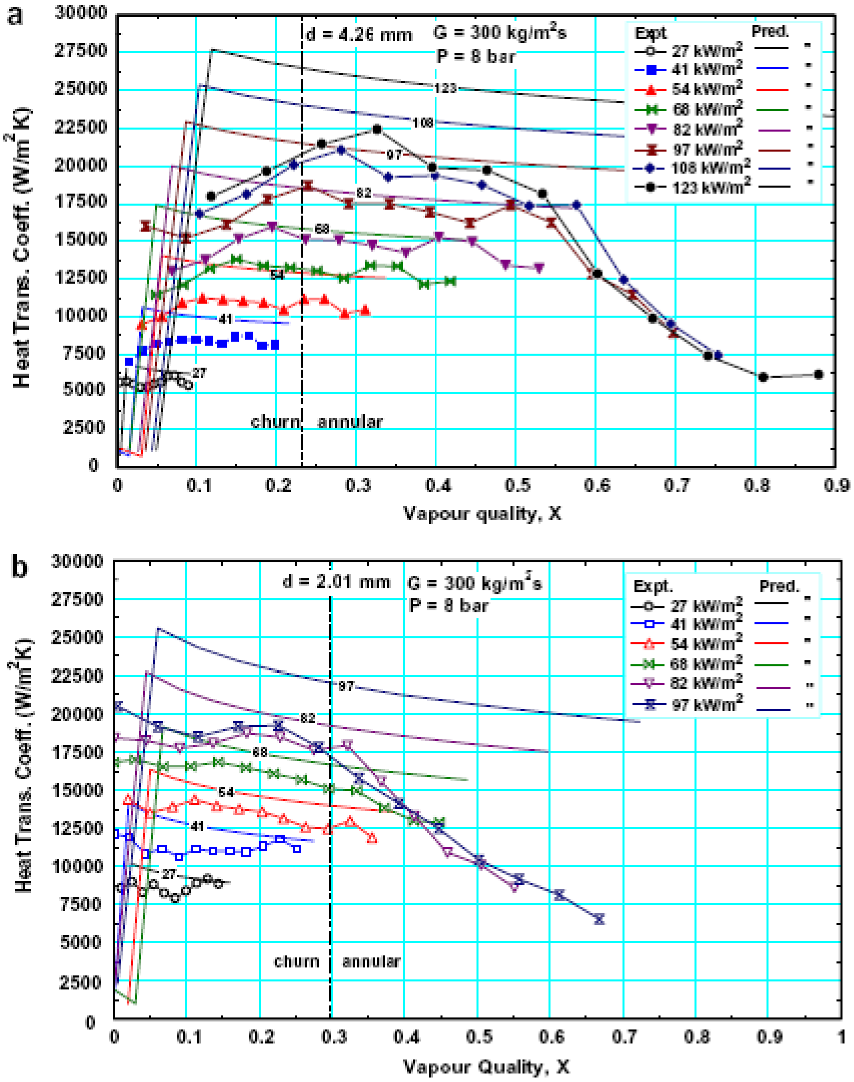

Figure 39 Comparison of the experimental local heat transfer coefficient versus vapor quality [15] with the three-zone model [26] for various heat flux values and P = 8 bar:(a) d = 4.26 mm, **Eo= 28.1**(b) d = 2.01mm, **Eo=6.26**

Shiferaw et al. [60] presented another detailed analysis of the three-zone evaporation model in 2009; they underlined that the three zone model [26] predicts fairly well the 1.1 mm tube heat transfer results at low quality, especially the low pressure results, that are experimental data that would be interpreted conventionally as nucleate boiling. In [60] there is also a good prediction14 of the three zone model with experimental data in the case in which dryout appeared to occur early at low quality. However, the model can not predict the decreasing heat transfer coefficients at high qualities near the exit of the test section, attributed to dryout; further studies are necessary in order to find an independent evaluation of the three parameters necessary to make the model self-sufficient and to improve the partial dryout model [60].

Consolini and Thome in 2010 [61], maintaining the purely convective boiling nature suggested in the three-zone model, include coalescence in the description of the thin evaporating film and thus account for its influence on heat transfer. They presented a simplified analysis of one-dimensional slug flow with bubble coalescence [61]. In [62] the coalescence of two bubbles into an elongated bubble was observed in parallel multiple microchannels; this paper underlines how a previously formed vapour slug can influence the growth of following bubbles and their behaviour.

Coalescing bubble flow has been identified as one of the characteristic flow patterns to be found in microscale systems, occurring at intermediate vapor qualities between the isolated bubble and the fully annular regimes.

---

[14] This prediction of dryout has been done when critical film thickness is made almost equal to the measured average roughness of the tube (1.28 μm) and the other two parameters are $C_{\delta 0}$ set to 2.2 times its standard value (from the database in [49] the standard value is equal to 0.29), and the bubble generation frequency set to 1.75 times the value recommended by Dupont et al. [49].

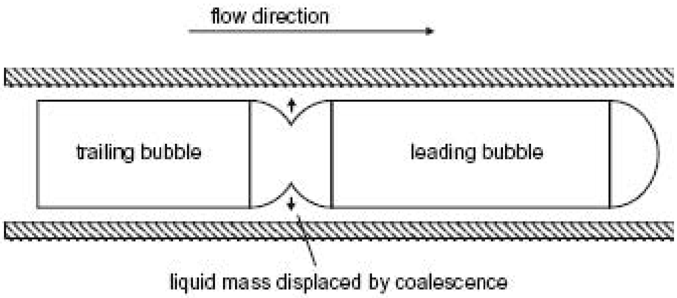

Figure 40 Schematic diagram of coalescence of two bubbles [61]

In fact, within the general classification of slug flow, Revellin and Thome [35] and more recently Ong and Thome [63], segregated the regimes into an isolated bubble flow and a coalescing bubble flow in the range of vapor qualities, where the characteristic bubble frequency reduces from a peak value to zero (representing the transition to annular flow)[15]. During coalescence, the breakup process of the liquid slugs induces a redistribution of liquid among the remaining flow structures, including the film surrounding individual bubbles; the effects of bubble coalescence and thin film dynamics are included in this micro-channel two-phase heat transfer model.

The new model [61] has been confronted against experimental data taken within the coalescing bubble flow mode, identified by a diabatic microscale flow pattern map. The comparisons for three different fluids (R-134a, R-236fa and R-245fa) gave encouraging results with 83% of the database predicted within a ±30% error band. In the model the equations are based on flow patterns and thus rely on the accuracy of the adopted flow pattern map to identify the coalescing bubble flow

---

[15] In general terms, the frequency presents a maximum value, f_{max}, at the vapor quality related to the transition between the isolate bubble and coalescing bubble modes, and declines then to zero at the transition to annular flow. These two vapor qualities are denoted with x_c and x_a.

regime boundaries, i.e. x_c and x_a[16]. Since generally flow pattern transition equations are indicative more of a band of transition vapor qualities rather than an exact value, the predictions in the neighborhood of the transition boundaries may be subjected to higher errors than those that are well within the coalescing bubble flow mode.

In Figure 41 there is the comparison between the model [61] and the experimental data from [41] for R-141b; the model reproduces the increase in heat transfer with heat flux but it shows a general under-prediction of the experimental results that becomes more pronounced at the highest heat fluxes.

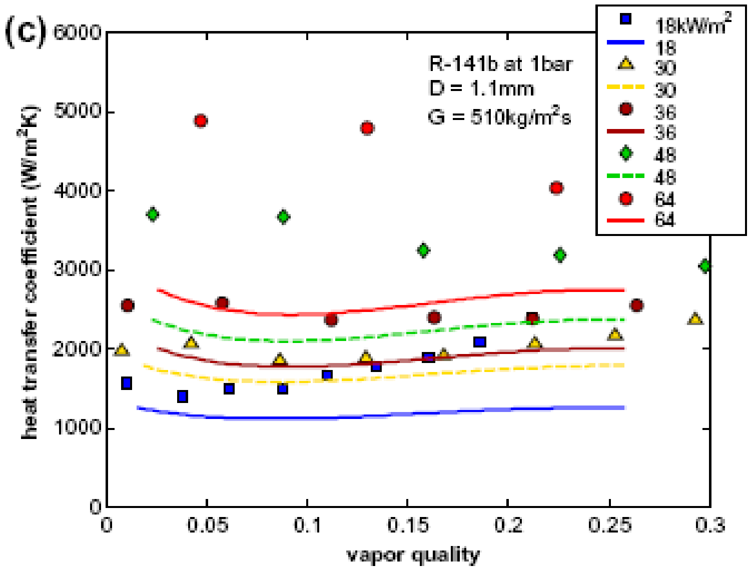

Figure 41 Experimental heat transfer coefficients [41] as function of vapor quality compared with the prediction [61] for R-141b at 1 bar and at different heat fluxes. **Eo=0.83**

---

[16] See note 15 for the meaning of x_c and x_a.

In [61] the authors assert that their approach, which has been developed for a constant heat flux, could potentially be extended to the time varying heat flux case.

Among the large number of papers which could be eventually added to the present review, some are worth of a citation: the correlations of Lazarek and Black [64] and Tran et al. [65], the empirical method of Kandlikar and Balasubramanian [66], the adaptation of Chen’s superposition model by Zhang et al. [67] and Bertsch et al. [68]. While in [64] and [65] the experimental data are correlated to the parameters that influenced the heat transfer behavior and nucleate boiling is suggested to be the dominant heat transfer mechanism, [66], [67], and more recently [68] try to revise methods originally developed for the macro-scale assuming nucleate boiling as a dominant mechanism.

4.3 HEAT TRANSFER COEFFICIENTS

4.3.1 The heat transfer coefficient versus vapor quality

In

Table 3 there is a summary of the literature results on the behaviour of heat transfer coefficient and on the different variables whose heat transfer depens on.

Authors, test fluid and test section diameter	**Heat transfer coefficient depends on:**
Bao et al. [40] R-11 and R-123,d= 1.95 mm. Figure 42, Figure 43	- q" - independent *of* G - independent *of* x
Bertsch et al. [69]	- on x; h decreases for x >0.5 - slightly on G; h increases weakly with G - on q"; h increases with it.

Consolini et al. [70] R134a, R236fa, R245fa d=510μm and d=790 μm	- h increases with q" - minimal effect of G and x on h
Dupont et al. [71] d =0.5 - 2 mm in increments of 0.166mm	- h decreases with diameter for x<0.04; - for 0.04<x<0.18 h increases, reaching a peak, and then it decreases with the diameter - h increases with diameter for x>0.18 Depending on the thermophysical properties of the fluid and the operating conditions, each zone can disappear or move as a function of quality x.
Harirchian and Garimella [45]	- the microchannel cross sectional area; h increases with decreasing cross sectional area for microchannel smaller than 0.089 mm^2 while for microchannel area >0.089 mm^2 h is independent of channel dimensions. - on q"; h increases with it.
Harirchian and Garimella [48]	- on x for R-134a; h increases with increasing of x till vapor quality of 20% after which it dropps for further increases in x. - on x for FC-77; h increases with increasing exit vapour quality until the point of dryout after which h decreases.
Huo et al. [14], R-134a d= 2.01 and d=4.26 mm	- h has a complex behaviour especially for x>0.2. The trends of h versus x are the same as in [15], but the values of h are different, as outlined

	in 2.2.
Lee et al. [39]	- on x; h decreases with it. - on q"; h increases with it.
Lin et al. [41,72] R-141b, d=1.1 mm Figure 44	- strongly on x at low and high q". At low q" h has a peak at about x=0.6. At high q" h has a peak for small x and then fell with x and becomes independent from q" - at intermediate q" is independent on x
Ong et al.[63] R134a, R236fa, R245fa d=1.030 mm Figure 49 Figure 50	- on q" at low x R245fa in a 1.030 mm channel - h increases with q" for a wide range of x for R134a and R236fa at low G - the fluid properties. In fact for low x, h for R134a is the highest followed by R236fa and R245fa reflecting their values of reduced pressure. - on G for R134a and R236fa. It appears that the transition to annular flow occurs at lower x with increasing G. h increases after the transition occurrence for both fluids
Shiferaw et al. [15] R134a , d=2.01 mm and d= 4.26 mm Figure 46, Figure 47	- on q" till x=0.5 for the 4.26 mm tube and till x=0.3 for the 2.01 mm tube. - on system pressure (h increases with the pressure) - independent on x for x<0.5 for the 4.26 mm tube and for x<0.3 for the 2.01 mm tube. - independent on G for low quality

Shiferaw et al. [60] R134a , d= 1.1 mm Figure 48	- h increases with the pressure (probably due to the fact that bubble departure diameter decreases as the system pressure increases) - on q" - for low q" and G and for x<0.5, h is independent on x
Yen et al.[42],HCFC123 d= 210 μm dh= 214 μm Figure 45	- on x - on the shaped cross-sections for x<0.4. In this range h is higher for the square microchannel because corners in the square microchannel acted as effective active nucleation sites

Table 3 Summary of the behaviour of heat transfer coefficient recently presented in literature.

In Figure 42 and in Figure 43[17] the experimental values of h are plotted versus vapor quality including the subcooled boiling data [40].

---

[17] The thermodynamic vapor quality x_{th} is given by: $x_{th} = \dfrac{h - h_{sat,L}}{h_{sat,V} - h_{sat,L}}$

where $h_{sat,L}$ and $h_{sat,V}$ are the specific enthalpy of the saturated liquid and vapor while *h* is the total specific enthalpy of the fluid which is determined from the inlet enthalpy and the heat transferred to the fluid.

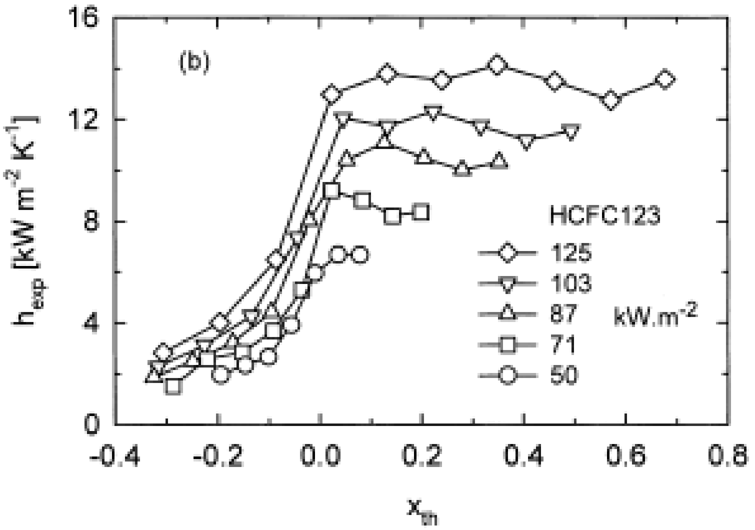

Figure 42 Plot of experimental heat transfer coefficients as function of vapor quality for R123 for different heat fluxes, with G = 452 kgm^{-2}s^{-1} and p_{inlet} = 450 kPa. **Eo=5.18**

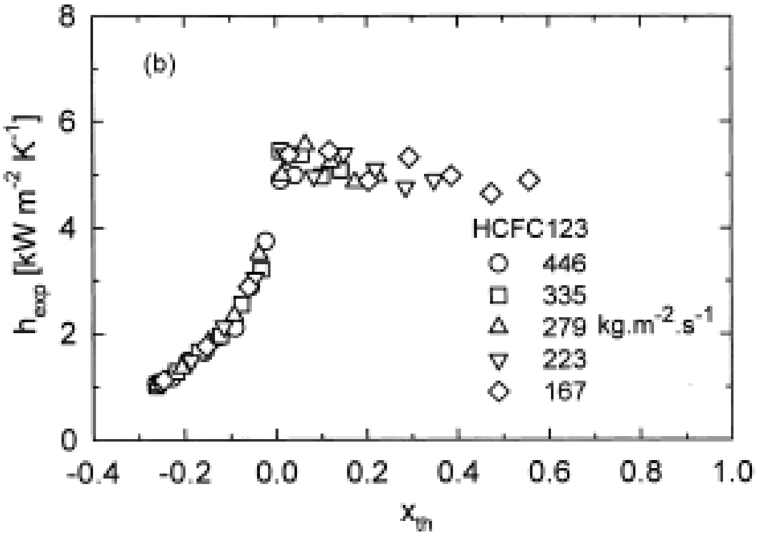

Figure 43 A plot of the experimental heat transfer coefficient versus vapor quality at different mass fluxes for HCFC123, q"=39 kWm^{-2} and p=350kPa. **Eo=4.78**

Lin et al. [72] found a complex dependency of h on q" and also on x, as presented in Figure 44.

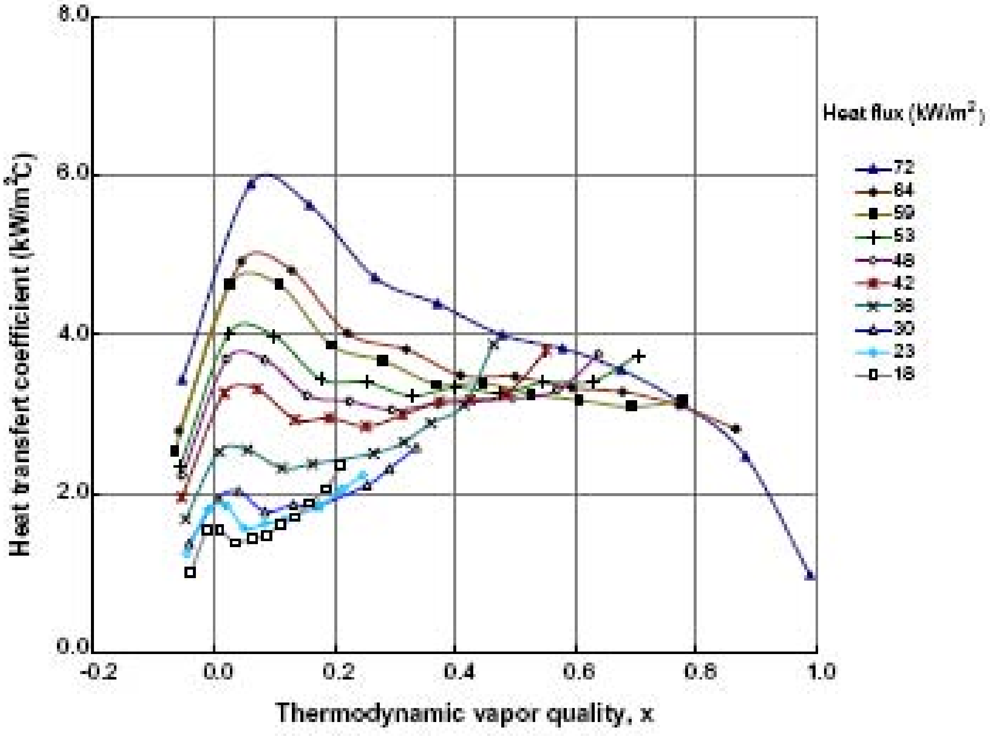

Figure 44 Flow boiling data for R-141b in 1.1 mm tube, G=510 kg/m^{2}s. **0.87 <Eo<0.96** [18]

---

[18] In [72] the saturation pressure at which these experimental data were obtained is not clear and so the authors of this review prefer to use the range of pressure 0,135-0,22 MPa declared in the paper to calculate Eo.

Yen et al. [42] presented these experimental data:

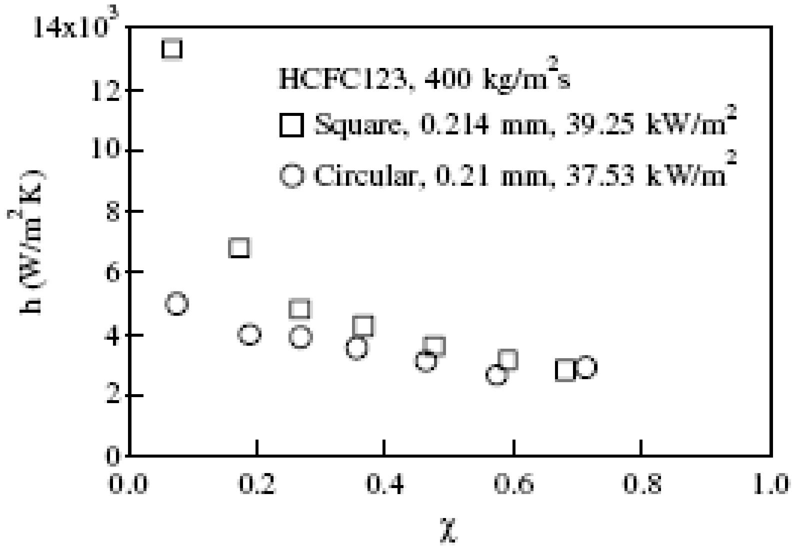

Figure 45 Local heat transfer coefficient h versus vapor quality x for different shaped cross sections at the same q and G [42]. For the circular channel **Eo=0.046**, while for the square channel **Eo=0.048**

Shiferaw et al. [15] obtained these trends for h:

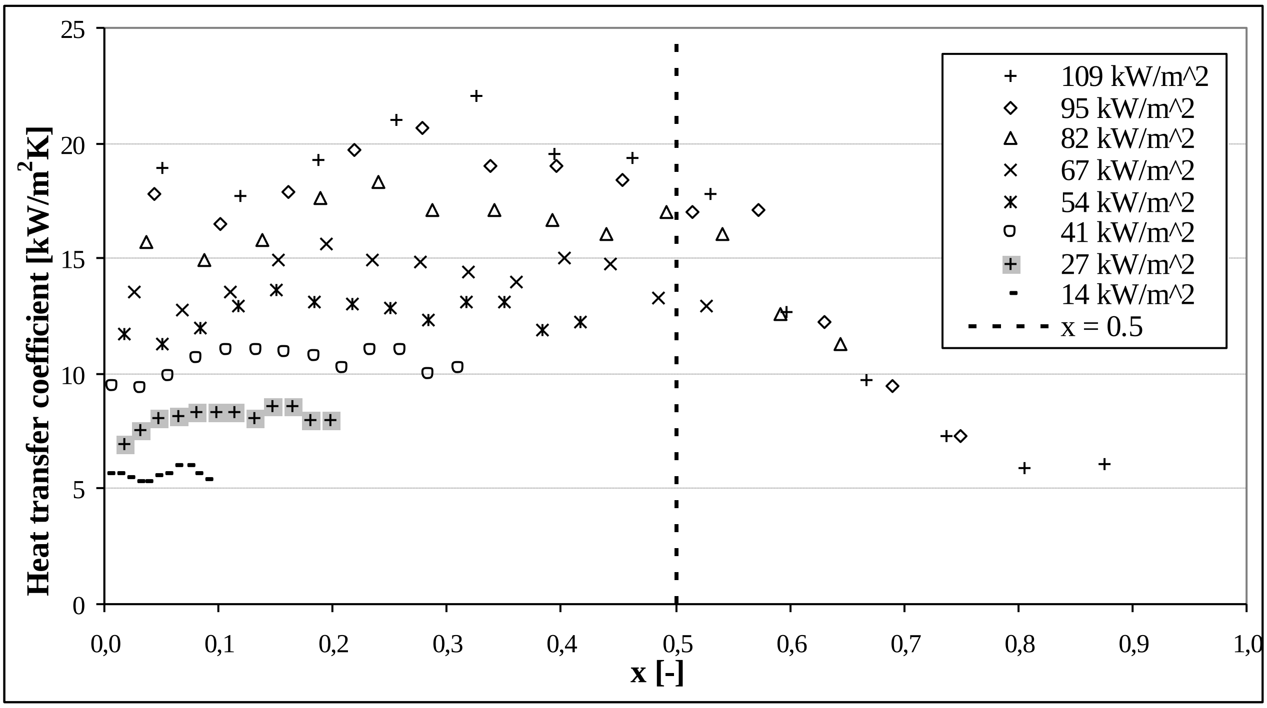

Figure 46 Local heat transfer coefficient as function of vapor quality for R-134a with different heat fluxes; G= 300 kgm^{-2}s^{-1}, p=8bar, d$_h$= 4.26 mm, **Eo=28.1**

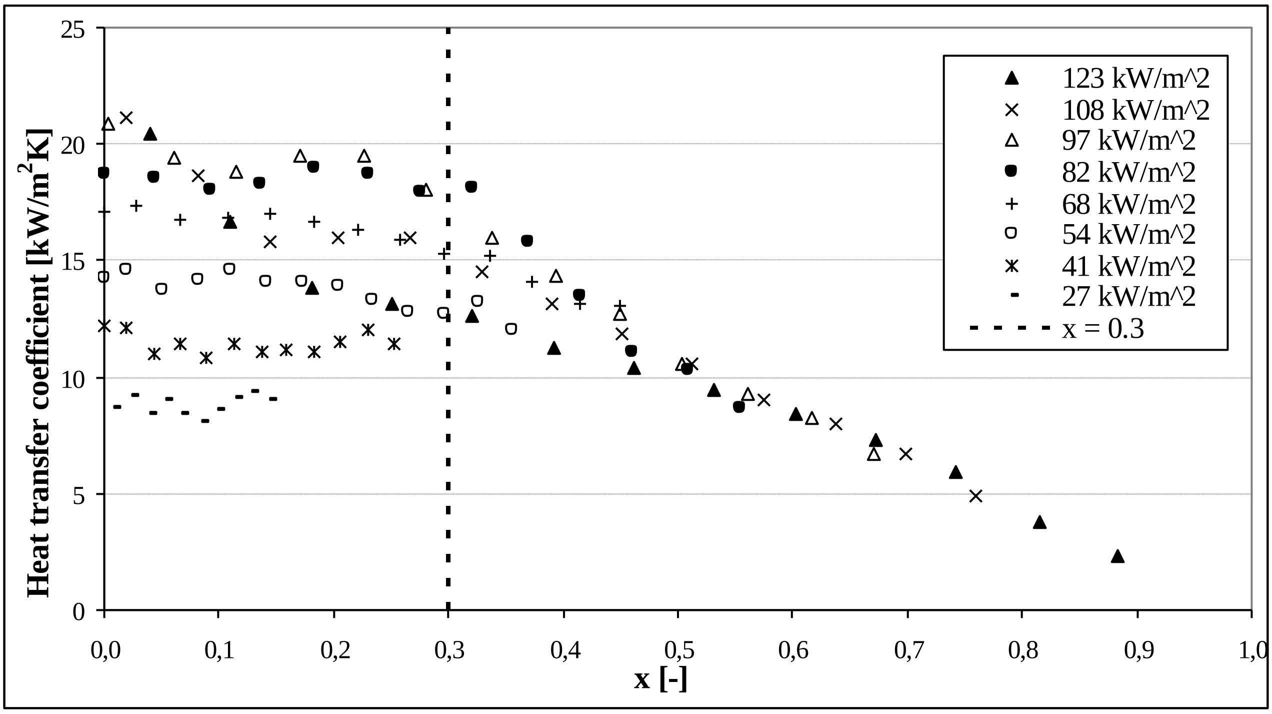

Figure 47 Local heat transfer coefficient as function of vapor quality for R-134a with different heat fluxes; G= 300 kgm^{-2}s^{-1}, q=39 kWm^{-2} , p=8bar, d$_h$= 2.01 mm. **Eo=6.26.**

Shiferaw et al. [60] presented this behaviour for h:

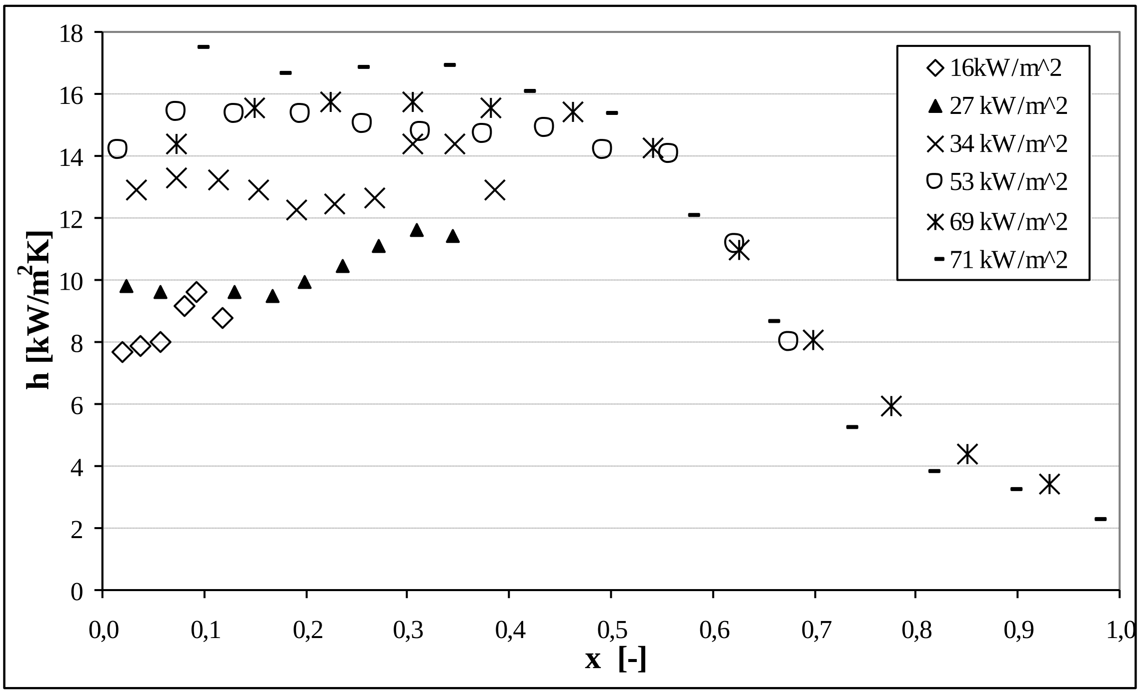

Figure 48 Local heat transfer coefficient as a function of x for R-134a with different heat fluxes; d_h=1.1mm, G = 200 kg/m2 s, P = 8 bar at different heat flux [60]. **Eo=1.87**

An accurate flow boiling heat transfer data is presented by Ong et al.[63] :

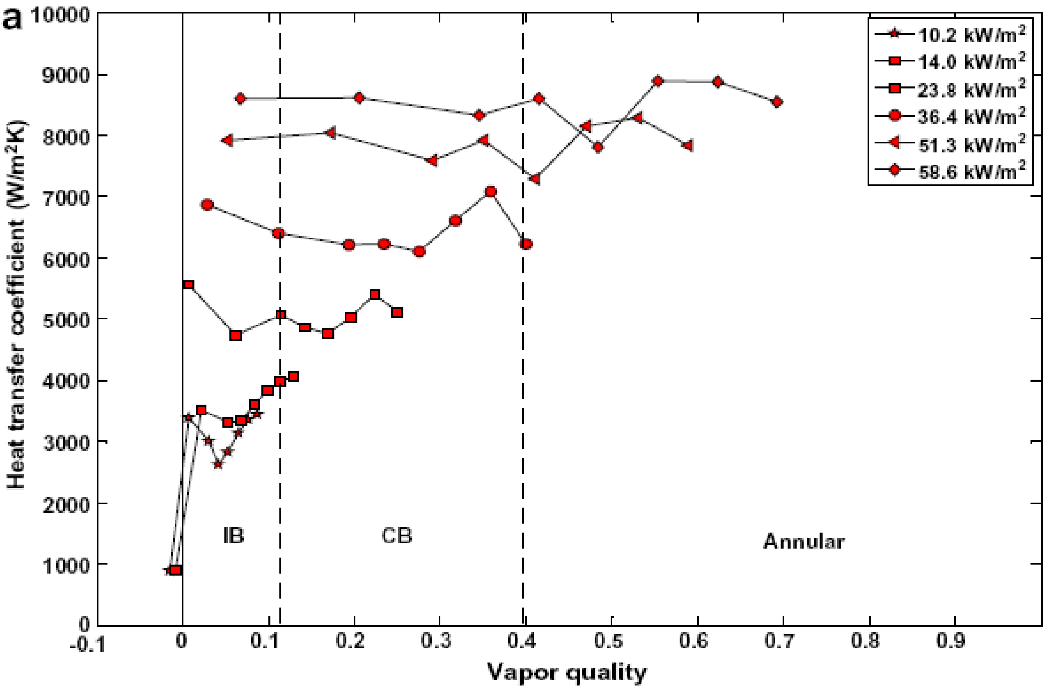

Figure 49 Heat transfer coefficients for R134a at Tsat = 29 °C for G = 300 kg/m^{2}s in a 1.030 mm [63] The decreasing heat transfer trend in the isolated bubble regime seems to be due to the transition from bubbly flow to elongated bubble flow at very small x. **Eo=1.59**

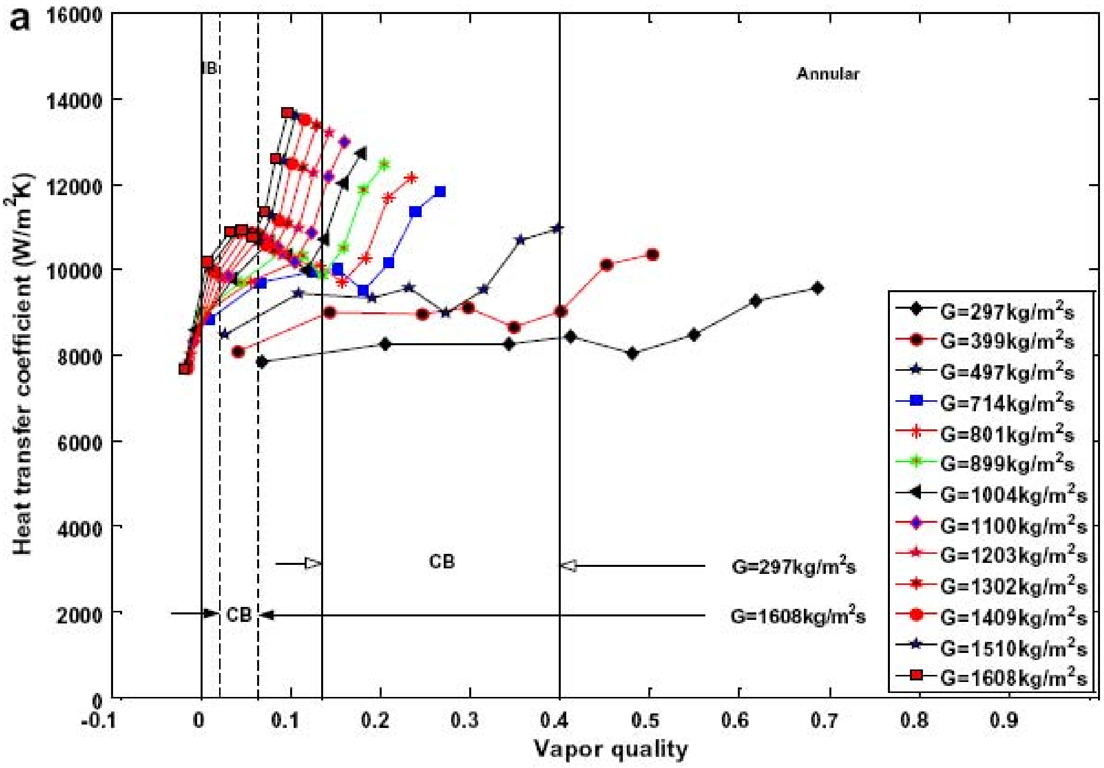

Figure 50 Effect of mass flux for R134a at Tsat = 29 °C with ΔTsub = 4 K in a 1.030 mm tube [63]. **Eo=1.59**

Lee et al. [39] proposed a new three-range two-phase heat transfer coefficient correlation, one for each quality region (see table 2); this correlation, that incorporates the effects of Bl and We_{LO} for the medium quality range, shows good predictive capability for R134a and water.

Agostini and Thome [51] categorized the trends in local flow boiling heat transfer coefficient based on a review of 13 studies; the heat transfer trends versus vapor quality are represented in Figure 51.

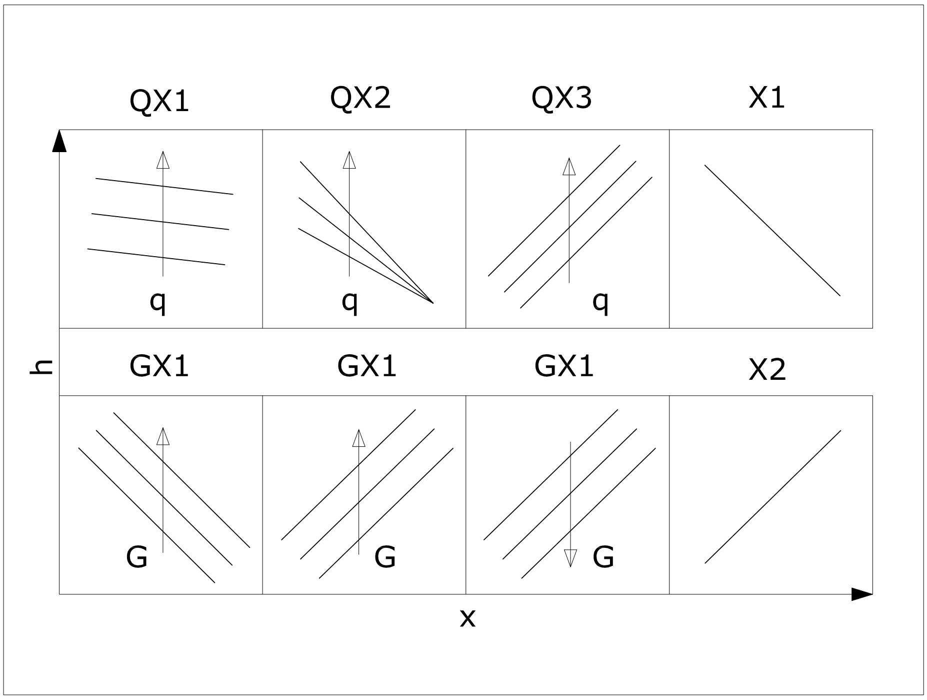

Figure 51 Heat transfer coefficient versus vapor quality documented by Agostini and Thome [51]

Here the boiling trend is identified by the different variables whose heat transfer depens on and the number refers to alternative behaviors observed with these variables. For example QX1 means that the heat transfer coefficient depends on the heat flux and vapor quality and present the behaviour named 1 among the threee observed with these variables. Agostini and Thome found that the behaviours are QX1 and X1 for the most part of the trends examined. Their conclusions can be summarized:

- for x <0.5 h increases with q" and decreases, or is relatively constant, with respect to x;

- for x>0.5 h decreases sharply with x and it does not depend on q'' or G;
- an increasing in q'' tends to increase h; this is not more true at high x;
- the effect of G varies from no effect, an increasing effect or a decreasing effect.

Referring to Figure 51, Thome asserts [58] that the three-zone model [26] responds to the effects of q'', Tsat and G and it responds to some of these trends by the onset of dryout of the liquid film (going from a two-zone to a three-zone model at that point). The model cannot explain such contrasting trends and, partially following Thome [58], additional phenomena, like channel geometry and instability effects must come into play in microchannel flow boiling.

4.3.2 The heat transfer coefficient versus superheat ΔT

Bao et al. [40] summarizes the experimental data for R-11 and R-123 inside a copper tube with a diameter of 1.95 mm for tests over a wide range of conditions. The heat transfer coefficient at each heating section is determined from the following equation:

$$h = \frac{q''}{T_W - T_F}$$

Figure 52 and Figure 53 show the heat transfer coefficient as a function of $1/(T_W - T_F)$ for R-11 for two different values of the averge applied heat flux, 55 kW/m^2 and 105 kW/m^2 [40]. From the linear best fit of Figure 52 the value of the heat flux is 58.587 kW/m^2 (R^2=0.986) and this agrees with the experimental average heat flux value.

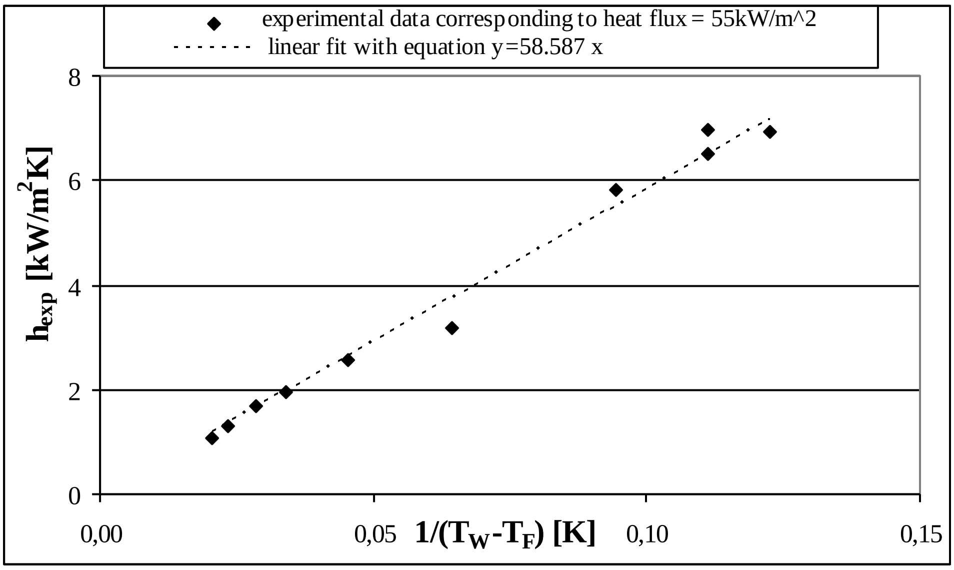

Figure 52 Plot of experimental heat transfer coefficient as function of $1/(T_W-T_F)$ for R11, with G = 446 $kgm^{-2}s^{-1}$ and inlet pressure = 463 kPa [40]. **Eo=4.37**

From the linear best fit of Figure 53, the value of the heat flux is 101.94 kW/m^2 (R^2=0.995) and this agrees with the experimental average heat flux value.

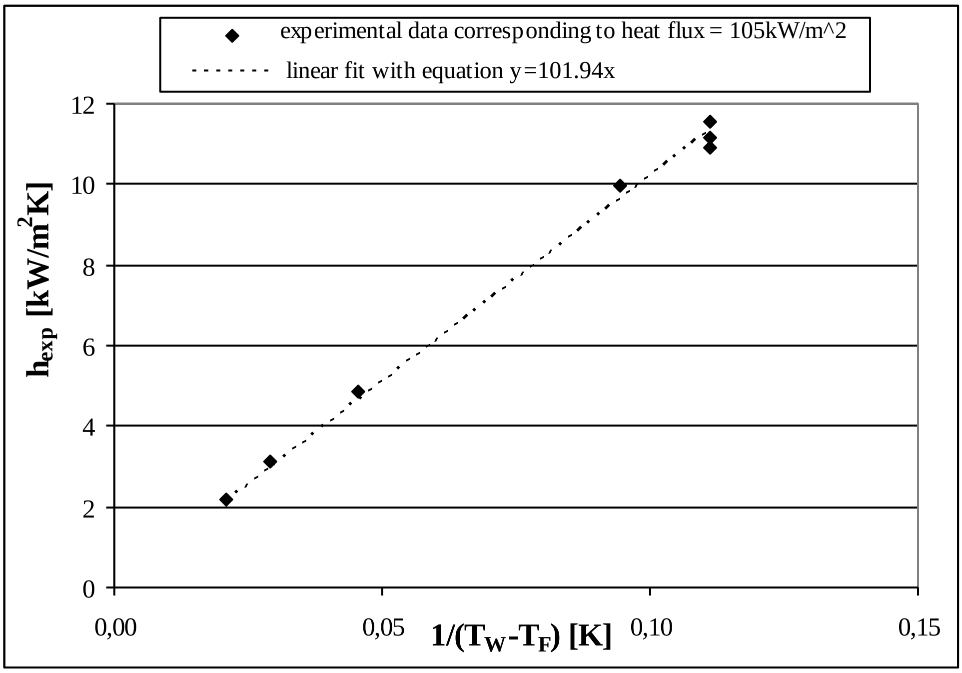

Figure 53 Plot of experimental heat transfer coefficient as function of 1/(T_W-T_F) for R11, with G = 446 kgm^{-2}s^{-1} and inlet pressure = 463 kPa [40]. **Eo=4.37**

Figure 54 shows the heat transfer coefficient as a function of 1/(T_W–T_F) for R-123 for an averge applied heat flux equal to 85 kW/m^2 [40]. From the linear best fit of Figure 54 the value of the heat flux is 92.81 kW/m^2 (R^2=0.995) and this agrees with the experimental average heat flux value.

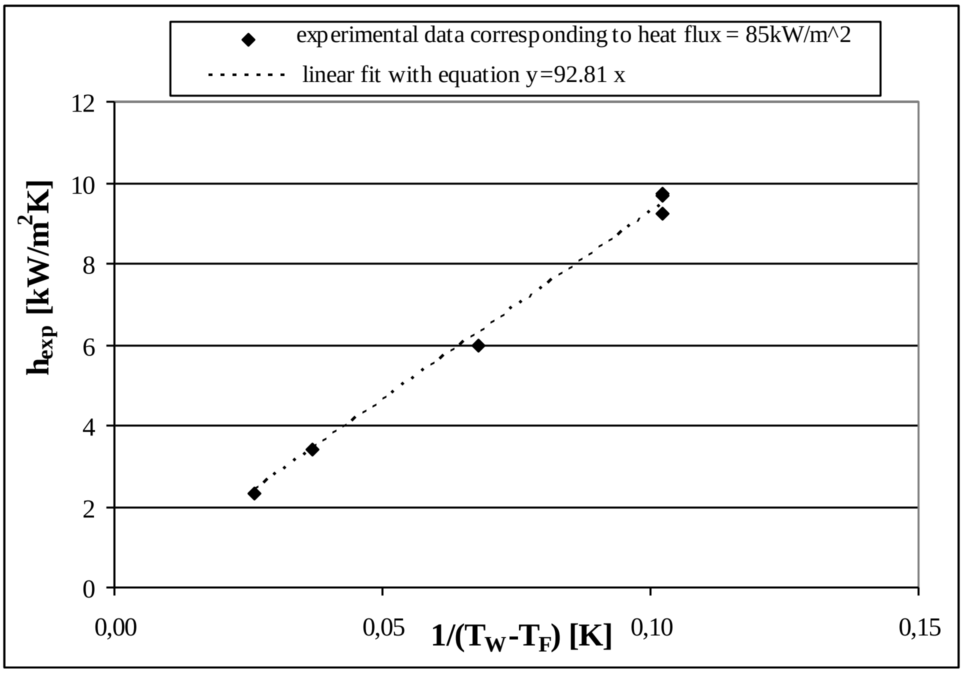

Figure 54 Plot of experimental heat transfer coefficient as function of 1/(T_W-T_F) for R123, with G = 335 kgm^{-2}s^{-1} and inlet pressure = 360 kPa [40]. **Eo=4.8**

The authors considered only the experimental data of Bao et al. [40] because it was not possible to consider other experimental works due to the lack of exact informations about the temperatures of the heated wall and the fluid. In literature, in fact, it is usually possibile to find only h as function of x and there are not experimental values of wall and fluid temperatures.

4.4 FLOW PATTERNS

An important aspect of two–phase flow patterns in microchannels is how to identify them, qualitatively and /or quantitatively. The difficulty of identifying flow regimes and their transitions visually comes from the difficulties both in obtaining good high-speed images and in the interpretation of the flow (subjectivity and pattern definition depending on the author), and also in choosing the channel size that determines either macro or microscale or the transition between them. In Kandlikar’s opinion in 2002, the literature on flow patterns in microchannels is insufficient to draw any conclusions but it is possible to underline that the effect of surface tension is quite significant causing the liquid to form small uniformly spaced slugs that fill the tube, sometimes forming liquid rings. In his review in 2006, Thome [58] asserts that at very low G the two-phase flow in microchannels approaches capillary flow as a natural limit, where all the liquid flow is trapped between pair of menisci with dry wall vapor flow in between; no stratified flow is observed in microchannels due to the predominance of surface tension over gravity forces so that the tube orientation has negligible influence on the flow patterns.

The three-zone heat transfer model proposed by Thome et al. [26] illustrates the strong dependency of heat transfer on the bubble frequency, the length of the bubbles and liquid slugs and the liquid film thickness. For these reasons, it is opportune to apply an optical measurement technique to quantitatively characterize flow pattern transitions and to measure the frequency, velocity and length of vapor bubbles in microchannels, in particular at the exit of microevaporators in which the flows are formed. So the better approach is to use quantitative means to identify flow patterns, for which various techniques are available; one is the two laser/two diode optical technique developed by Revellin et al. [50] for microchannels.

It is important to underline that the bubble size and the bubble behavior is influenced also by subcooling. Kandlikar et al. [*73*] concluded that the bubble growth rate strongly depended upon subcooling. Low pressure subcooled flow boiling inside a vertical concentric annulus (d_h =13 mm) examined by Zeitoun et al. [*74*] showed that the mean size and lift duration of the bubbles increased at decreasing liquid subcooling. Chang et al. [*75*] examined the behavior of near-wall bubbles in subcooled flow boiling of water in a vertical one-side heated rectangular channel (d_h = 4.44 mm) and described the coalescence of the bubbles. Yin et al. [*76*] studied the bubble generation for R-134a in a horizontal annular duct (d_h = 10.31 mm); they showed that the liquid subcooling exhibited a significant effect on the bubble size and that raising the refrigerant mass flux and subcooling suppressed the bubble generation. In 2009 Chen et al. [*77*] explore the heat transfer and bubble behavior in subcooled boiling flow of R-407C in a horizontal narrow annular duct. They examine in particular the bubble characteristics such as the mean bubble departure diameter and frequency from the heating surface by mean of flow visualization in order to improve the understanding of the subcooled flow boiling processes in a narrow channel. In [77] is underlined that higher wall superheat and higher imposed heat flux are needed to initiate the boiling for a higher subcooling and, recording the bubble motion at a given ΔT_{sub}, it emerges that the bubbles are larger at a lower liquid subcooling. This is due to the weaker vapor condensation and to the more bubble coalescence at a lower ΔT_{sub}. Increasing the inlet subcooling results in a reduction of the bubble departure frequency and of the number of active nucleation sites.

Recently Zhuan et al. [78] analyzed the process of bubble growth, condensation, and collapse in subcooled boiling in the micro-channel trough simulation. The degree of subcooling influences bubble growth and collapse; an annular flow seldom occurs in subcooled boiling for wide range of mass and heat fluxes and this is a big difference with the saturated boiling where slug and annular flows usually appear in the microchannel. In subcooled boiling, the bubble flow occurs with higher heat flux compared with saturated boiling at the same mass flux and, in accordance with [79], the ONB heat flux increases as the subcooling increases.

Table 4 summarizes the observation on flow patterns in microchannels.

Author	Observations on flow patterns
Chen et al. [16] Figure 55, Figure 56	Dispersed bubble, bubbly, slug, churn and annular flow. Occasionally mist flow was observed in the bigger tubes at very high vapor velocity while confined bubble flow19 was found in smaller tubes at lower vapor and liquid velocity. It was only observed in the 1.10 mm tube at all experimental pressures and in the 2.01 mm tube only at 6.0 bar. This indicates that surface tension became the dominant force in the smaller tubes at the lower fluid velocities and this agree with the confinement criterion by Kew and Cornwell [28] for which the confinement effect should be observed at diameter of tube between 1.7 and 1.4 mm at 6-14 bar. With the increase of fluid velocities, inertial force and friction gradually replace the importance of surface tension.
Harirchian and Garimella [32,*80*] Figure 57	Five flow regimes – bubbly, slug, churn, wispy-annular and annular flow- were identified. Vapor bubbles are confined within the channel cross-section in slug flow and in confined annular flow.
Cornwell and Kew [81], Lin et al. [11, 82]	Three flow patterns are commonly encountered during flow boiling in minichannels/microchannels: isolated bubble, confined bubble or plug/slug20, and annular flow.

---

[19] It is similar to slug flow but with elongated spherical top and bottom bubbles.

[20] slug flow, is found at low and intermediate vapor qualities in micro-channel systems.

Ong and Thome [63]	Isolated bubble, coalescing bubble and annular flow.
Revellin and Thome [35] Figure 59	The microscale flow patterns were first classify in the ‘classical’ manner as follows: bubbly flow, bubbly/slug flow, slug flow, slug/semi-annular flow, semi-annular flow, wavy annular flow and smooth annular flow. Then, rather than limiting the observations into the traditional flow regimes and an adiabatic map, a novel diabatic map (see 4.5) classifies flows into three types: isolated bubble, coalescing bubble and annular flow zones.
Revellin et al. [50] and [83]	Bubbly flow, slug flow, semi-annular flow and annular flow. It is evidenced that the thin film surrounding the bubbles becomes more uniform as the diameter decreases and this is the evidence that buoyancy has still a role. The higher G is, the earlier annular flow is encountered while bubbly flow tends to disappear at high G because small bubbles quickly coalesce to form elongated ones.
Ribatski et al [29]	Bubbly flow is seldom observed due to the fact that its lifespan is very short as bubbles coalesce or grow to the channel size very quickly
Shiferaw et al. [60] Figure 58	At low q" confined bubble flow and then, increasing q", elongated bubble, slug, wavy annular, annular flow respectively.
Zhang et al. [84]	No bubbly or plug flow, mostly annular flow with a very thin layer of liquid.

Table 4 Summary of the observations on flow patterns in mini-microchannels recently presented in literature. Some of these flow patterns are presented in the following figures.

In Figure 55, Figure 56, Figure 58, Figure 59 there are some flow patterns observed for R134a during the experiments [16], [35], [60].

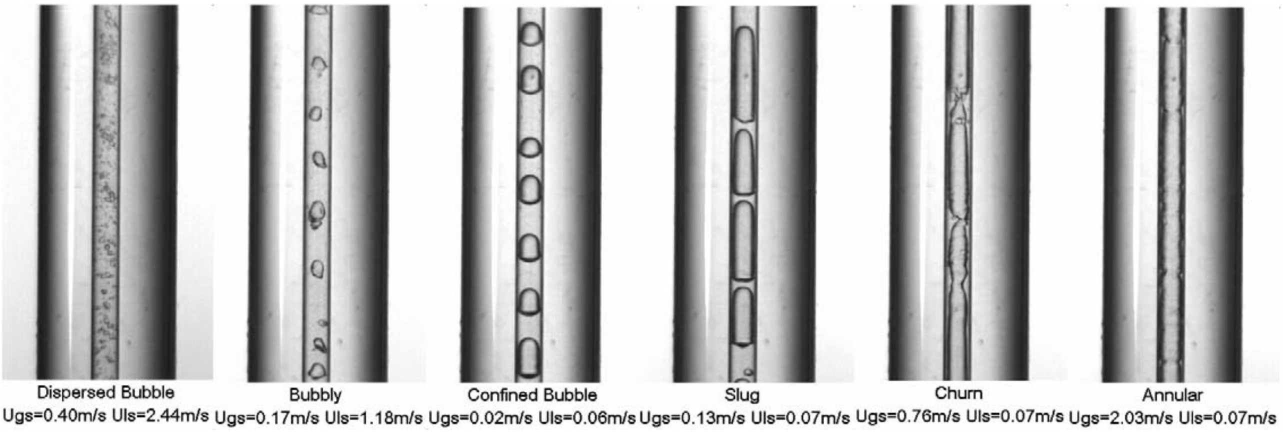

Figure 55 Flow patterns observed for R-134a in the 1.1 mm internal diameter tube at 10 bar [16] **Eo=2.1**

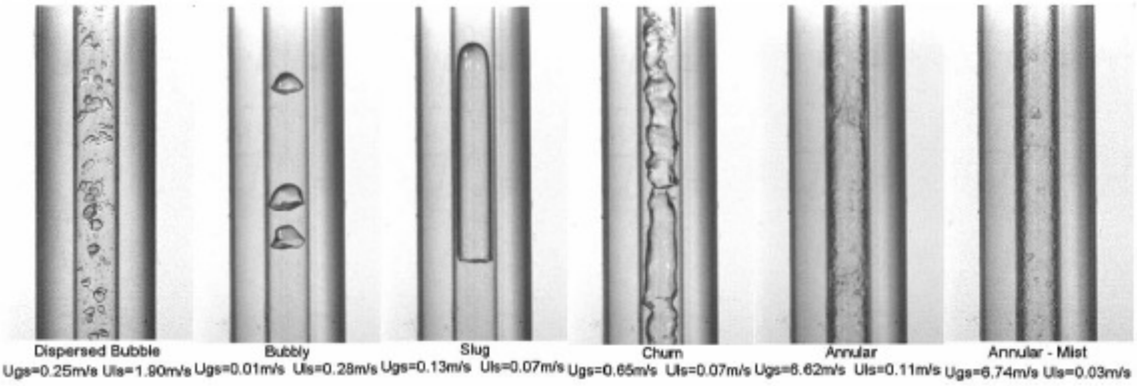

Figure 56 Flow patterns observed for R-134a in the 2.01 mm internal diameter tube at 10 bar[16]. **Eo=7.03**

Figure 57 present the summary of boiling flow patterns of Harirchian and Garimella [32] for different microchannel sizes and mass fluxes. Five flow patterns are observed: bubbly (B), slug (S), churn (C) wispy-annular (W) and annular (A); sometimes there is alternating bubbly/slug flow (B/S), alternating churn/ wispy-annular flow (C/W) or alternating churn/annular flow (C/A). In Figure 57 the empty “rectangles” represents single-phase flow.

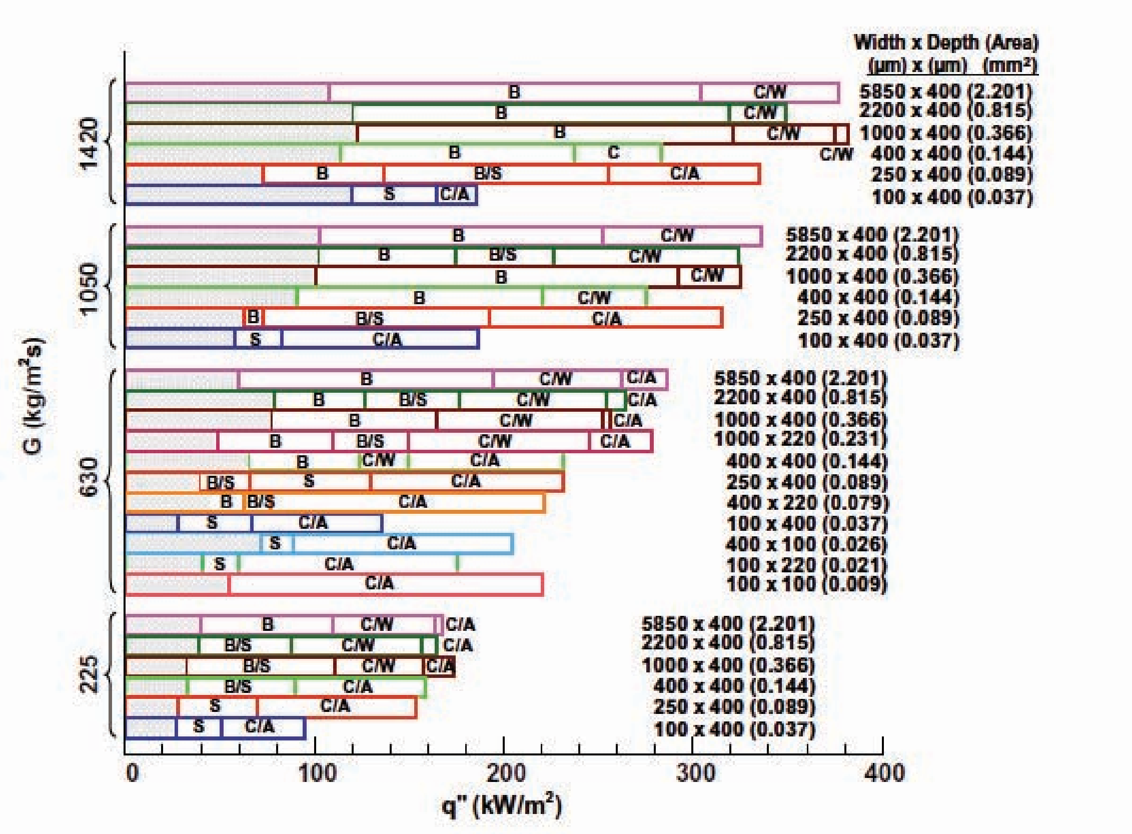

Figure 57 Boiling flow patterns in microchannels [32]

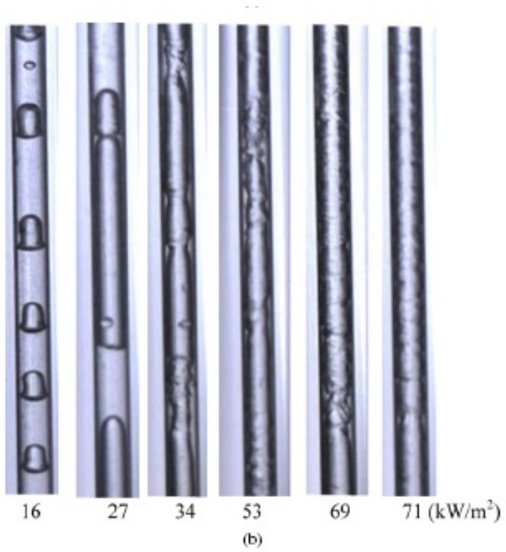

Figure 58 Typical patterns for R134a in 1.1 mm internal diameter tube, G=200 kg/m^{2}s, p= 8 bar [60]. **Eo=1.87**

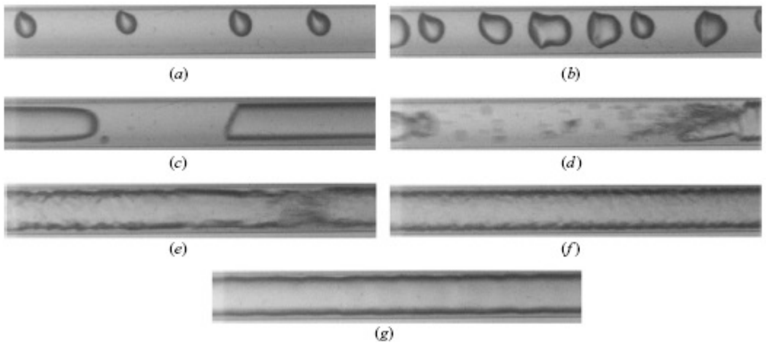

Figure 59 Flow observations for R-134a, D = 0.5 mm, L = 70.70 mm, G = 500 kg m–^{2} s–^{1}, T_{sat} = 30 ˚C and ΔT_{sub} = 3 ◦C, at exit of heater taken with a high definition digital video camera. (a) Bubbly flow at x = 2%; (b) bubbly/slug flow at x = 4%; (c) slug flow at x = 11%; (d) slug/semi-annular flow at x = 19%; (e) semi-annular flow at x = 40%; (f) wavy annular flow at x = 82%; (g) smooth annular flow at x = 82% [35]. **Eo=0.39**

4.5 FLOW PATTERN MAPS

To better predict heat transfer coefficients it is desirable to develop a flow pattern map for predicting the flow regimes of two-phase flow in microchannels; flow pattern maps are used to determine the flow patterns that exist underwent different operating conditions and to predict the transition from one type of two- phase flow pattern to another type. Regarding the flow pattern transition prediction methods, there is the need of incorporating the properties of the gas and liquid phases in order to generalize the map to work for other than the original fluid. In literature there are some proposed flow pattern maps based on air-water flows but they are not listed here because in this review we are interested only in single substance two-phase flow.

In 2006 Chen et al. [16] underlined that none of the existing flow pattern map were able to predict their observations; they identified the Weber number as the most useful parameter to predict the transition boundaries that include the effect of diameter. In 2007 Revellin and Thome [83] showed that the flow pattern transition depend on the coalescence rates and that the observed transitions did not compare well to the existing macroscale flow map for refrigerants nor to a microscale map for air–water flows. So they proposed [35] a new type of flow pattern map for evaporating flow in microchannels.The new type of diabatic map [35], presented in Figure 60, classifies flows as follows:

a) the isolated bubble (IB) regime, where the bubble generation rate is much larger than the bubble coalescence rate and includes both bubbly and slug flows;

b) the coalescing bubble regime (CB), where the bubble coalescence rate is much larger than the bubble generation rate and exists up to the end of the coalescence process;

c) the annular regime (A), whose extent is limited by x at the onset of CHF.

d) Dryout regime (PD): begins at x corresponding to the onset of CHF and PD refers to the post-dryout region, after passing through CHF at the critical vapour quality.

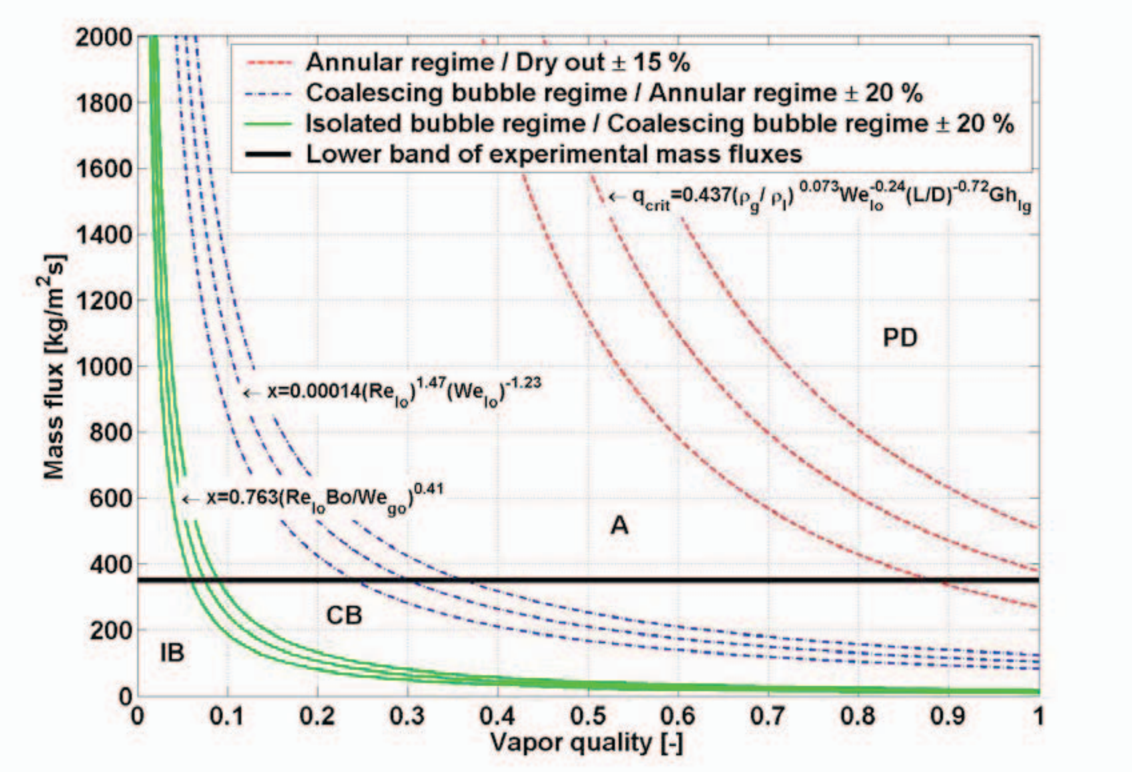

Figure 60 Diabatic coalescing bubble map for evaporating flow in circular uniformly heated microchannels: R-134a, D = 0.5 mm, L = 70 mm, T_{sat} = 30 °C, q = 50 kW m^{-2} and ΔT_{sub} = 0 °C [35]. Transition boundaries, center curve of each group, are shown with their error bandwidth. **Eo=0.39**

The lower end of the transition lines below the horizontal black line represents an extrapolation below the lowest G tested, where two-phase flow instabilities occur. Using the laser/diode measurement technique described in [50] the bubble frequency was detected and it was found that, at a fixed G, it increases with q" and x until it reaches a peak; after that the frequency decreases, first very sharply and then less sharply, to a bubble frequency of zero. The first sharp fall off is due to the coalescence of all the smaller bubbles into long bubbles and the slower fall off is from the coalescence of the long bubbles into even longer and thus fewer bubbles, until the annular flow is reached. The transition prediction methods are also described in [35] and the equations for calculating x at which a transition occurs, showed in Figure 60, are evaluated for R134a properties at 30℃ in terms of Bl, Re_L, We_L, We_V. The vapour quality transition location IB/CB does not depend on the channel diameter but is a function of q"; on the other end, the CB/A transition, that is the vapour quality at which the bubble frequency reaches zero, i.e. it is the end of the presence of liquid slugs and distinct vapour bubbles, it is not influenced by q".

The diabatic flow pattern map described above, has been advanced by a mechanistic approach proposed by Revellin et al. [85] using an elongated bubble velocity model proposed by Agostini et al. [86]. This elongated bubble velocity model predicts that elongated bubbles travel faster as their lengths increase and predicts the bubble frequency and the mean bubble length as a function of the vapor quality in a micro-evaporator. This model is a step towards a theoretically based diabatic flow pattern map that yields bubble frequencies and bubble lengths.

The experimental flow pattern observations by Ong and Thome in 2009 [63] for R134a in a 1.030 mm channel, show good agreement with the extrapolation of the flow pattern map by Revellin and Thome [35]. On the other hand, the CB/Annular transition did not work as well for the fluids R236fa and R245fa. So, based on this new larger database for these three fluids, Ong and Thome modified the IB/CB transition correlation and also the CB/Annular transition expression to account for the effects of reduced pressure of these two refrigerants to this larger channel. The new expressions compare well with the new observations for R134a, R236fa and R245fa for channel diameters from 0.509 to 1.030 mm, for G above 200 kg/m^{2}s and reduced pressures from 1.842 to 7.926 bar. The new proposed flow transition lines with error boundaries for all the three fluids are shown in Figure 61, Figure 62 and Figure 63.

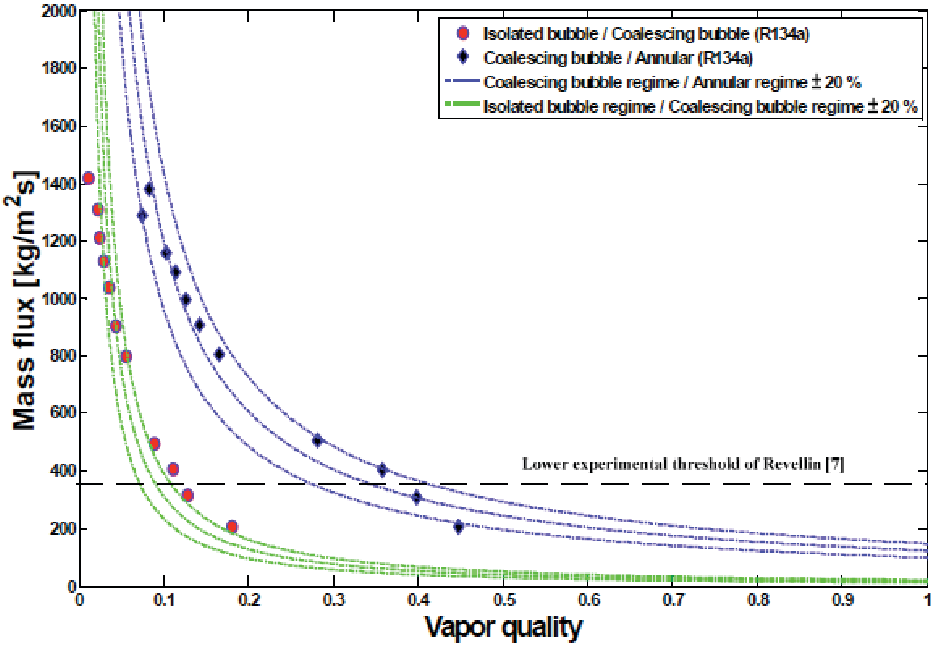

Figure 61 Comparison of experimental flow pattern transition lines for R134 with the new proposed flow transition lines for the 1.030 mm channel at T_{sat}=31°C [63] **Eo=1.63**

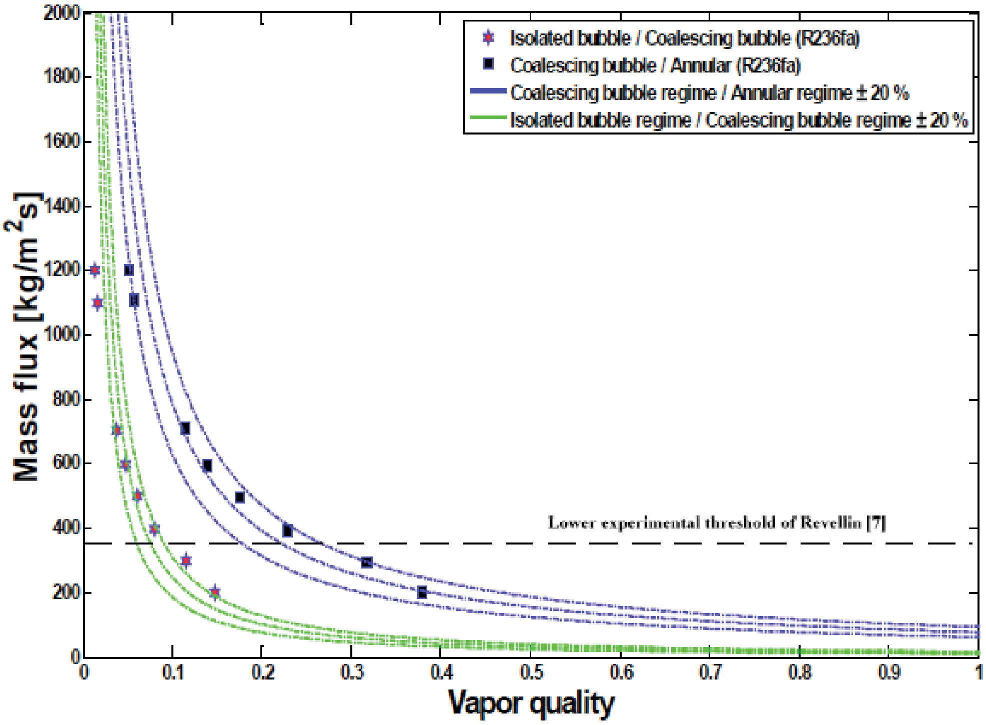

Figure 62 Comparison of experimental flow pattern transition lines for R236fa with the new proposed flow transition lines for the 1.030 mm channel at T_{sat}=31°C [63] **Eo=1.46**

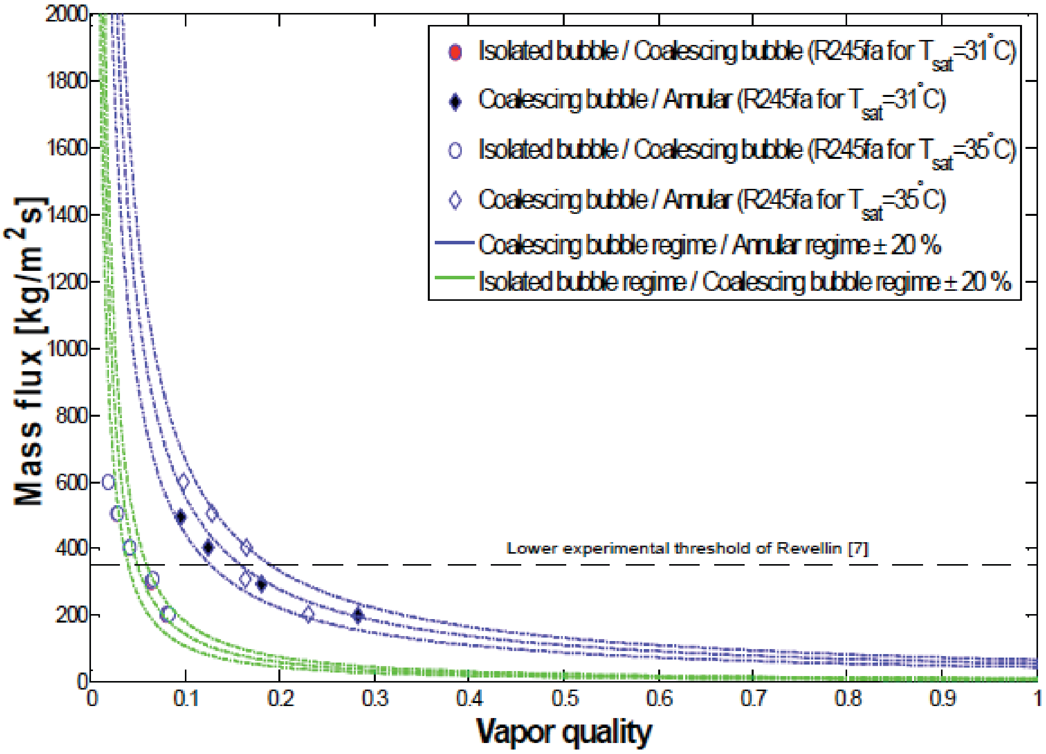

Figure 63 Comparison of experimental flow pattern transition lines for R245fa with the new proposed flow transition lines for the 1.030 mm channel at T_{sat}=31°C [63] **Eo=1.03**

In 2010 Harirchian and Garimella [32] proposed a comprehensive flow regime map for microchannel flow boiling with quantitative transition criteria for flow pattern transitions in order to determine the flow pattern that exists under a given set of conditions. The map was developed for boiling of FC-77 for a wide range of experimental parameters and channel dimensions; the map uses non-dimensional parameters of $Bl \times Re_{LO}$ and $Bo^{0.5} \times Re_{LO}$, the convective confinement number introduced in section 3.1, as the coordinates and it presented four regions, each associated to a flow regime: slug, confined annular, bubbly and alternating churn/annular/wispy-annular flow. A modified version of this flow regime map has been presented in 2012 [52] to include the effect of the heated length of the microchannels on two-phase flow development; this new map has the phase change number, N_{pch}[21], as the y-axis, differently from Bl x Re_{LO} that was the y-axis of the previous version [32]. Figure 64[22] presents this modified version of the map, which enables the determination of the distance from the inlet of the microchannels where different flow transitions occur.

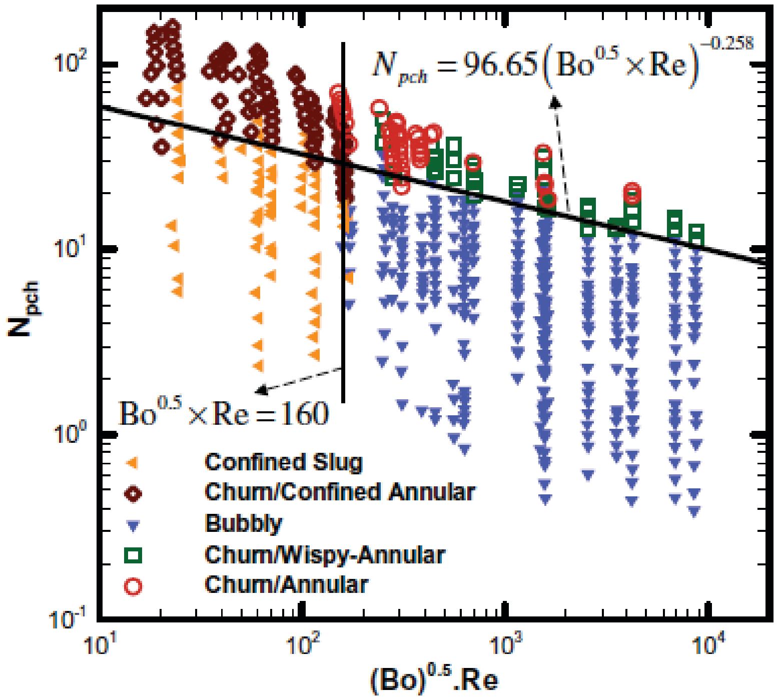

Figure 64 Flow regime map using the phase change number [52]

---

[21] $$N_{pch} = Bl \frac{L_H}{D_{hH}} \frac{\rho_L - \rho_V}{\rho_V}$$ where D_{hH} = cross sectional area of a microchannel / (microchannel width +2·microchannel depth).

[22] In figure Re indicate the Reynolds number calculated using the liquid phase mass flux and so it corresponds to Re_{LO} defined in nomenclature.

Chapter 5

Flow boiling in microgravity

Boiling heat transfer under microgravity conditions is to be widely applied to the high performance heat exchange processes in space and the experimental results for microgravity boiling are helpful for understanding terrestrial boiling phenomena because the gravitational force, which appears to be one of the important parameters dominating the bubble motion and the heat transfer, is markedly decreased. Furthermore, the presence of gravity can mask effects that are present, but are comparatively small. Both low gravity and earth laboratory researchers interact in order to foster collaborative work on the physics of two- phase systems, using reduced gravity as a specific tool to facilitate access to interfacial phenomena. The knowledge about the fundamentals of flow boiling in microgravity is still quite limited. The availability of flight opportunities is scarce and so the experimental activity in this area is still quite fragmented, and, consequently, coherence in existing data is somewhat missing. As regards the critical heat flux data, there is almost no existing fundamental work [18].

Celata and Zummo [21] concluded that a systematic study of flow boiling heat transfer is necessary in order to better establish the flow boiling heat transfer knowledge in microgravity, because the available results on heat transfer are contradictory, spanning from increase to decrease with respect to terrestrial gravity and include no effect of gravity level. It is also fundamentally important to determine the flow condition threshold for which microgravity does not affect flow boiling heat transfer, i.e. the threshold beyond which inertial effects are dominant over buoyancy.

5.1 FLOW PATTERN FEATURES

The effect of gravity levels on heat transfer strongly depends on the flow patterns and, therefore their knowledge has a fundamental role.

Author, test fluid and diameter of test section	**Observations on the flow patterns gravity effects**
Ohta [19] Freon 113 8 mm	For the subcooled condition: at 1*g* the bubbly flow in the inlet region changes to the alternate froth and annular flow in the exit region while at μ*g*, void fraction markedly increases even in the inlet region due to the decrease in bubble velocity, which in turn promotes the transition to annular flow at lower quality. For moderate x: the annular flow is observed along the entire tube length for 1g and μ*g* but in this case the turbulence in the annular liquid film is reduced. At high x, the flow pattern is almost independent of gravity.
Celata et al. FC-72 4 and 6 mm [20,21, 87] Figure 65 and Figure 66	The observed flow patterns at low gravity are bubbly, plug and a disordered intermittent flow. In bubbly flow, for low G and low q", gravity level affects both bubble shape and size. For higher G differences in bubble size and flow pattern at the two gravity levels tend to disappear. With increasing q", the flow patterns become intermittent

	with elongated bubbles for both gravity conditions. Further increasing in q''cause Taylor bubbles[23] to become longer and liquid slug to become shorter. Bubbly-intermittent flow transition at μ*g* is anticipated with respect to the transition at 1g.
Luciani et al. [6] Figure 69	Very big differences in bubble size and flow patterns between 1g and μ*g*: classical bubbly flow structure at 1g while at μ*g* there is an evolution of bubble structure from slug to churn flow.

Table 5 Summary of the observations on the flow patterns gravity effects recently presented in literature.

---

[23] Taylor bubbles are the bullet-shaped vapor bubbles with a diameter similar to the channel diameter that characterize plug flow. These bubbles are elongated in the direction of the channel axis and the length can vary from one diameter up to several channel diameters.

The results obtained with the 4 mm for 1g and μg in [20] are depicted in Figure 65.

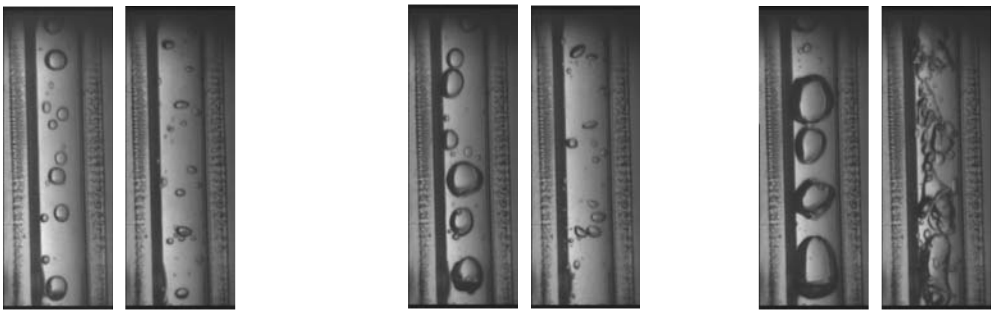

(a) q''=17520W/m^2, xout=-0.081 (b) q''=19326W/m^2, xout=-0.033 (c) q''=20220W/m^2, xout=-0.004

(d) q''=22222W/m^2, xout=0.039 (e) q''=23800W/m^2, xout=0.06 (f) q''=26488W/m^2, xout=0.11

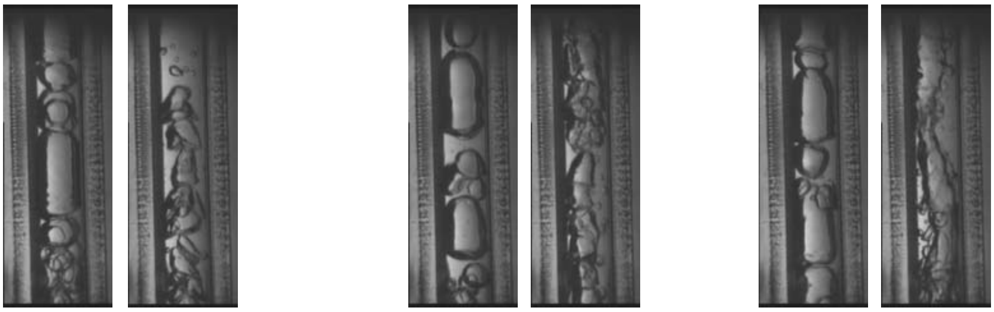

Figure 65 Flow patterns at microgravity conditions (left) and at terrestrial gravity (right) for d=4 mm, G= 93kg/m^{2}s, p=1.78 bar [20]. **Eo=0.35** at μg and **Eo=35.5** at terrestrial gravity.

In bubbly flow, Figure 65 a) and b), the spherical shape at 0 g, agree with the fact that when the interfacial forces are predominant on inertial and buoyancy forces, the surface of the bubble is minimized and the shape tends to be spherical. Celata et al. [20] undelined that since for low G inertial forces can be neglected, the Eo number, described in 2.1.1, is usefull to evaluate the influence of interfacial forces on buoyancy. In microgravity condition Eo number is small and therefore the bubble surface is minimized and this results in a spherical shape. Celata et al. [20] attributed the larger diameter of bubbles at 0 g situation to the detaching mechanisms that is characterized by a long growth because of the absence of buoyancy.

In the bubbly-plug flow in Figure 65 c), the elongated bubble diameter reaches the tube diameter at 0 g while at 1 g the bubble diameter is smaller. Furthermore, at 0 g the bubbles are separated by liquid slugs containing few small bubbles while at terrestrial gravity the liquis slugs contain a lot of irregular bubbles. The same behaviour is observed for the intermittent flow in Figure 65 d), e) and f) where the increasing in the heat flux is accompanied by longer bubbles and shorter liquid slugs and the disorder in the vapor –liquid configuration is higher at 1 g than at 0 g, as underlined in [20].

Celata et al. [20] underlined that the effects of gravity level on flow pattern decrease with the increasing of the mass flux; in Figure 66 there are the flow patterns for 0-g and 1-g obtained for high G. The bubbly flow in Figure 66 a) and the intermittent flow in Figure 66 b) are less influenced by the gravity level if compared with the flow patterns of Figure 65.

(a) low heat flux (b) high heat flux

Figure 66 Flow patterns at microgravity conditions (left) and at terrestrial gravity (right) for d=4mm, G= 355 kg/m^{2}s, p=1.8 bar , $\Delta T_{sub,in}$=25.3 K [20]; **Eo=0.35** at μg and **Eo=35.5** at terrestrial gravity

Summarizing the flow patterns observations presented by Celata et al. in [20,21,87], bubbly flow occurs in both tube diameters, 4 and 6 mm, in the subcooled flow boiling region and in the near zero quality area for saturated flow boiling region. For increasing values of x, two types of intermittent flow are observed: plug flow for G<230 kg/m2s and a more disordered intermittent flow for higher values of G. Celata et al. underlined [20] that G=230 kg/m2s represents the boundary between an ordered flow (plug flow) and a disordered and chaotic flow and that the corresponding inlet value of Reynolds number is 1970, that is very close to the region of the transition from laminar to turbulent flow in single-phase flow.

Celata et al. analyzed flow pattern data [20] with four flow pattern maps developed for gas-liquid flow, without phase change; one was developed for normal gravity conditions [88] and three for low gravity conditions [89, 90, 91, 92]. The map of Dukler and co-workers [89,90], based on the void fraction transition criteria, shows a reasonable prediction capability with smaller tubes (d=4mm), but not in the transition from bubbly to slug flow region for the tube of 6 mm, as it is possible to see from the transition lines in Figure 67 and Figure 68. The transition from bubbly to slug flow is postulated to occur when the void fraction is equal to 0.45 and it is represented by the unbroken line in the following figures.

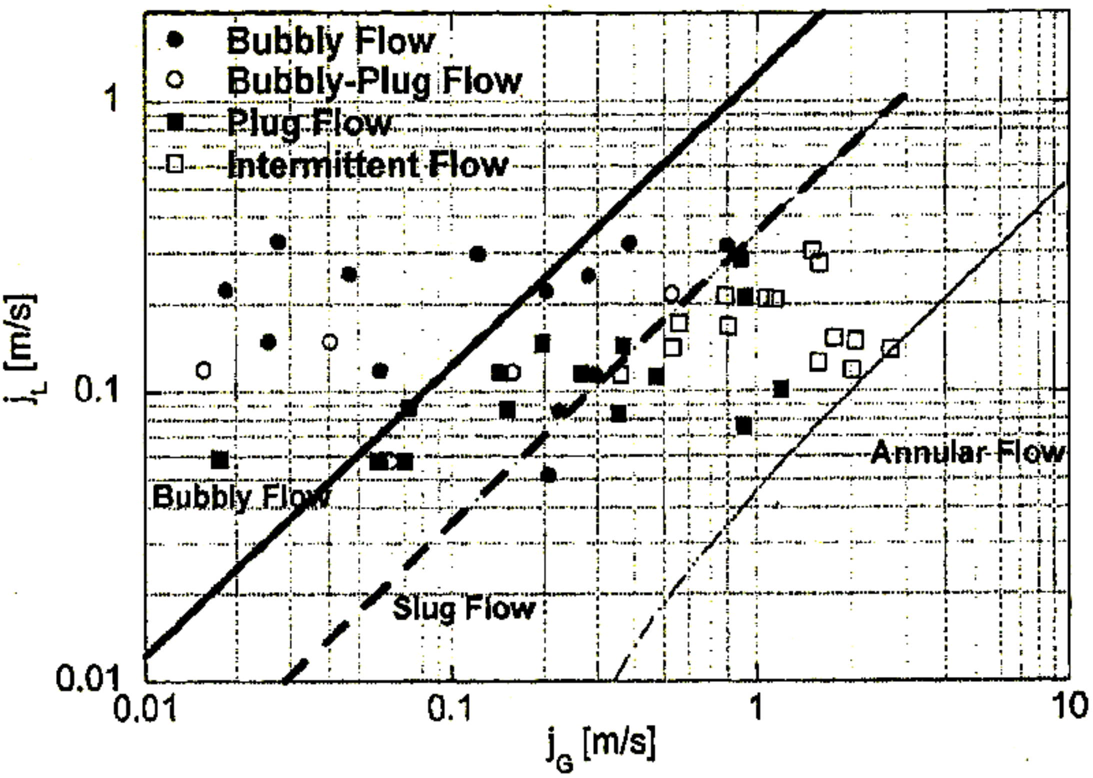

Figure 67 Flow pattern map for microgravity data for the tube of 4 mm [20] **Eo=0.35**

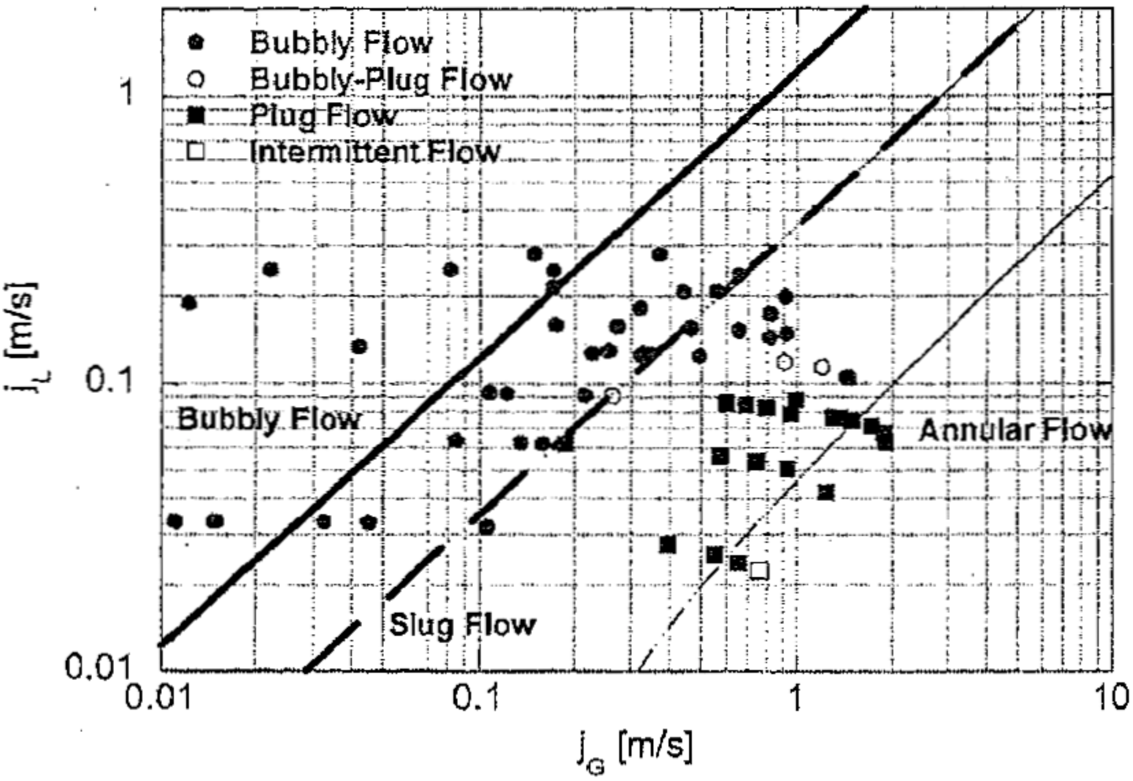

Figure 68 Flow pattern map for microgravity data for the 6 mm tube [20] **Eo=0.8**

Celata et al. [20] proposed a modified criterion for the bubbly-slug flow transition for larger tubes. They postulated that this transition occurs when the void fraction reaches the maximum value of 0.74. This modification showed in Figure 67 and Figure 68 with a dashed line, makes the flow pattern map proposed by Dukler and co-workers a good prediction tool for low gravity data flow pattern for the 6 mm tube but it does not work for the smaller tube.

In Figure 69 there are the flow patterns by Luciani et al. [6] for hypergravity and microgravity[24]; at 2-g there is a classical bubbly flow

---

[24] In this paper μg corresponds to 0.05ms^{-2} and hypergravity to 2g.

structure while at μg there is an evolution of bubble structure from slug to churn flow. The profiles are similar in hypergravity and terrestrial conditions.

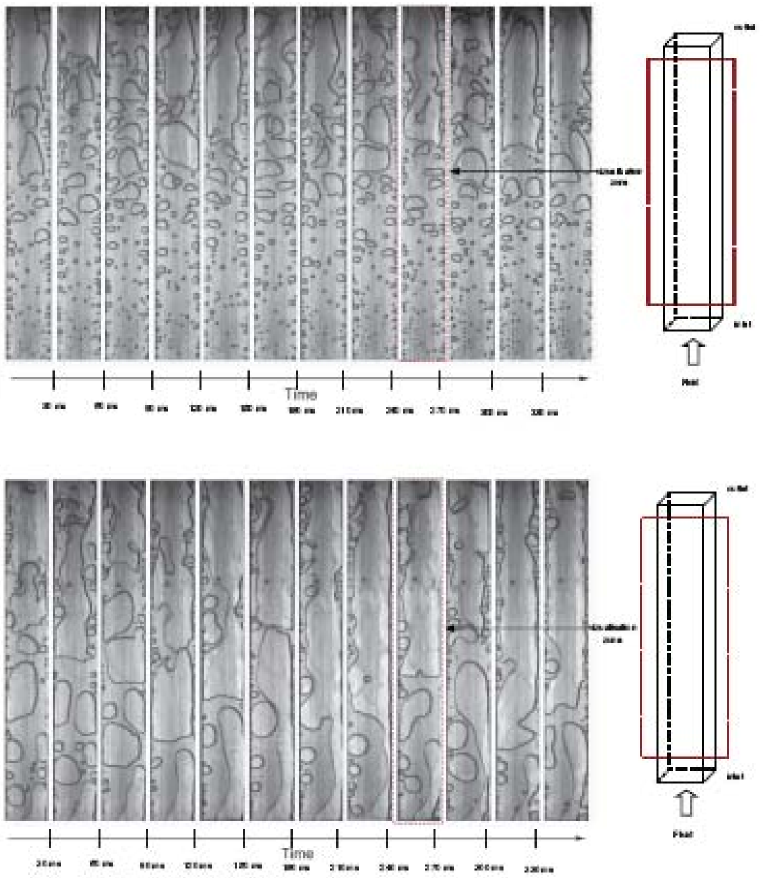

Figure 69 Conditions of hypergravity (top) and microgravity (bottom) for d_h= 0.84 mm, q'' =33 kWm^{-2}, $Q=2.6 \cdot 10^{-4}$ kgs^{-1}, Tsat= 54°C [6] **Eo=1.44** at 2-g and **$Eo=3.67 \cdot 10^{-3}$** at 0-g

Luciani et al. [6] explain these differences in bubbles size *in* terms of the capillary length l_c, introduced in 3.1. During a parabolic flight g is the only parameter that changes at a constant mass flux and heat flux rate and, passing from 1g to μg, l_c, that depends on $\frac{1}{\sqrt{g}}$, increases *by* nearly *as much as* 1400%. This may explain the different size of the bubbles of Figure 69.

5.2 HEAT TRANSFER

When the heat transfer coefficient, measured in microgravity conditions, is compared with the values obtained at terrestrial gravity, two conflicting trends are obtained. In some experiments there is enhancement of the heat transfer coefficient, in others one there is deterioration of it. In parabolic flights the short duration of microgravity conditions (22 seconds) does not allow a full development of flow boiling heat transfer, thus spoiling the experimental evidence. In Table 6 there is a summary of microgravity two-phase flow heat transfer research until 1994 [93]; the papers on gas –liquid two-phase flow are not considered because the purpose of the present review is two-phase flow with phase change of a single fluid component.

Authors	**Reduced Gravity Facility**	**Test fluid**	**Test section Geometry**	**Results**
Papell [94] (1962)	NASA Learjet	Water	7.9 mm ID L = 16.5 cm	Microgravity heat transfer coefficient 16% higher
Feldmanis [95] (1966)	KC-135	Water	9.5 mm ID L = 91.4 cm	Higher boling heat transfer coefficients at microgravity (not explicitly measured)

Reinarts et al. [96](1992)	KC-135	R-12	8.7 mm ID L = 35.5 cm	26% lower condensation heat transfer coefficients at microgravity
Ohta et al.[97] (1994)	MU-300 Aircraft	R-113	8mm ID L = 6.8 cm	In the bubbly and annular flow regime: no microgravity effects. With nucleate boiling suppressed, the heat transfer coefficients were lower at microgravity.

Table 6 Microgravity two-phase flow heat transfer research, concerning phase change of a single fluid component, until 1994 [93].

In 1997 Ohta [19] noted some problems in the existing research in microgravity flow boiling: the available heat transfer data *were* obtained only in the subcooled and low quality region, the effect of gravity was not clarified in a wider quality range and no critical heat flux measurement for the fundamental boiling system has been conducted under microgravity. He measured the heat transfer coefficients of the test fluid Freon 113 for a given quality and heat flux by using a transparent heated tube having an internal diameter of 8 mm. The experimental conditions covering all measurements are: system pressure P=0.11-0.22 MPa; mass velocity G=150 and 600 kg $(m^2\ s)^{-1}$; inlet quality x_{in}=0-0.8; $q'' = 5x10^3\text{-}1.5x10^5\ Wm^{-2}$. Despite the change of g level, a constant flow rate was realised. The inlet quality of the heated tube *was* increased by the preheaters up to x_{in}=0.8 at mass velocity G=150 kg $m^{-2}\ s^{-1}$ for Freon under atmospheric pressure. For the measurements of h for a given x, a constant value of q" is supplied continuously. Since g effects become weak at high G, most experiments were performed at low mass velocity, G = 150kg/m^{2}s. In this paper, reduced gravity level of about 10^{-2}g *was* referred as microgravity. No marked gravity effect on the heat transfer *was* observed in the case of high G because the bubble detachment is promoted by the shear force exerted by the bulk liquid flow and thus no marked change in the bubble behavior and in the heat transfer is recognized with varying gravity level. The effects of gravity on the heat transfer mechanisms are classified in Table 7 by the combination of mass velocity, quality and heat flux.

		Low quality (Bubbly flow regime)	Moderate quality (Annular flow regime)	High quality (Annular flow regime)
Dominant mode of heat transfer (at low mass velocity)	Low heat flux	Nucleate boiling in subcooled or saturated bulk flow of liquid	Two-phase forced convection	Two-phase forced convection
	High heat flux	Nucleate boiling	Nucleate boiling in annular liquid film	Nucleate boiling in annular liquid film

Table 7 Effects of gravity on the heat transfer mechanisms [19]

The heat transfer due to two-phase forced convection changes with gravity: it is enhanced at 2g and deteriorates at mg. In the case of low heat flux and high quality, the effects of gravity on the behavior of annular liquid film are decreased because of the increasing in thickness of annular liquid film and the reduction of turbulence in it. In fact, the effect of the shear force exerted by the vapor core flow with the increased velocity exceeds that of the gravitational force on the behavior of annular liquid film. No marked gravity effect was observed when nucleate boiling was the dominant mode of heat transfer. At high quality, observing the transition of h after the stepwise increase of heat flux, Ohta [19] found that the value that critical heat flux assumes under microgravity is not so different from the result of the terrestrial measurements. The results of microgravity flow boiling experiments conducted in 1993-1999 by Ohta are summarised in [98].

Table 8 gives a summary of the observations on the effect of gravity level on the heat transfer coefficient from different authors.

Author, test fluid and diameter of test section	**Observations on the heat transfer coefficient gravity effects**
Ohta [98] [25] Freon 113 8 mm	- No gravity effects at high q" - In bubbly flow regime and low x, h is rather insensitive to gravity despite the distinct change of bubble behaviour. - No gravity effects for high x - h deteriorates in μg for medium x

---

[25] As in Table 7, only the results at low G are listed. From the experiments, the boundary of low and high G is around $G = 300 kg/m^2s$ and the effects of gravity in extremely low mass velocity $G \leq 100 kg/m^2s$ have not been clarified.

Celata [21,87] FC-72 6, 4 and 2 mm Figure 70	- μg lead to a larger bubble size which is accompanied by a deterioration of h. - As the fluid velocity increases, the influence of g level on h tends to decrease, but this also depends on x.
Luciani et al. [5] HFE-7100 0.49, 0.84, 1.18 mm, Figure 71	- During μg, h is higher in comparison with the 1g, and 1.8 g values - h is higher in the inlet minichannel and then decrease in the flow direction from the inlet to the outlet channel for all gravity levels. In fact, as soon as the vapour occupies the whole of the minichannel, h falls to reach a value that characterizes heat transfer with only vapour phase.
Luciani et al. [6] HFE-7100 0.49 mm Figure 72	- h is higher in the inlet of minichannel independent of the g value and this agrees with the fact that at the inlet the flow has a low percentage of isolated bubbles. - h then decreases with *the flow* direction x and remains constant *in the plain of the channel section*. - in μg h is higher and at the inlet is almost twice the value in 1g, and 1.8 g - no differences between 1g, and 1.8 g

Table 8 Summary of the observations on the influence of gravity on heat transfer coefficient, recently presented in literature.

The inter-relation between the fluid velocity and exit quality on the gravity effect in heat transfer has preliminarily been quantified by Celata and Zummo [21,87]; they assert that the influence of gravity on h decreases with increasing of fluid velocity and they concluded that for low x, gravity influence can be neglected for fluid velocity greater than 25 cm/s while for x> 0.3 h is unaffected by gravity level even at low velocities. In Figure 70 a scheme of the experimental flow patterns observed at 10-2g [21,87] clarifies the condition. The dashed line delimits the gravity influence region from the region unaffected by gravity level; this dashed line moves towards higher ReL for higher tube diameter while it moves toward lower ReL for lower tube diameter.

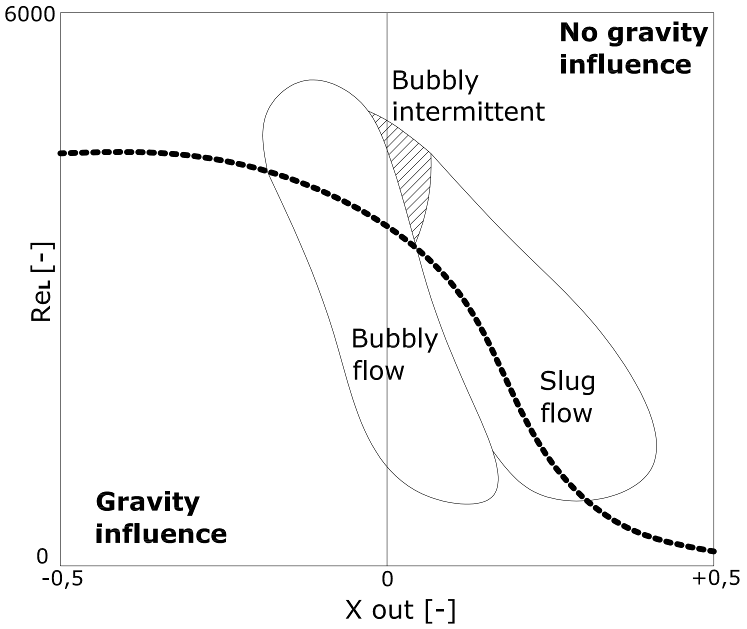

Figure 70 Zero gravity map for the inter-relation between fluid velocity and quality on gravity effect in heat transfer [87].

Luciani et al. [5] use an inverse method to estimate the heat transfer coefficient of HFE-7100 in a rectangular minichannel. In Figure 71 it is possible to see what is summarized in Table 8. Luciani [5] asserts that the microgravity generates vapour pocket structures which fill the width of the minichannel to explain that h is locally higher.

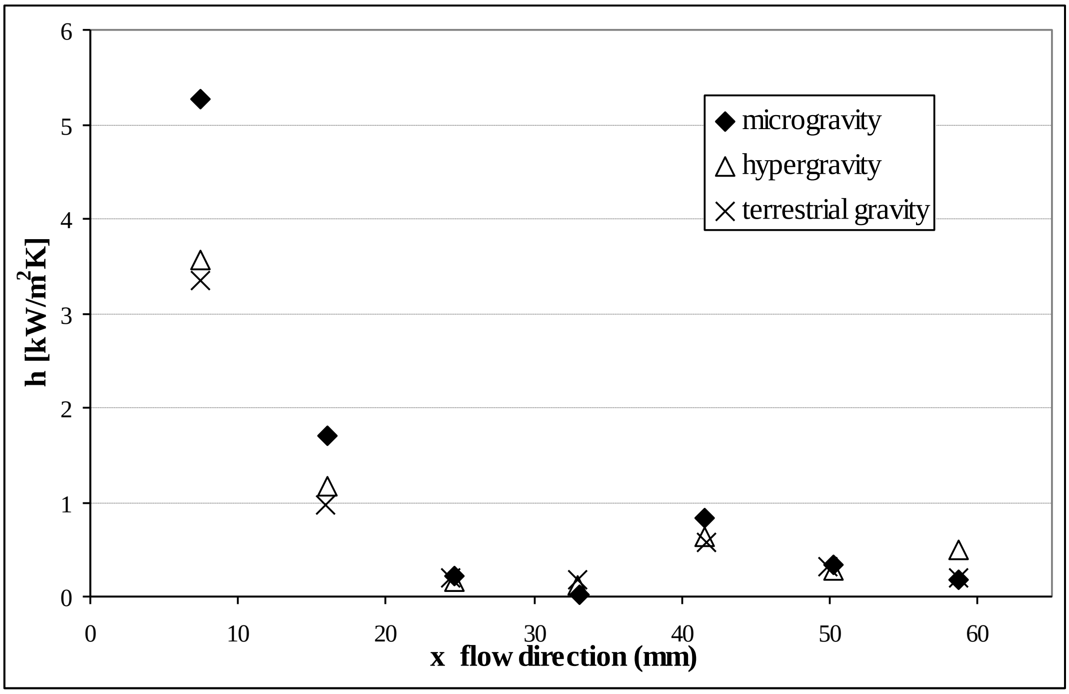

Figure 71 Local heat transfer coefficient as a function of the main flow axis (q"=32kWm^{-2}, Q= 2.6·10^{-4} kgs^{-1}, x=0.26, d$_h$=0.84mm) [5] **Eo=3.67·10^{-3}** in μg, **Eo=0.72** at terrestrial gravity and **Eo=1.3** in hypergravity

Figure 72 present the experimental data published in [6] by Luciani et al. thanks to the experiments done during parabolic flights on board A300 Zero-G [5].

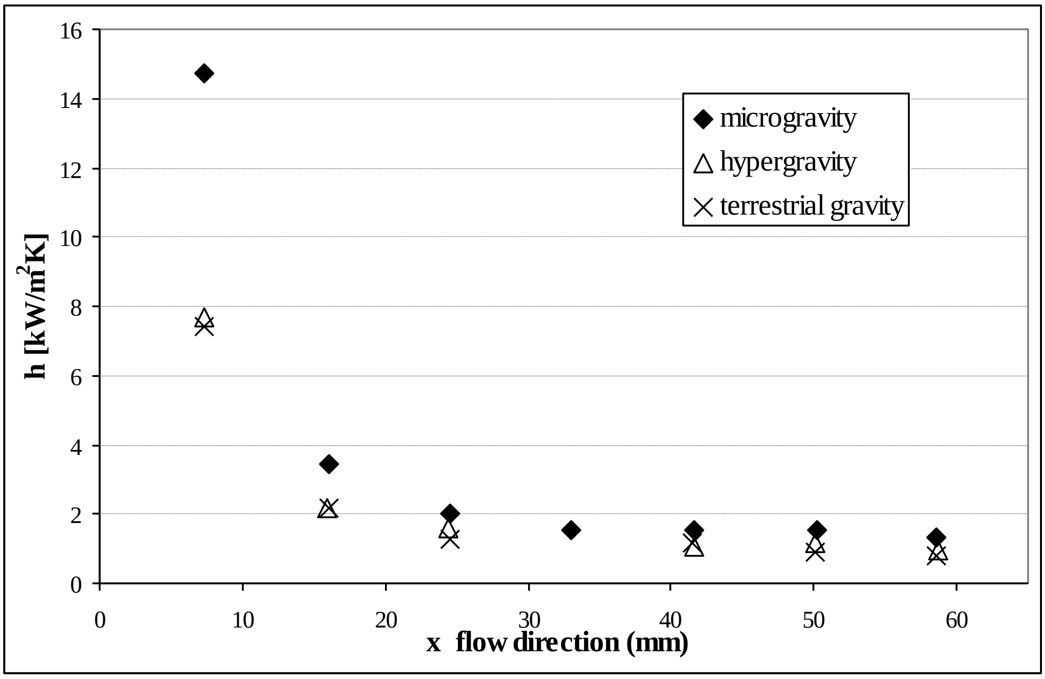

Figure 72 Local heat transfer coefficient as a function of the main flow axis depending on the gravity level (heat flux q"=45 kWm^{-2}, Q= 4.2·10^{-4} kgs^{-1}, d_h =0.49mm) [6]. **Eo=1.25·10^{-3}** in μg, **Eo=0.25**at terrestrial gravity and **Eo=0.44** in hypergravity

The authors [6] underlined that the results obtained in microgravity do not correspond with the theory; in fact generally microgravity conditions lead to a larger bubble size which is accompanied by a deterioration in the heat transfer rate while in [6] the heat transferrin microgravity conditions is higher. None of the existing models can predict the behaviour of the boiling heat transfer coefficient when the gravity level changes; more test are necessary to improve the knowledge and to validate future models.

5.3 CONSIDERATIONS ON THE EÖTVOS NUMBER AND FLOW PATTERNS FOR DIFFERENT GRAVITY LEVELS.

With the purpose to compare the literature experimental data having the same Eo number, **Table 9** provides a group of experimental papers each
characterized by the same Eo number at terrestrial gravity.

Author	Fluid	d_h	E_o	g-level
Lin et al. [11]	R-141b	1.1 mm	1.03	1g [26]
Ong et al. [63]	R-245fa	1.03 mm	1.03	1 g
Revellin et al [83]	R134a	0.8 mm	1.04	1g [27]

Table 9 Experimental papers [11, 63, 83] having the same Eo number.

In **Table 10** are shown the flow patterns and on flow pattern transitions correspondent to data of **Table 9**. Note that the isolated bubble regime includes both bubbly and slug flows.

---

[26] In [11] the quality correspondent to the transition was associated to two different mass fluxes (G=365 kg/m^{2}s and G=505 kg/m^{2}s); since G does not influence Eo, the authors decide to consider the maximum quality range correspondent to each transition.

[27] In [83] the flow patterns are presented only for the 0.5 mm channel; the authors decide to use these flow patterns as data for the 0.8 mm channels since in [83] it is underlined that the 0.8 mm diameter did not show any significant difference to the 0.5 mm channel although bubbly/slug flow was present over a wider range of mass flux.

		Diameter		
Eötvos	**x**	**d_h=0.8mm**	**d_h=1.1mm**	**d_h=1.03mm**
1.03	x<0.005	Bubbly [83]	Confined bubble[11]	Isolated Bubble [63]
	x<0.03	Bubbly, Bubbly-Slug [83]	Slug to Churn [11]	Isolated Bubble [63]
	x<0.16	Bubbly-Slug to Slug [83]	Churn to annular [11]	Coalescing bubble [63]
	x<0.3	Slug to Semi Annular [83]	Annular [11]	Annular [63]
	x<0.4	emi Annular to Annular [83	Annular [11]	Annular [63]
	x>0.4	Annular [83]	Annular [11]	Annular [63]

Table 10 Flow pattern observed in [11, 63, 83] having an Eötvos number equal to 1.03.

From **Table 10** it emerges that, independently from the diameter, the experiments with the same Eo numbers show the same flow pattern at least for a vapour quality x>0.3. It would be interesting comparing experimental data having the same Eo number and very different diameters, for example, data obtained using a 5 mm and 0.5 mm channel size. So far, in literature such data do not exist and hence a specific experimental activity is still necessary.

With the purpose to compare the literature experimental data having the same Eo number and different gravity levels, two groups of experimental papers are presented in **Table 11**.

Author	Fluid	D_h	E_o	g-level
Celata et al. [20, 21, 87]	FC-72	6 mm	0.8	0.01 g
Lin et al. [11]	R-141b	1.1 mm	0.83	1g [28]
Celata et al. [20, 21, 87]	FC-72	4 mm	0.35	0.01 g
Revellin et al [50]	R134a	0,5 mm	**0.38**	1g [29]

Table 11 Two group of experimental papers, [11, 20, 21, 87] and [20, 21,50, 87], characterized by the same Eo number.

In Table 12 there are the observations on flow pattern and on flow pattern transitions correspondent to the data of **Table 11**.

			Gravity level	
			1g	**0g**
Eötvos	**0.35**	x<0.04	Bubbly [50]	Bubbly [20,21,87]
		x<0.19	Slug [50]	Slug and intermittent [20,21,87]
		x<0.4	Semi-annular [50]	Intermittent flow [20,21,87]
		x<0.82	Annular [50]	not examinated
	0.8	x<0.005	Confined bubble [11]	Bubbly[20,21,87]
		x<0.03	Slug to Churn [11]	Bubbly [20,21,87]
		x<0.16	Churn to annular [11]	Bubbly-Slug and Slug [20,21,87]
		x<0.3	Annular [11]	Slug [20,21,87]
		x<0.4	Annular [11]	Intermittent [20,21,87]
		x>0.4	Annular [11]	not examinated

Table 12 Flow pattern observed in [11, 20, 21, 50, 87] in conditions of terrestrial gravity and microgravity classified in terms of Eötvos number.

---

[28] In [11] the quality correspondent to the transition was associated to two different mass fluxes ($G=365\ kg/m^2s$ and $G=505\ kg/m^2s$); since G does not influence Eo, the authors decide to consider the maximum quality range correspondent to each transition.

[29] All the data were observed for $G=500\ kg/m^2s$.

From Table 12 it emerges that the Eo number is not sufficient to characterize the flow patterns, since, for the same Eo value, the correspondent flow patterns at terrestrial gravity and microgravity are different. Hence there is the necessity of systematic experimental tests made at the same Eo number in order to check if these dimensionless parameters could describe what is really changing from macroscale to microscale, i.e. the confinement of the bubbles. So far, Eo number is not a good parameter to describe this transition and is not adeguate to make a comparison between microgravity and microscale, since, as evidenced above, it is not significant in microgravity situations.

PART II: EXPERIMENTAL SECTION

Chapter 6

Experimental setup

6.1 EXPERIMENTAL TEST RIG

An existing test rig, built by Stefano Dall’Olio during his PhD and described in [100,101] was implemented to study flow boiling of refrigerants inside a mini channel with particular emphasis of Onset of Nucleate Boliling (ONB). There has been a development of the test section and of the heating system and a new data acquisition system and post processing software were built. A schematic view of the experimental apparatus is given in Figure 73. It consists of two main circuits: the test section loop and a secondary loop, where the fluid is thermally controlled and the entire vapor formed in the test section is condensed. The pressure of the system depends on which refrigerant there is. When R134a is used, the loop is filled with refrigerant till the internal pressure reaches 6 bar, in order to bring the saturation temperature (Tsat=21°C) just below the ambient temperature. When

R245fa is the fluid to be tested, the system pressure reaches 1,6 bar and the saturation temperature is Tsat=27°C. In Table 13 the experimental conditions are summarized.

Refrigerant	**Inlet pressure [MPa]**	**Tsat [°C]**	**G range [kg/m^{2}s]**	**q" [kW/m^2]**
R-134a	0.537-0.590	18-21	50-137	0-22
R-245fa	0.148-0.165	25-28	50-115	0-26

Table 13 Summary of the experimental conditions

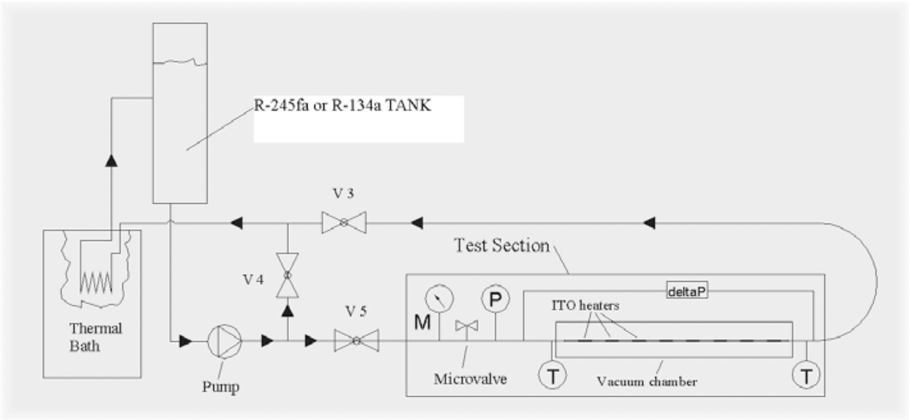

Figure 73 Experimental test rig scheme

The test section tube is made of high precision glass (DURAN) with an internal diameter of 4 mm. The mini-channel is enclosed in a co-axial glass tube with 6 cm external diameter vacuumed in order to eliminate the convection heat losses and consider only radiation losses. The transparent ITO film, characterized by a mean electric resistance of 50 Ohm/m^2, covers eight portions of equal length (40 mm) and each independent portion is used to electrically heat the glass surface allowing to observe and record the boiling mechanisms taking place inside the tube with a high speed PCO® camera. The temperature of the tube wall is monitored by means of eight K-type thermocouples placed on each heater.

Figure 74 presents the test section while Figure 75 is a zoom on one of the eight ITO heaters.

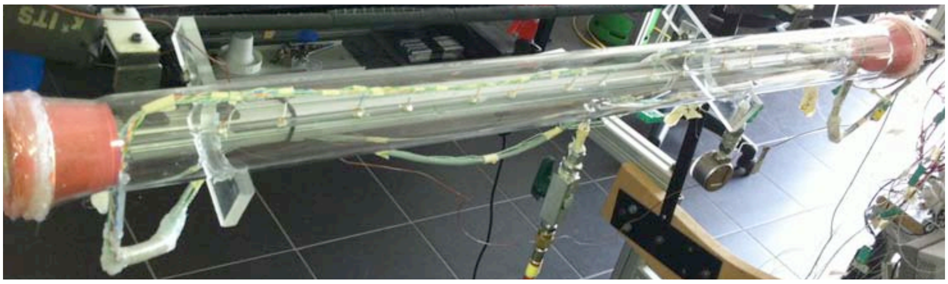

Figure 74 The test section inside the co-axial glass tube.

Figure 75 shows the k-type thermocouple and the electrical wires that provide power to the heater. These are fixed to the ITO coating thank to a conductive epoxy, CW2400, that is the silver part of the minichannel in Figure 75.

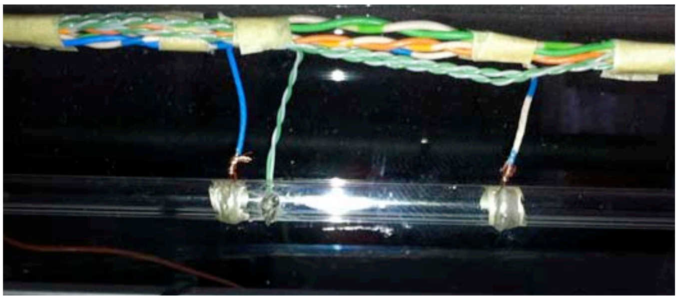

Figure 75 A part of the minichannel where there is the ITO heater.

Refrigerant temperature is measured at the inlet by a RTD PT-100 and at the outlet of test section by a K-type thermocouple. The pressure is measured at the inlet of the test section, after the micro-regulation valve, by PSE 510[30] pressure sensor. The fluid inlet saturation temperature T_{sat} is estimated with the help of the NIST REFPROP libraries (Lemmon et al. 2007) from this inlet pressure.

An helix type heat exchanger is cooled by means of a thermal bath HAAKE C50P® which maintains propylene glycol at a constant pre-imposed temperature; this unit is necessary to define the operating experiment temperature and to condense the fluid coming from the test section in the form of wet vapor. The mass flow rate, measured by a Coriolis flow meter CORI-FLOW M53[31], can be adjusted by working on the micro regulation valve positioned at the inlet of the test section, by closing the bypass valve or by changing the pump speed.

6.2 EXPERIMENTAL PROCEDURE

First of all, the experimental apparatus is vacuumed using a vacuum pump and then the secondary loop is filled with the refrigerant while the test section loop is closed. Then the valves are opened so that the two loops are connected and the refrigerant can move toward the test section; the secondary loop is then close and the test section loop is vacuumed and that is again connected with the secondary loop. These steps are repeated for three times in order to minimize the presence of air in the experimental apparatus. There can be gas dissolved in the refrigerant tank used to fill the loop according to standard Ahri 700-2011[32]. During the procedure described above, the valve between the inlet of the test section and the pressure sensor PSE 510 was closed to prevent the vacuum pump to damage the pressure sensor. After the "vacuum procedure", the valve was opened to allow the measure by the pressure sensor.

Before running the experiment the coaxial glass chamber is vacuumed, the mass flux is adjusted to the desired value and then the

---

[30] Operating pressure range 0-10 bar, output signal 0-5 V

[31] Flow rate: 0.5- 5 kg/h

[32] 1,5%vol a 25°C.

fluid inlet temperature is set in order to enter the test section in sub-cooled condition of maximum 2 °C, so as to work as close as possible to the saturated boiling conditions. To set the temperature of the fluid, it is necessary to close the test loop while the fluid has to circulate into the secondary loop. The power supplied to the fluid is set to the desired value that is maintained until a steady tube temperature is reached; mass flux, temperature, pressure and power input values are stored using the data acquisition systems and this is described in section 6.3. The power supplied to the fluid is increased, starting from 0 W, with increments of 0.5W in the regions near the onset of nucleate boiling and of 1 W in the other regions until the maximum desired power (11 W for R134a and 12 W for R245fa). Then the power level was decreased from the maximum value to 0 W with step of 1 W. Figure 76 shows an example of the experimental profile of T_{win} during the steps of increasing power.

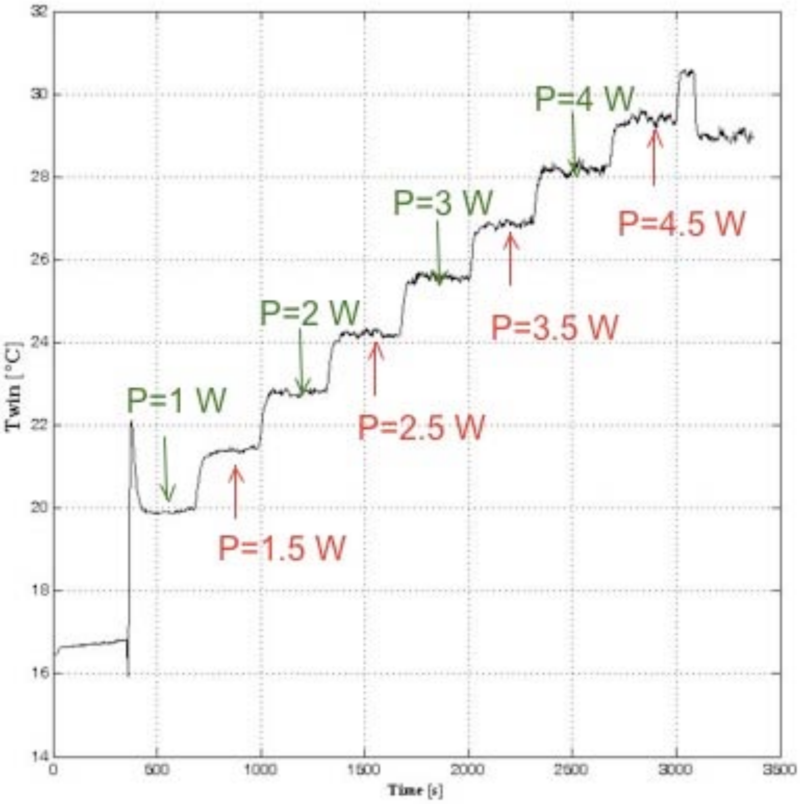

Figure 76 Experimental profile of Twin during the steps of increasing power.

For each heat flux step, the correspondent flow pattern is visualized and recorded at a speed of 1000 frames/s using the high-speed camera, as shown in **Errore. L'origine riferimento non è stata trovata.** In order to provide the necessary amount of light, a continuous electricity lamp of 65W is positioned in front of the camera. Being the lamp temperatures very high, a glass covered with an infrared filtering film has been positioned between the lamp and the test section, in order to minimize the radiated power.

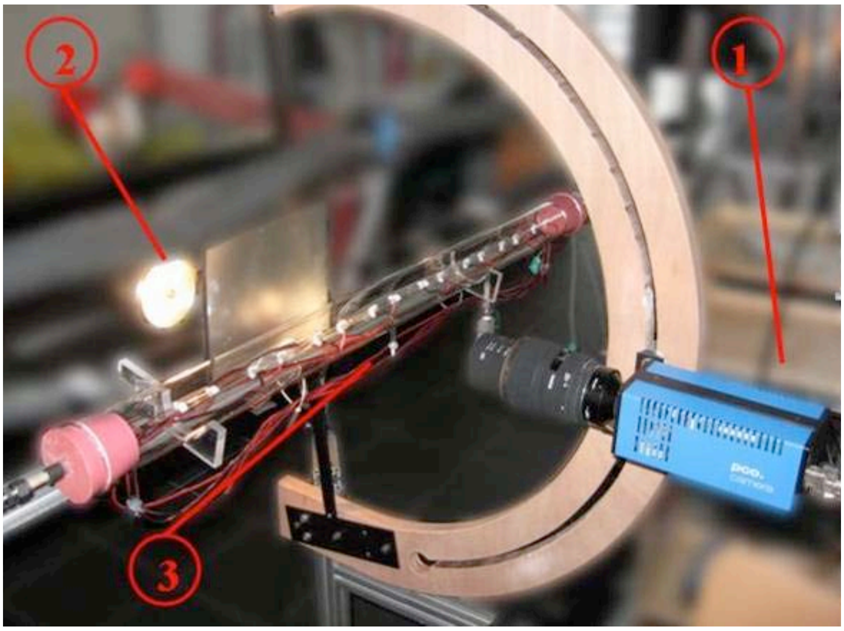

Figure 77 View of the test section: high speed camera (1), the light source (2) and the test section (3)

The experimental procedure explained above, is repeated two times for every mass flux value examined in order to check the repeatability. The internal temperature of the heated wall T_{win} is calculated starting from the temperature of the external mini-channel, T_{wout}, measured by the K-type thermocouple and considering heat conduction through the glass according to this:

$$T_{win} = T_{wout} - \frac{\ln\left(\frac{r_{ext}}{r_{int}}\right)}{2k\pi L_H} \cdot P \tag{II-1}$$

Finally the following temperature difference, called wall superheat, is calculated at each heat input level:

$$\Delta T_{sh} = T_{win} - T_{sat} \tag{II-2}$$

Also the vapor quality is calculated along the channel since, in case there is a phase change in the channel, it increases in the direction of flow. If there is not thermal equilibrium between the phases, one cannot calculate the quality merely by knowing the inlet quality and the heat flux from the wall. Unfortunately, it is very difficult to measure or calculate with precision the quality of the liquid-vapor mixture flowing in a channel where a change of phase takes place A fictitious quality, the so called thermodynamic equilibrium quality can be calculated by assuming that both phases are saturated, i.e. that their temperatures are equal to the saturation temperature corresponding to their common pressure. The so-called thermodynamic equilibrium quality can be calculated as:

$$x = \frac{h(z) - h_L}{h_{LV}} \tag{II-3}$$

where h_L [J/kg] is the enthalpy of the saturated liquid, h_{LV} [J/kg] is the latent heat of vaporization, and $h(z)$ [J /kg] is the enthalpy at a cross section z, which can be calculated from:

$$h(z) = h_{in} + \frac{1}{q}\int_0^z P'(z)dz \tag{II-4}$$

where h_{in} is the enthalpy of the fluid at the inlet and $P'(z)$ [W/m] is the heat input from unit of length. Since we are making experiments with only one heater, the expression of the vapour quality becomes easier:

$$x = \frac{P}{qh_{LV}} \tag{II-5}$$

Regarding the experimental accuracies, the mass flow rate accuracy is ±1% while the pressure accuracy is ± 2% in the pressure range of R-245fa experiments (≈ 1.6 bar) and it is ± 0.5% in the pressure range of R-134a experiments (≈ 5.6 bar). The thermocouples have an accuracy of ± 0.2°C after calibration.

6.3 DATA ACQUISITION AND POST PROCESSING SOFTWARE

Thermocouples signals, the mass flow rate and pressure are acquired using Agilent 34970A and stored in the PC thanks to a dedicated data acquisition software that has been developed with Simulink. Figure 78 presents the control panel of the software that acquire the data from two heaters, named 1 and 2 in the figure below; a second similar software was developed to acquire data from the eight heaters contemporaneously but, since the experiments were performed using only one heater, the first one was used.

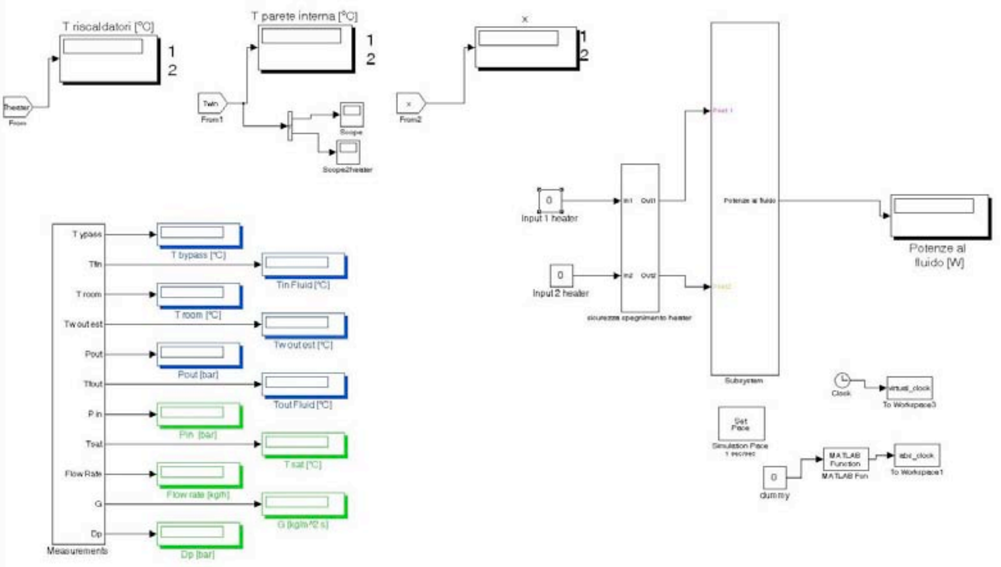

Figure 78 Control panel of the Simulink acquisition data system

The data are transmitted from Agilent 34970A to Simulink with a frequency of around 2Hz. Since we are interested only in stationary conditions, i.e. the temperature of the heated wall is constant inside a fixed range, a dedicated Matlab program rejects the data obtained in the transient time and then it calculates the mean values of the experimental data.

The PC controls ITO coatings power through the NI (National Instrument) USB-6008[33] acquisition and control device and by the specifically designed electronic board, which is supplied with a 56V DC power supplier. In Figure 79 there is a scheme of the signals acquisition connections.

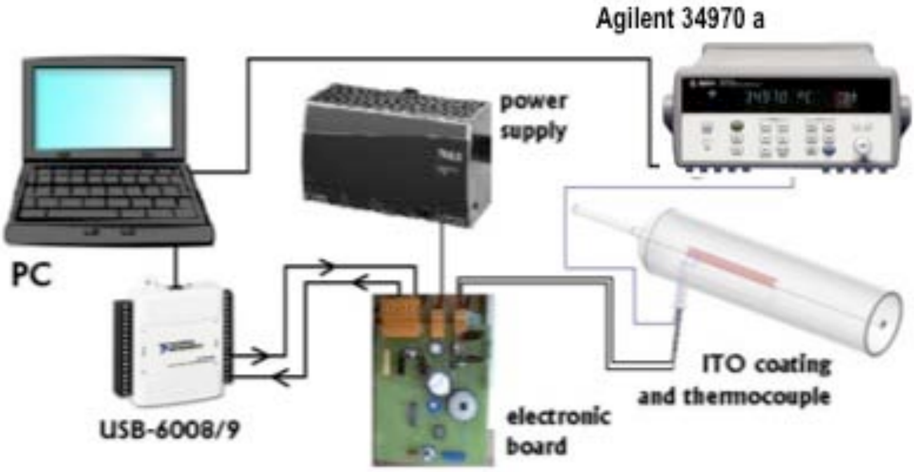

Figure 79 Experimental setup acquisition scheme.

Each NI USB-6008 controls two ITO heaters and it communicate with two electronic boards, one for each heater. The electronic board, showed in Figure 80 Figure 81, applies the correct value of voltage to the heater in order to reach the desired electrical power and amplifies the coating voltage and current signals adequately, so that these can be acquired by the USB-6008 and transmitted to the PC. Typically, the range of the final resistance of each heater is between 65 and 300 Ω. The radiation heat transfer between the ITO coating and the environment is numerically estimated and subtracted to P, the total power supplied to the ITO coatings in order to obtain the net thermal power supplied to the working fluid; this value is controlled with a standard PID (proportional-integral-derivative). The contribute of the

---

[33] Input and output range:

axial conduction along the tube was considered in [sdo] thanks to a numerical analysis. According to this study [sdo], the new equivalent length of the coating, depending on the amount of power provided by the heater, should be used to calculate the heat flux. Since the length of each coating can vary for less than one millimeter for each side and this means that the length of the coating is 40 mm ±5%, the new equivalent length was considered only when the difference between this and the nominal length, i.e. 40 mm, is bigger than 5% and this happens, according to [101] for power bigger than 5 W.

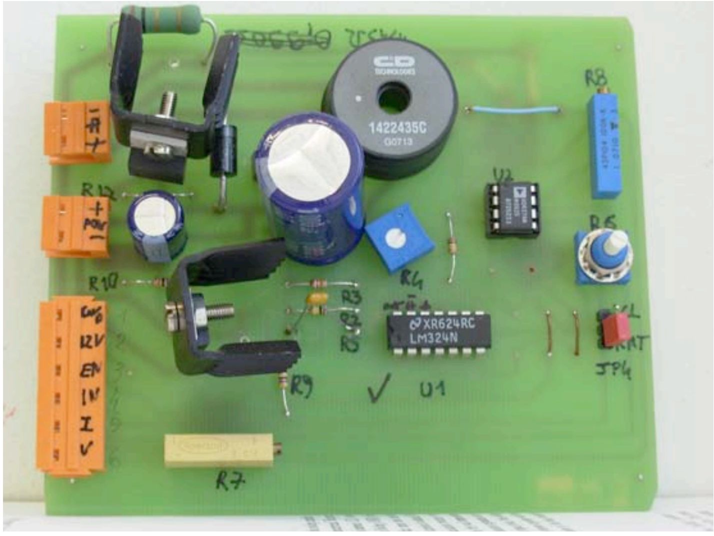

Figure 80 Front of the new electronic board

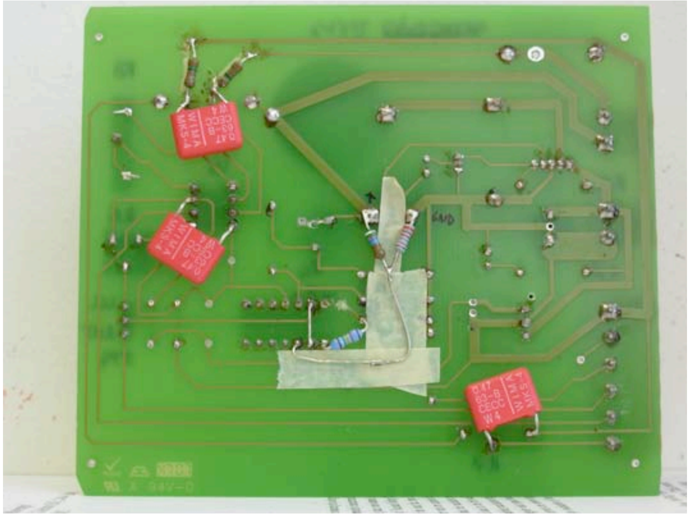

Figure 81 Back of the new electronic board

Since we are interested only in stationary conditions, i.e. the temperature of the heated wall is constant inside the range of ± 0.2°C that is the accuracy of the thermocouples after the calibration, a dedicated Matlab program was developed. It rejects the data obtained in the transient time associated to each step power and then it calculates the mean values of the experimental data. These are stored for post processing and they are:

- the total power supplied to the heaters, P
- the net power supplied to the fluid, Pf
- the vapour quality, calculated according to (II-5)
- the internal temperature of the heated wall, T_{win}
- the inlet temperature of the fluid, T_{in}
- the inlet pressure, p_{in}, and the corresponding saturation temperature, T_{sat}
- the mass flux, G
- the wall superheat, according to (1)
- the heat flux calculated from the net power supplied to the fluid, q"

Also the standard deviations of these data are calculated and stored. For the heat flux, the uncertainty has been calculated starting from the standard deviation of the power and applying the error propagation theory.

Chapter 7

Experimental analysis of R-134a

7.1 STATE OF THE ART ON ONSET OF NUCLEATE BOILING

Focusing on the Onset of Nucleate Boiling, which marks the boundary between the single-phase and two-phase heat transfer region, Ghiaasiaan et al. [102] developed a semiempirical method for the estimation of the incipient boiling heat flux. Bang et al. [103] performed a digital photographic study of subcooled flow boiling to observe near-wall structures, giving primary attention to bubble formation and bubble coalescence in the bubble layer; Callizo et al. [104] presented boiling curves for R-134a. Liu et al. [105] investigated experimentally ONB of water in a rectangular micro-channel developing an analytical model able to predict the heat flux and the bubble size at the onset of boiling. Recently, Hong et al. [106] found that the heat flux and wall superheat needed to initiate the nucleate boiling in narrow rectangular channel under static conditions, increased with the mass flux and the inlet subcooling.

7.2 BOILING CURVES

The heat flux versus the ΔT_{sh}, calculated by means of Eq. (1), represents the boiling curve obtained during the experiments. During the experimental campaigns, several boiling curves are obtained at different mass flux levels, G = 50, 80,100, 115 and 137 kg/m^{2}s. A gradual activation of the nucleation sites, starting from the upper side of the heater to the lower side, was evidenced for all the mass flux tested. Figure 82, Figure 83Figure 84Figure 85 and Figure 86 are the boiling curves obtained ad the different mass flux tested; the red line corresponds to the increasing in the heat flux while the green line to the decreasing in it.

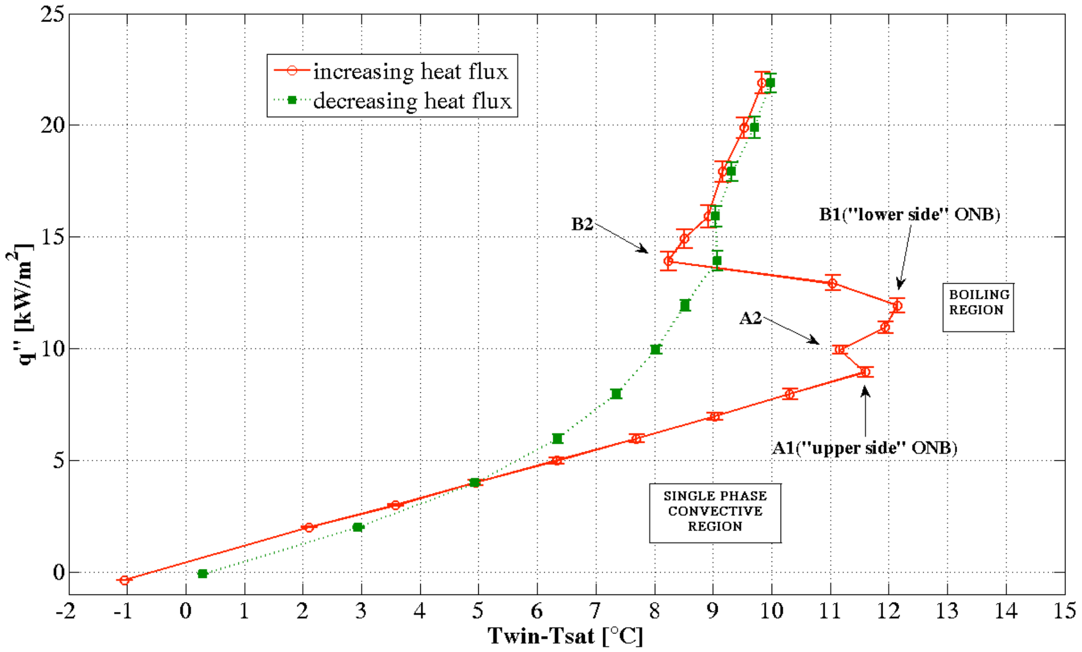

Figure 82 Boiling curve obtained for G = 137 kg/m^{2}s.

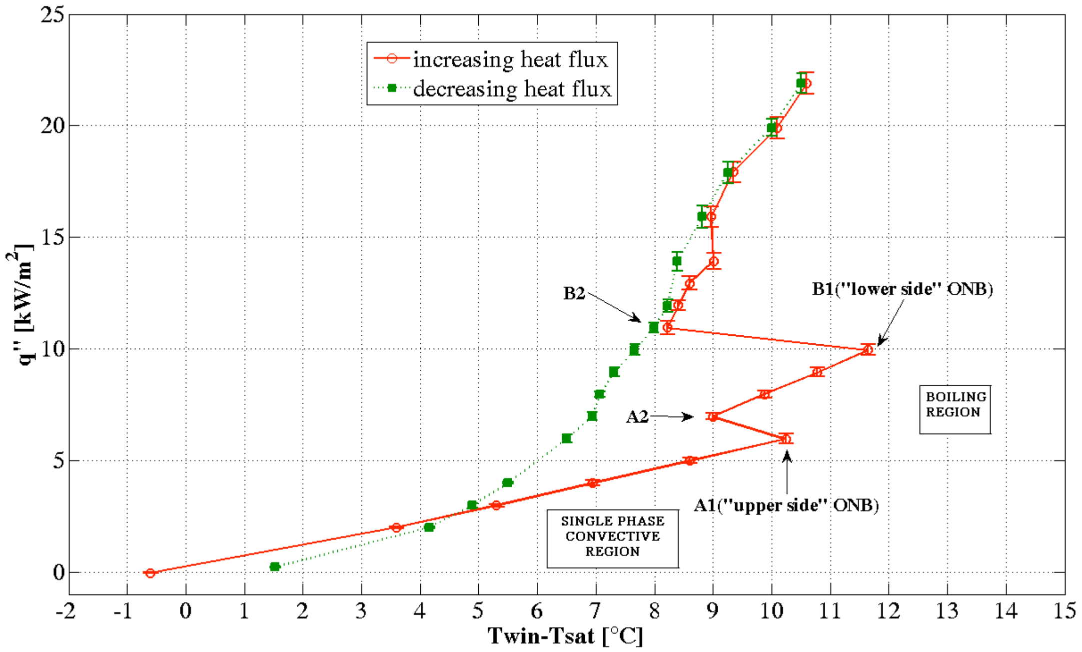

Figure 83 Boiling curve obtained for G = 115 kg/m^{2}s.

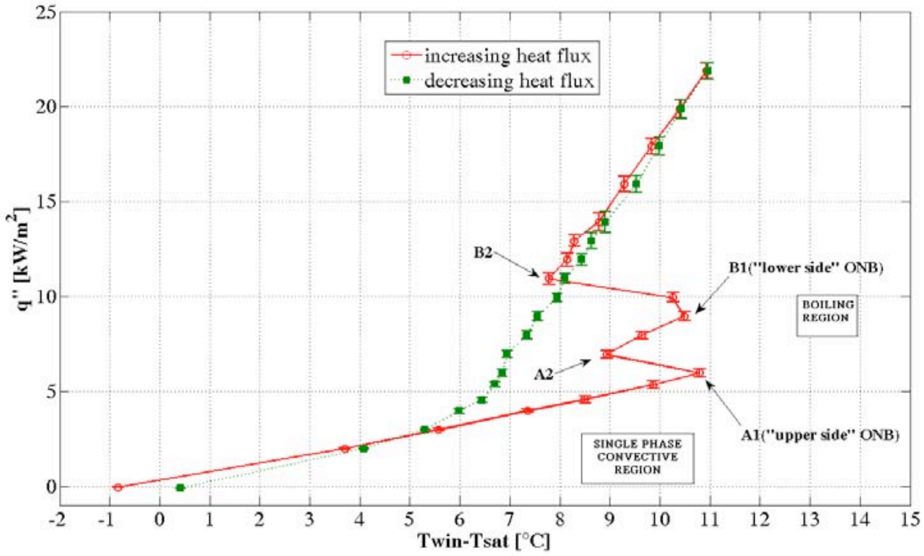

Figure 84 Boiling curve obtained for G = 100 kg/m^{2}s.

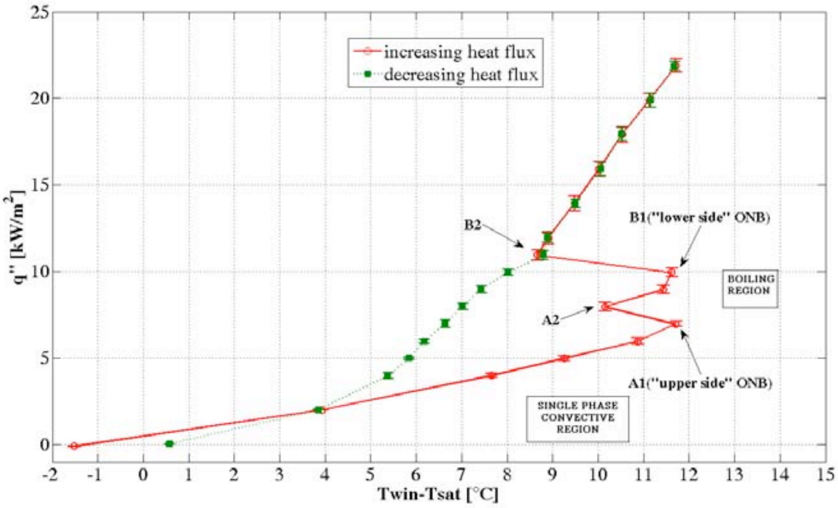

Figure 85 Boiling curve obtained for G = 80 kg/m^{2}s.

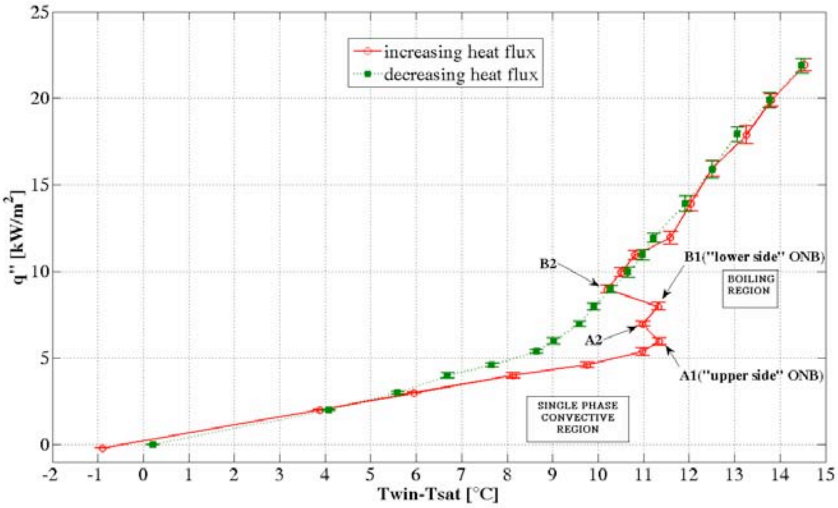

Figure 86 Boiling curve obtained for G = 50 kg/m^{2}s.

In the boiling curve obtained for G=50kg/m^{2}s, the point B1 occurs immediately after the point A2 but it must be stressed that this boiling curve has some characteristic features that will be evidenced in the next section, thank to the flow pattern observation. The values of ΔT_{sh} during the increasing of q″ are different from those obtained during the reduction of q″ and this is the so called boiling hysteresis. Two main regions, namely single phase forced convective region and boiling flow region are clearly identified in the figures above, and these regions are separated from the “upper side” ONB. Regarding the red lines in the previous figures, q″ increases almost linearly with the increasing in ΔT_{sh} in the single phase convective region; the liquid in contact with the tube internal surface soon becomes superheated, whereas the fluid bulk remains saturated. Further increase in the heat flux results in an increased wall superheat; vapor nuclei are activated and the boiling process occurs in the upper side of the tube. The ONB heat transfer mechanism causes the heating surface temperature to drop; this results in a reduction of the Twin and therefore a sudden drop of ΔT_{sh} is observed. A further increase of q″ results in an increase of the number of bubble sites and ΔT is slowly increasing; looking to the boiling curves obtained by increasing the heat flux, a second temperature drop is clearly recognizable. This occurs when the nucleation starts also in the lower side of the heater; this is due to a heterogeneous non-uniform flow boiling process. In order to clarify the nomenclature A1, A2, B1, B2 used in the figures above, it is important to define:

- A1 as the “upper side” ONB point; it corresponds to the maximum heat flux value at which only liquid phase exists;

-A2 corresponds to the temperature drop occurring after A1. Then a further increase of the heat input level results in an increase in ΔT_{sh};

- B1 is the “lower side” ONB, defined as the maximum ΔT below which boiling is activated only in the upper side of the heater;

- B2 corresponds to the maximum temperature drop occurring after B1.

In B2 the nucleation starts also in the lower part of the heater, it would be clear in section 7.3 where the flow patterns are presented. After B2 the flow boiling regime is homogeneous and the red curve trend is more regular since the wall superheat increases almost linearly with the heat flux. For every G the temperature drop associated to the "lower side" ONB is bigger than that associated to the "upper side" ONB. The fact that for the "lower side" ONB the nucleate boiling mechanism starts from the lower side of the heater and cause a bigger temperature drop, can be linked to an enhanced heat transfer phenomenon. In fact, despite the inner tube diameter is 4mm, the Bond number is still relatively high (Bo (30°C) = 22.78); this means that buoyancy forces still play an important role. In such conditions the bubbles nucleate, grow, and detach from the inner tube surface; finally they lift off to the upper side of the tube by the buoyancy forces and drag by the flow mainstream in the axial direction. This combination of two phase transport phenomena enhance the heat transfer process and leads to a larger temperature drop during the "lower side" ONB event.

It was expected that the boiling mechanism from the lower side of the heater, needs higher activation energy. So, despite the fact that the time is usually not considered in flow boiling literature, part of this study focused on estimating the amount of thermal energy needed to reach the Onset of Nucleate Boiling (ONB) at different mass fluxes. Going on with the research, the energy necessary to reach the "upper side" ONB and the "lower side" ONB was evaluated taking into consideration the duration of each heat flux step. At the end, the energy associated to upper and lower side ONB was considered not a good parameter to describe the physics of the boiling mechanism since, repeating several times the experiments, the energy values correlated to the upper and lower side ONB fall in a too big range of values.

7.3 FLOW PATTERNS

Thanks to the transparency of the ITO heaters, it is possible to visualize the earliest stages of the bubbles formation and boiling phenomena. The flow patterns associated to points A2, B1 and B2 are very important since they are linked to the "upper side" ONB, "lower side" ONB and to the consequent temperature drops. Point A1 corresponds to only saturated liquid and because of this, the correspondent flow pattern is not presented.

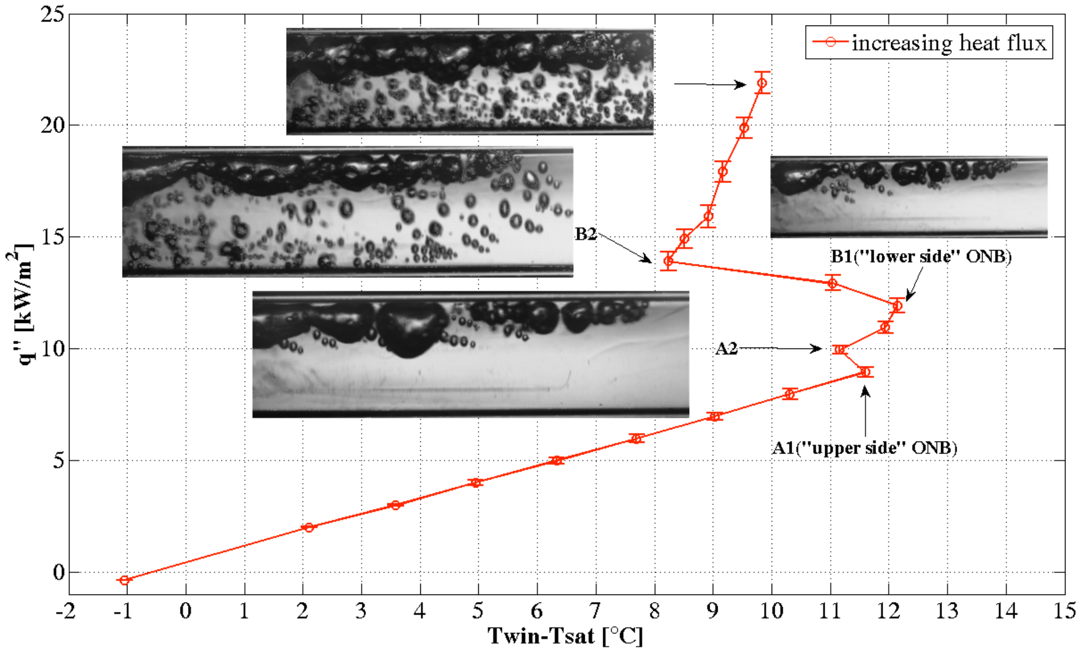

Figure 87 Flow patterns associated to point A2, B1, B2 and to q″=16 kW/m^2 for G = 137 kg/m^{2}s.

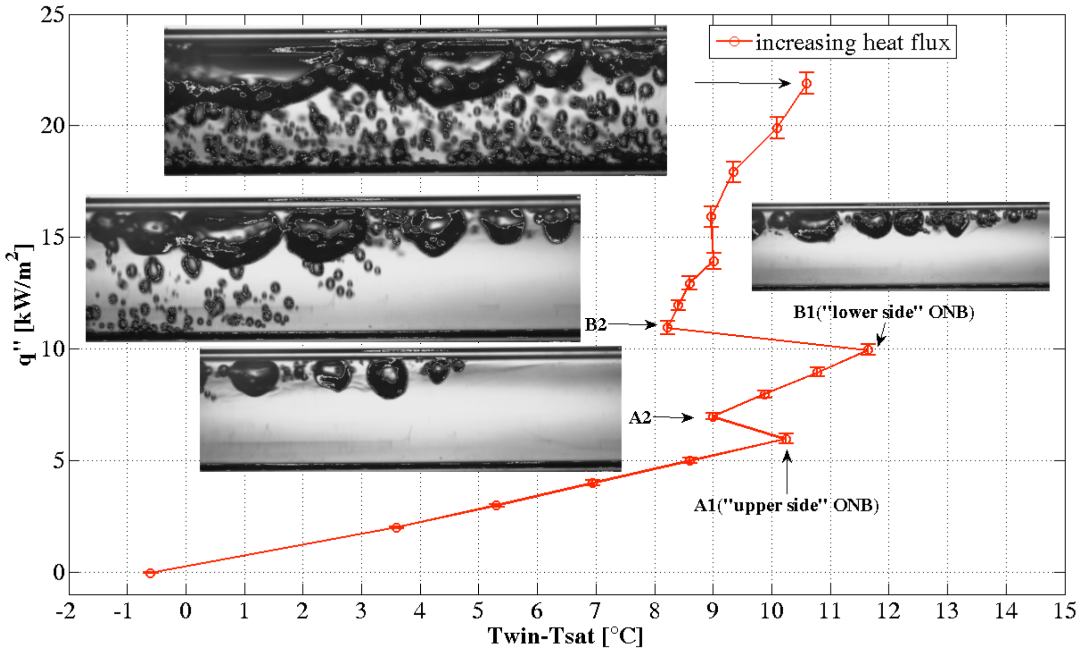

Figure 88 Flow patterns associated to point A2, B1, B2 and to q″=16 kW/m^2 for G = 115 kg/m^{2}s.

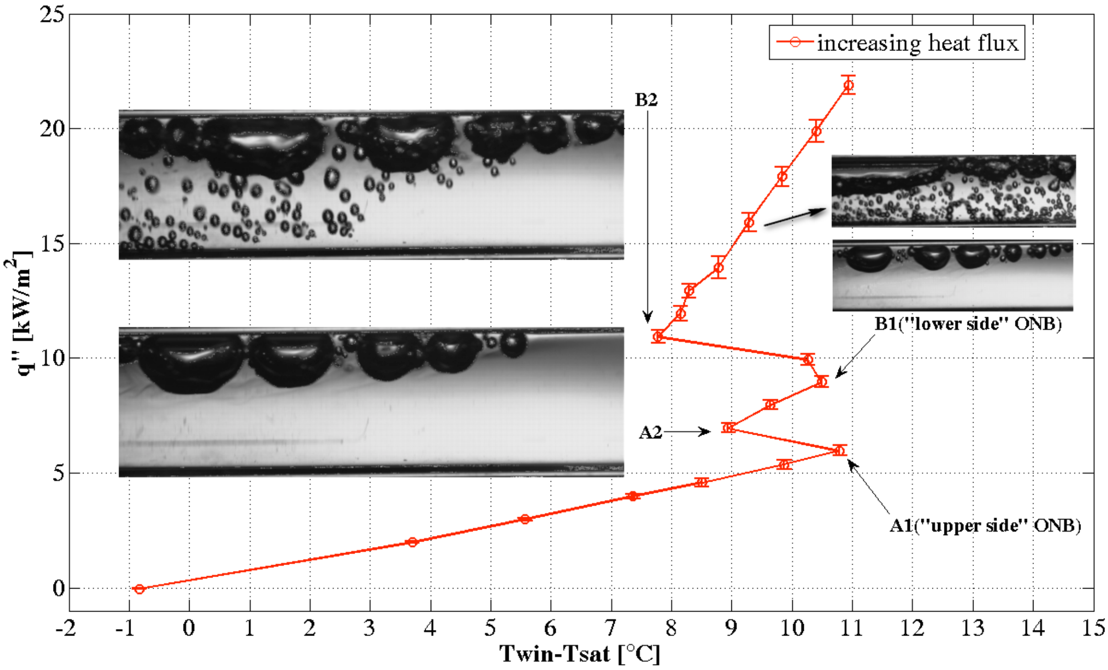

Figure 89 Flow patterns associated to point A2, B1, B2 and to q″=16 kW/m^2 for G = 100 kg/m^{2}s.

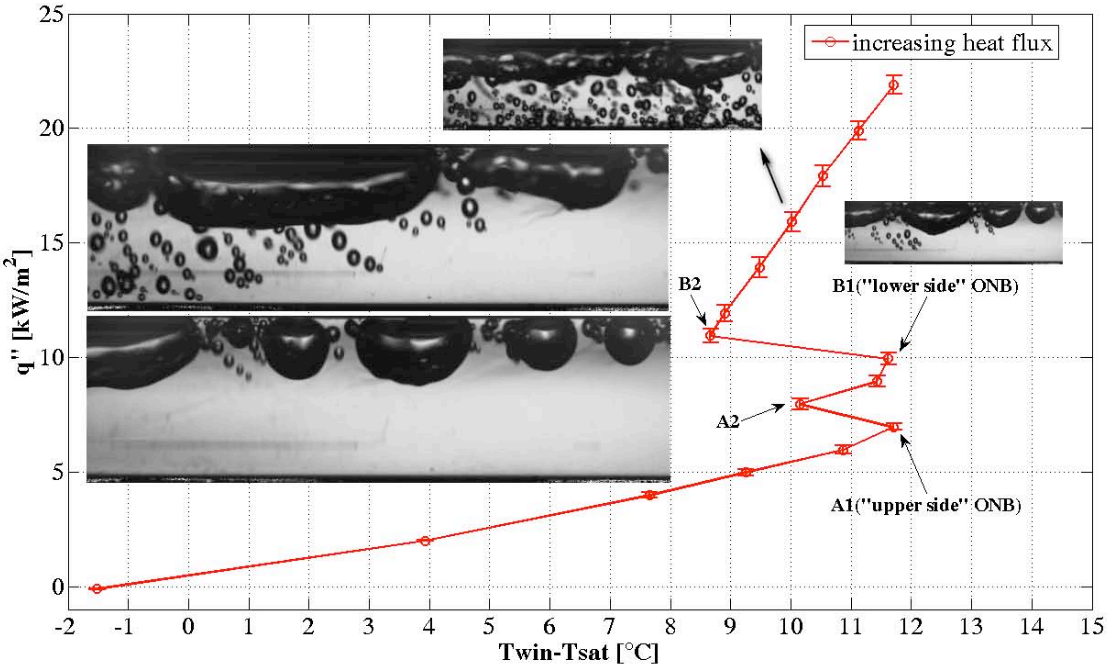

Figure 90 Flow patterns associated to point A2, B1, B2 and to q″=16 kW/m^2 for G = 80 kg/m^{2}s.

Thanks to the figures above, the definitions of A1,A2,B1,B2 become immediately clear. From the figures, in A2 the nucleation starts in the upper side of the heater while in B2 it starts also in the lower side of the heater.

The data obtained for G= 50 kg/m^{2}s have the particularity that point A1 do not correspond to only liquid phase. In fact, immediately after the first nucleation event, that happens before point A1, stratified flow appears without temperature drop and boiling curve trend alteration. The definition of A1 of the previous section is no longer valid, since in this point there are already vapor and liquid together; it was decided to refer to point A1 as “upper side” ONB also for G= 50 kg/m^{2}s only for sake of homogeneity.

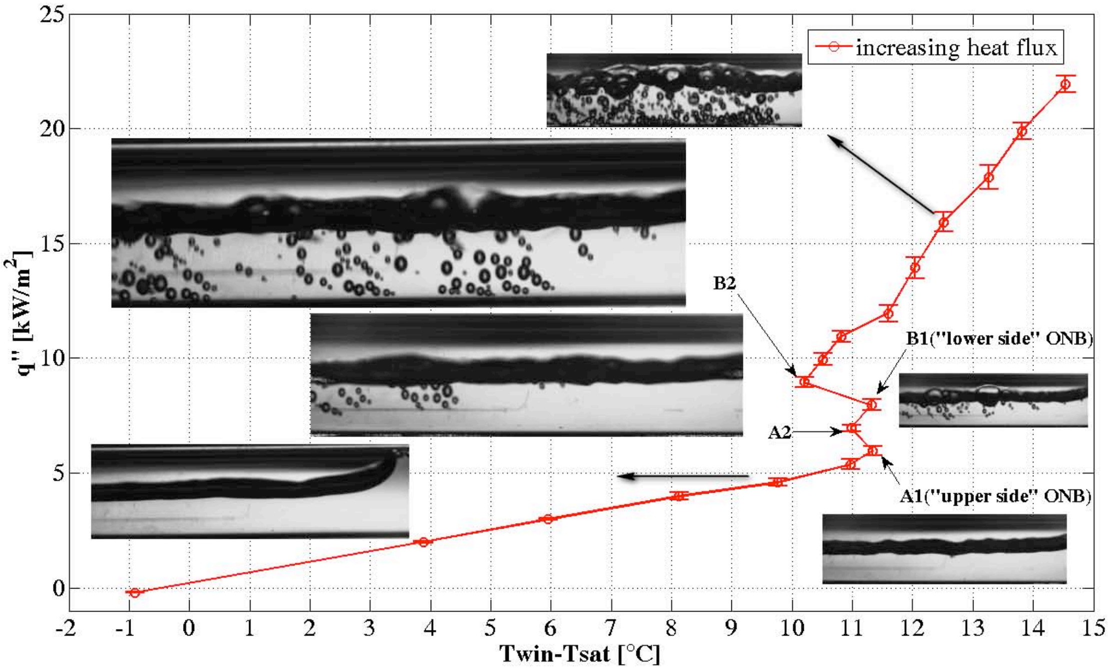

Figure 91 Flow patterns associated to point A1, A2, B1, B2 and to q″=4.6 kW/m^2 and q″=16 kW/m^2 for G = 50 kg/m^{2}s

Only the tests with G = 50 kg/m^{2}s exhibit this different behavior with respect to the other tests; the two phases, vapor resides at the top and the liquid at the bottom of the mini-channel, are completely separated by an undisturbed horizontal interface. Increasing the heat flux, the interface becomes disturbed and there is a little drop in the temperature related to point A1 and A2. Finally nucleation starts in the lower side of the heater (B1), and the boiling process becomes more homogeneous after B2.

It would be interesting to investigate the cases with a lower specific flow rate G<50 kg/m^{2}s in order to understand if this particular behavior still occurs. Some tests were done with G=30 kg/m^{2}s and, qualitatively speaking, immediately after the first nucleation event, always from the upper side of the heater, stratified flow appeared but the boiling curve trend was not altered (no temperature drop). There is only one temperature drop associated to the nucleation from the lower side of the heater.

7.4 HEAT TRANSFER COEFFICIENT

7.4.1 State of the art of the Heat Transfer Coefficient for R-134a

Callizo et al. [104] investigated subcooled flow boiling of R-134a and they presented a comparison between the R-134a experimental heat transfer coefficients and the predictions from classical correlations, showing that the classical correlations available from the literature were not able to predict the heat transfer coefficients in all tested conditions. Focusing on the heat transfer coefficient of R134a, Copetti et al [107] compared their experimental data to results predicted by existing correlations for the same operational conditions. They founded that the calculated coefficient agreed well with measured data within a range 35% for saturation temperature of 22 °C and that the Kandlikar and Balasubramanian correlation [108] gave the best predictions.

Shiferaw et al [60] conducted similar experiments in a 1.1 mm diameter tube showing that the R-134a heat transfer coefficients were not affected by mass flux nor vapor quality, but they increase with the heat flux level and the saturation pressure. Ong and Thome [63] tested three different refrigerants, namely R-134a, R-236fa and R-245fa founding that the heat transfer coefficient is mostly affected by the heat flux level at low vapor quality while the mass flux effect is predominant at high vapor quality. In 2011 Saisorn et al. [109] tested R134a in an horizontal mini-channel (1.75mm internal diameter); they compared their experimental data with the predictions of the three zone model by Thome et al. [26,49]. They founded that the heat transfer coefficient increases with increasing heat flux but is mostly independent of mass flux and vapor quality. Saisorn et al. [110] investigated the flow boiling of R134a in horizontal and vertical minichannels founding that the heat transfer coefficient depends on the flow direction and that the gravitational effect tends to be insignificant when the mass flux is low. The experimental results of Da Silva Lima et al. [111] clearly show that a local minimum heat transfer coefficient systematically occurs within slug flow pattern or near the slug-to-intermittent flow pattern transition; the vapor quality at which the local minimum occurs seems to be primarily sensitive to mass velocity and heat flux.

7.4.2 *The Experimental Heat Transfer Coefficient versus heat flux , wall superheat and versus vapor quality*

From each boiling curve obtained decreasing the heat flux, it was possible to calculate the heat transfer coefficient, HTC, using a linear regression according to the equation:

$$q'' = HTC\ (T_{w,in} - T_{sat}) \qquad \text{(II-6)}$$

In the following figures, the HTC values are presented with the error bars; the uncertainty analysis is based on the standard error obtained from the linear regression.

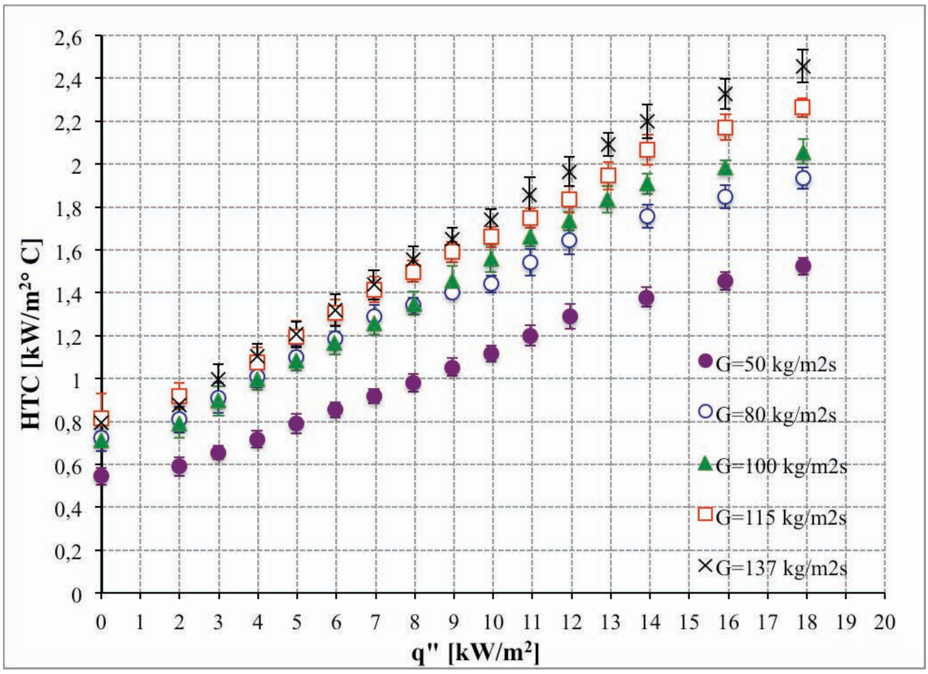

Figure 92 The heat transfer coefficient as function of the heat flux for all the mass fluxes tested.

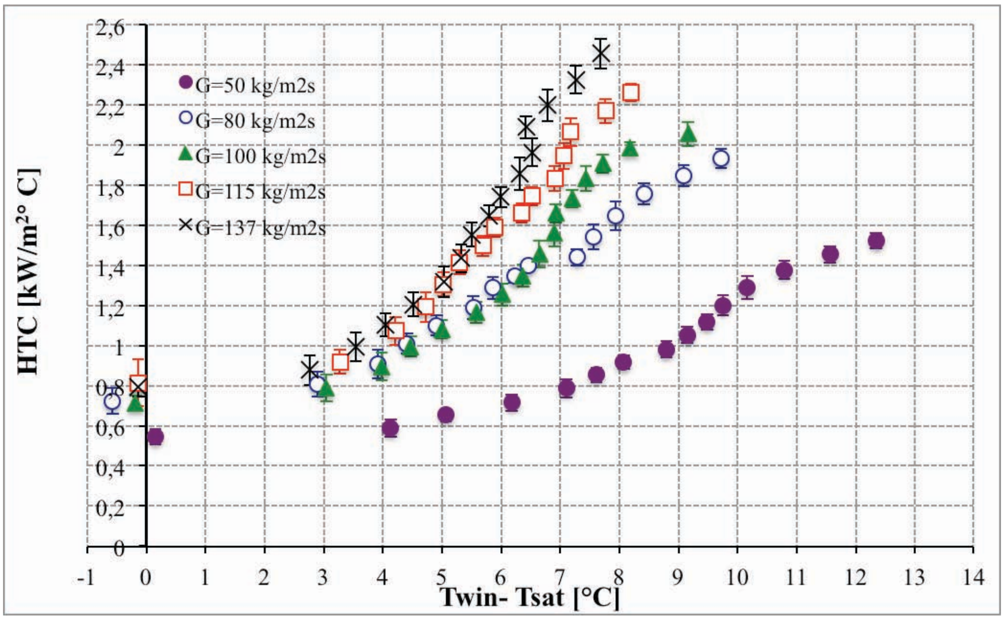

Figure 93 The heat transfer coefficient as function of the wall superheat for all the mass fluxes tested.

From the figures above, the HTC, estimated at a fixed heat flux value or wall superheat value, increases for increasing value of G. **Errore. L'origine riferimento non è stata trovata.** presents the HTC as function of the vapor quality; it increases for increasing value of G. From this figure, it emerges that we are studying flow boiling in a very narrow range of quality, that it x<0.1.

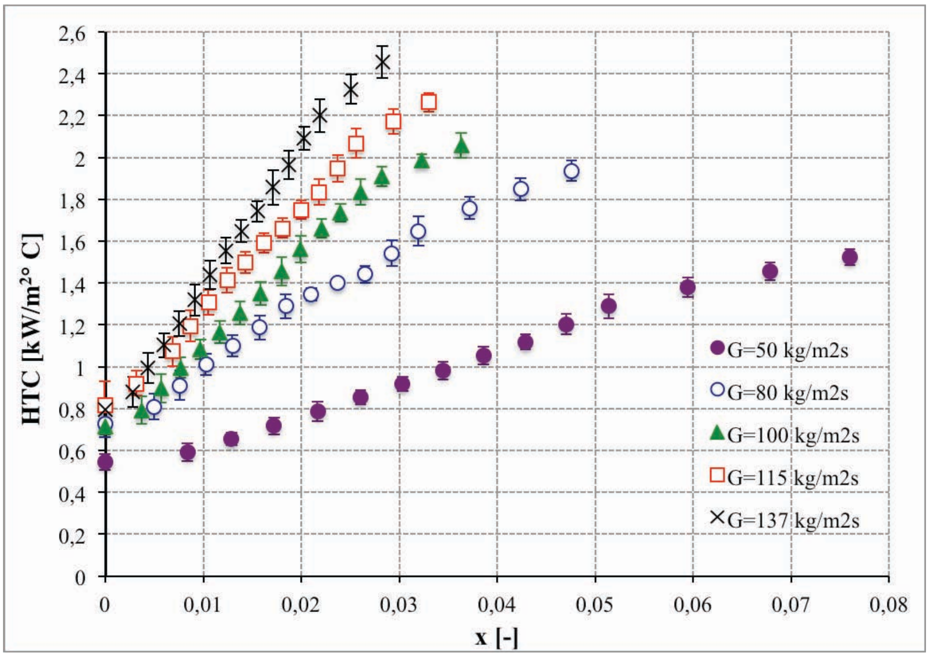

Figure 94 The heat transfer coefficient as function of the vapor quality for the different mass fluxes tested during the experimental campaign with R-134a.

7.5 CONCLUSIVE CONSIDERATIONS ON R-134a EXPERIMENTS

Saturated heterogeneous non uniform flow boiling of R134a has been experimentally investigated at five different mass flux levels with particular emphasis on the onset of nucleate boiling. The boiling curves evidenced the existence of hysteresis; a high-speed camera was employed to visualize the bubble evolution at the earliest stages of their nucleation. Results show that nucleation always starts in the upper side of the heaters. Only increasing the heat flux, the nucleation sites in the lower part of the heater are activated and boiling starts also in the lower part of the heater. There are two different temperature drops linked to the “upper side” and “lower side” ONB. For each mass flux values tested, the temperature drop associated to the “lower side” ONB is always bigger than this correspondent to the “upper side” ONB. The fact that the nucleation always starts in the upper side of the heater could be caused by the non homogeneous ITO coating. But the “upper side” and “lower side” ONB were observed repeating the experiment using eight different ITO heaters in different positions along the tubes. The plasma coating procedure can originate the fact that the ITO thickness presents the same non-uniformity for all the 8 heaters. But in this case, rotating the channel of 180° some differences should be observed while, also after the experiments that have been done after the rotation of 180°, the boiling always starts in the upper side of the heater. In next chapter this nucleation from the upper side of the heater would be investigated also using another refrigerant.

The heat transfer coefficient was estimated as function of the heat flux, of the wall superheat and of the vapor quality for all the mass fluxes tested; it emerges that the HTC values increases with G and that the difference in the HTC between the different G values increases a lot passing from the single phase to the two phase region.

Chapter 8

Experimental analysis of R-245fa

8.1 BOILING CURVES

The heat flux versus the ΔT_{sh}, calculated by means of Eq. (1), represents the boiling curve obtained during the experiments. During the experimental campaigns, several boiling curves are obtained at different mass flux levels, G = 50, 80,100, 115 kg/m^{2}s. A gradual activation of the nucleation sites, starting from the upper side of the heater to the lower side, was evidenced for all the mass flux tested. Figures 95-98 are the boiling curves obtained ad the different mass flux tested; the red line corresponds to the increasing in the heat flux while the green line to the decreasing in it.

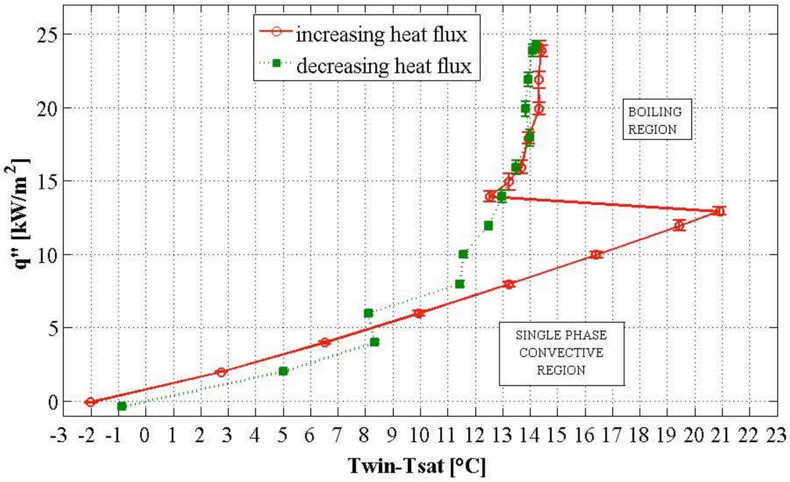

Figure 95 Boiling curve obtained for G=115 kg/m^{2}s

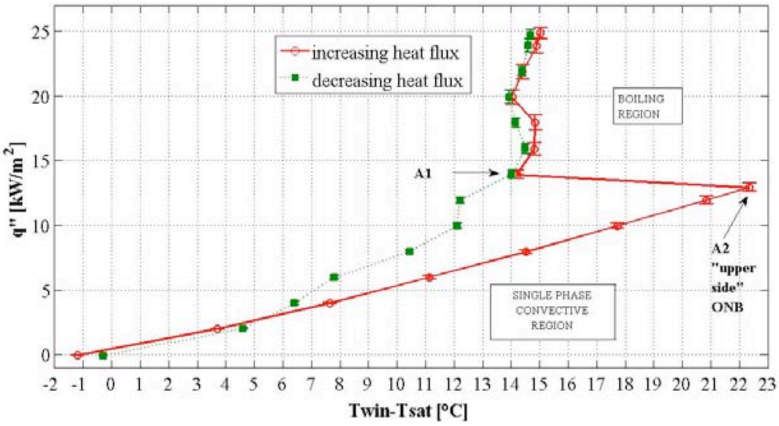

Figure 96 Boiling curve obtained for G=100 kg/m^{2}s

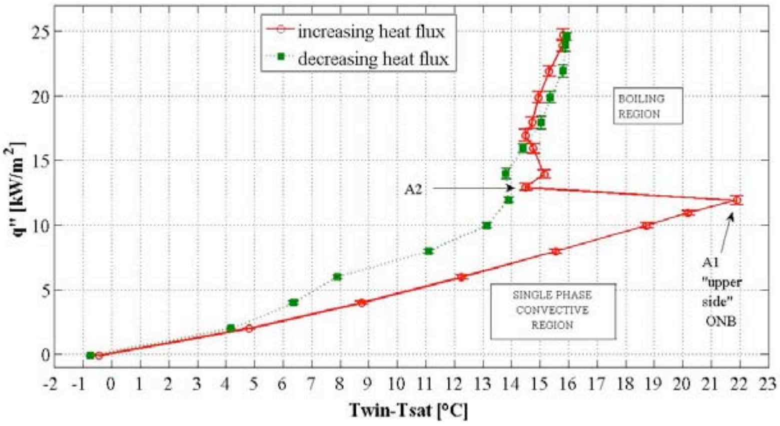

Figure 97 Boiling curve obtained for G=80 kg/m^{2}s

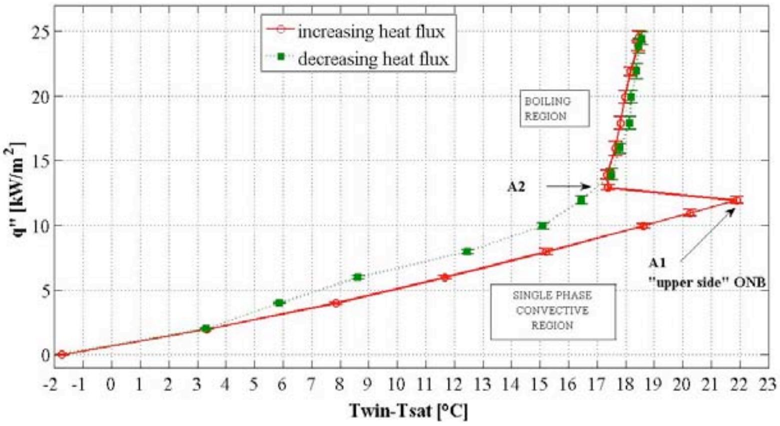

Figure 98 Boiling curve obtained for G=50 kg/m^{2}s

In the boiling curves the values of ΔT_{sh} during the increasing of q″ are different from those obtained during the reduction of q″ and this is the so called boiling hysteresis. Regarding the red lines in the previous figures, q″ increases almost linearly with the increasing in ΔT_{sh} in the single phase convective region; the liquid in contact with the tube internal surface soon becomes superheated, whereas the fluid bulk remains saturated. Further increase in the heat flux results in an increased wall superheat; vapor nuclei are activated and the boiling process occurs in the upper side of the tube. The ONB heat transfer mechanism causes the heating surface temperature to drop; this results in a reduction of the Twin and therefore a sudden drop of ΔT_{sh} is observed. From this point, called A” in the previous figures, there is the “ boiling region” where a further increase of q″ results in a slower increase of ΔT_{sh}. In this region there is activation of the nucleation sites also from the lower side of the heater but this is not associated to a second temperature drop like in R134-a experiments. The nomenclature A1, A2, B1, B2 introduced in chapter 7 is used partially also in this chapter. In the figures above there are points A1 and A2 that are respectively:

- A1: the “upper side” ONB point; it corresponds to the maximum heat flux value at which only liquid phase exists;

-A2 corresponds to the temperature drop occurring after A1. Then a further increase of the heat input level results in an increase in ΔT_{sh}.

In A2 the nucleation starts in the upper part of the heater and the correpondent flow pattern would be presented in next paragraph. After A2, the the red curve trend is regular since the wall superheat increases almost linearly with the heat flux for G=50 kg/m^{2}s and G=115 kg/m^{2}s. For G=80 kg/m^{2}s and G=100 kg/m^{2}s instead, the red curve trend is not regular immediately after A2 and it becomes regular after few heat flux step. This not regular trend could be justified by the fact that after A2 the nucleation gradually starts also in the lower part of the heater but there are few bubbles that appear and disappear and anly increasing the heat flux there is a complete activation of the nucleation from the lower side.

8.2 FLOW PATTERNS

Thanks to the transparency of the ITO heaters, it is possible to visualize the earliest stages of the bubbles formation and boiling phenomena. The flow patterns associated to point A2 is very important since the nucleation starts in this point and causes the temperature drop evidenced in last paragraph. Point A1 corresponds to only saturated liquid and because of this, the correspondent flow pattern is not presented.

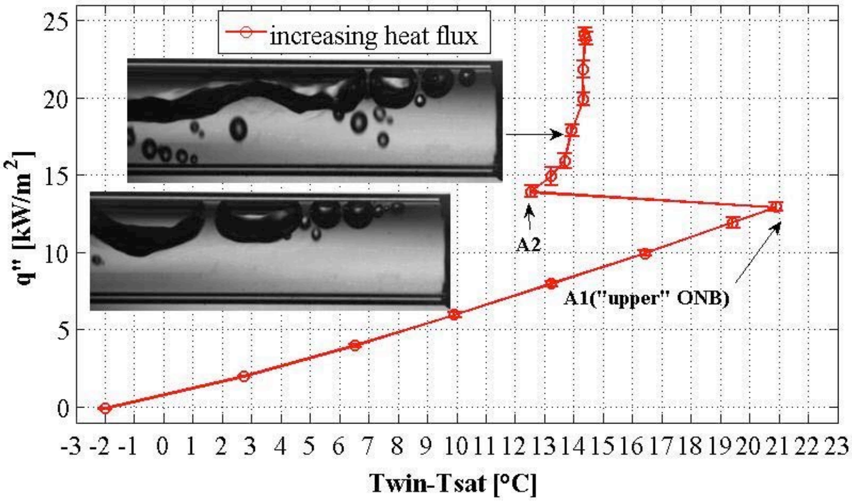

Figure 99 Flow patterns associated to point A2 and to q″=18 kW/m^2 for G = 115 kg/m^{2}s

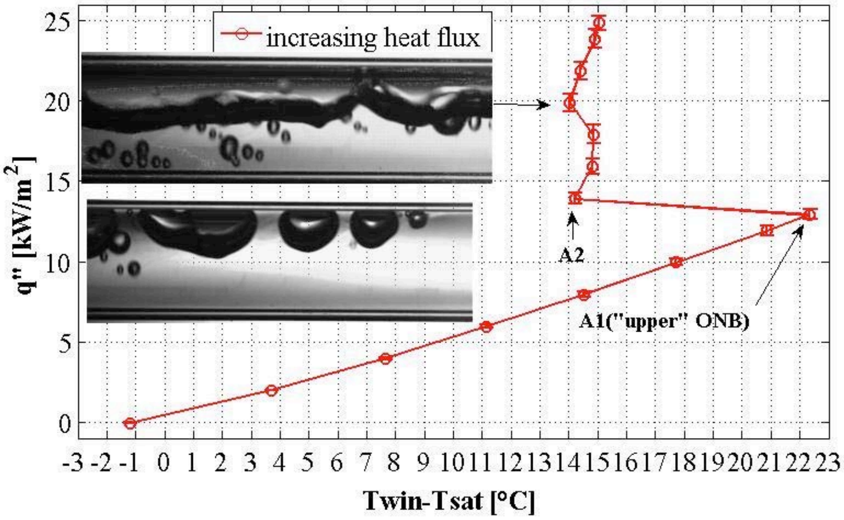

Figure 100 Flow patterns associated to point A2 and to q″=20 kW/m^2 for G = 100 kg/m^{2}s

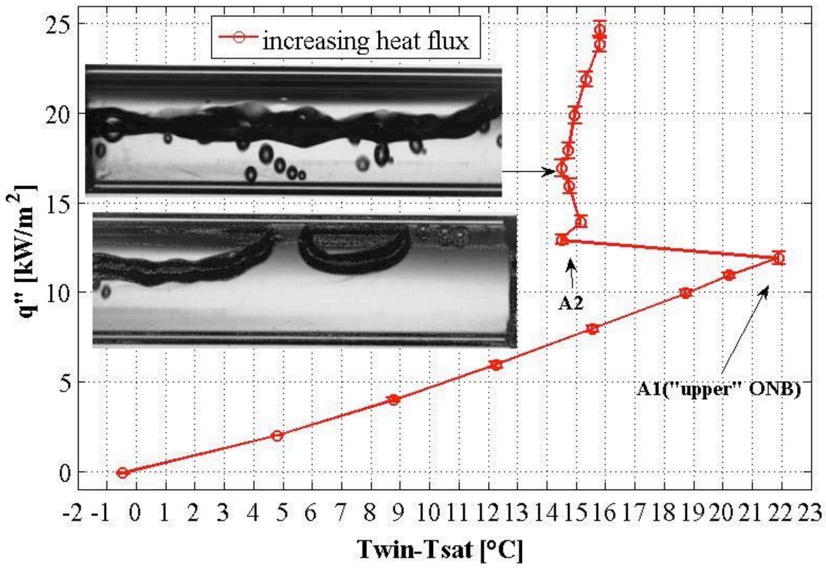

Figure 101 Flow patterns associated to point A2 and to q″=17 kW/m^2 for G = 80 kg/m^{2}s

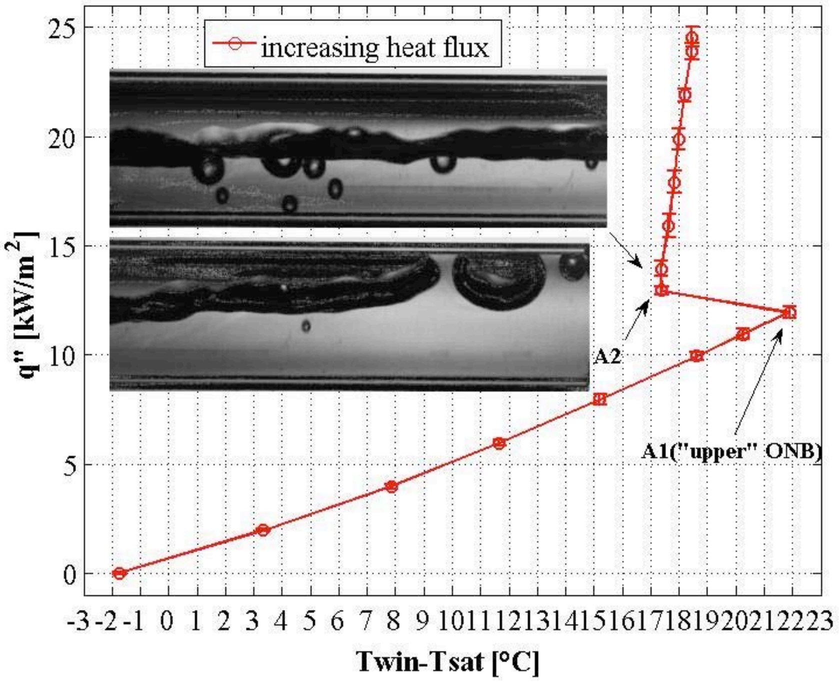

Figure 102 Flow patterns associated to point A2 and to q″=14 kW/m^2 for G = 50 kg/m^{2}s

From the figures above, in A2 the nucleation starts in the upper side of the heater. Then, increasing the heat flux, the nucleation also starts in the lower side of the heater but, since it is not associated to any temperature drop, for sake of homogeneity this point has not a specific nomenclature. In each boiling curve above, the point associated to the nucleation from the lower side is evidenced and the corresponding flow pattern is presented. The data obtained for G= 50 kg/m^{2}s have not the particularity that point A1 do not correspond to only liquid phase, founded during R-134a experiments. In R-245fa experiments, the first nucleation event happens in point A2 and stratified flow appears associated to temperature drop. So point A1 is still the “upper side” ONB also for G= 50 kg/m^{2}s .

8.3 HEAT TRANSFER COEFFICIENT

8.3.1 State of the art of the Heat Transfer Coefficient of R-245fa

Ong and Thome [**Errore. Il segnalibro non è definito.**] tested three different refrigerants, namely R-134a, R-236fa and R-245fa founding that the heat transfer coefficient is mostly affected by the heat flux level at low vapor quality while the mass flux effect is predominant at high vapor quality. Tibiriçá and Ribatski [112] present experimental flow boiling heat transfer results in a horizontal 2.3 mm I.D. stainless steel tube with R134a and R245fa as working fluids. They found that the heat transfer coefficient is a strong function of heat flux, mass velocity and vapor quality. They compared their experimental data against ten flow boiling predictive methods from the literature and founding that Liu and Winterton [113], Zhang et al. [114] and Saitoh et al. [115] captured most of the experimental heat transfer trends. Agostini et al. [116] focused on flow boiling heat transfer of R-245fa and founded three significant trends for the heat transfer coefficient; it increases with x and it is independent of heat flux ang mass flux at low heat flux. At medium heat flux, the heat transfer coefficient increases with the heat flux, increases slightly with G and it is independent of x. At high heat flux, the heat transfer coefficient decreases with increasing q" and x and increases with G.

8.3.2 The Experimental Heat Transfer Coefficient versus heat flux, wall superheat and versus vapor quality

From each boiling curve obtained decreasing the heat flux, it was possible to calculate the heat transfer coefficient, HTC, using a linear regression according to the equation (II-6).

In the following figures, the HTC values are presented with the error bars; the uncertainty analysis is based on the standard error obtained from the linear regression.

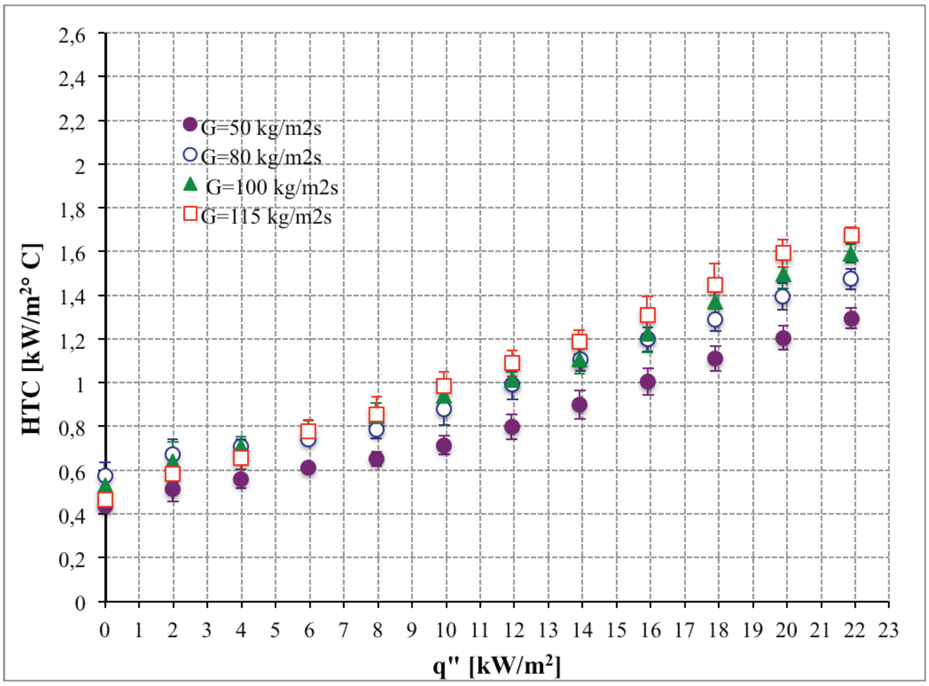

Figure 103 The heat transfer coefficient as function of the heat flux for the different mass fluxes tested during the experimental campaign with R245fa.

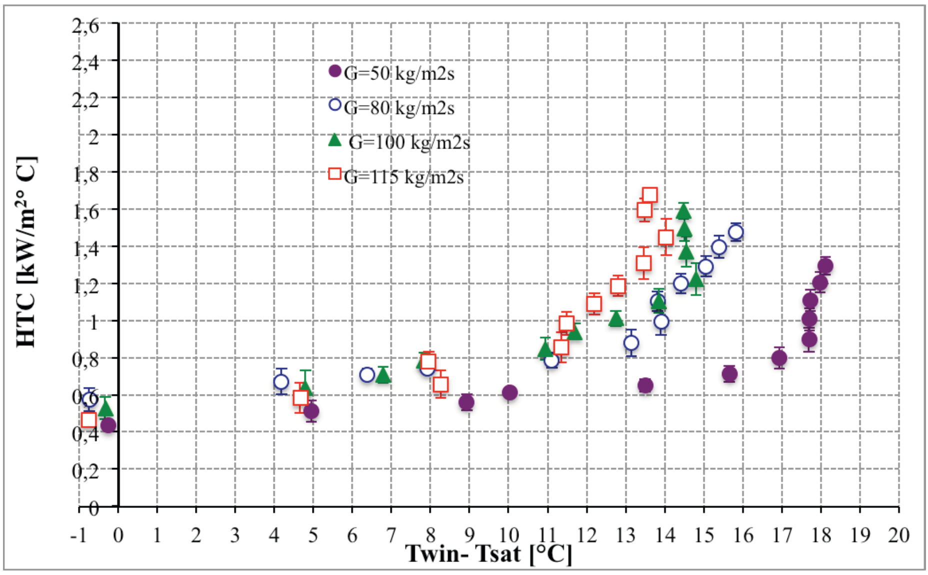

Figure 104 The heat transfer coefficient as function of the wall superheat ΔT_{sh} for the different mass fluxes tested during the experimental campaign with R245fa.

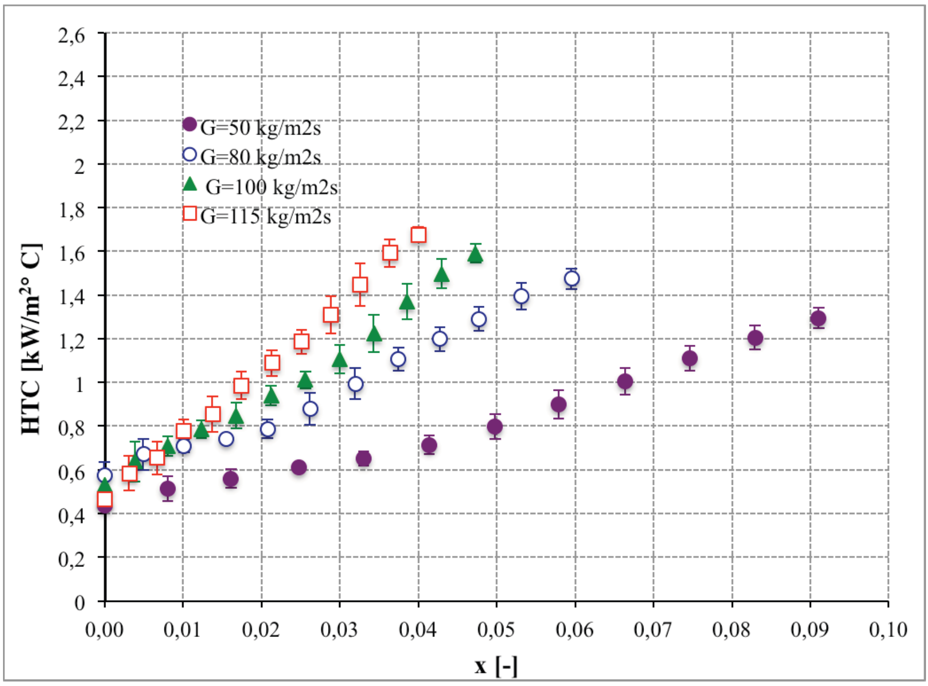

Figure 105 The heat transfer coefficient as function of the vapor quality for the different mass fluxes tested during the experimental campaign with R245fa.

From Figure 103 the HTC, estimated at a fixed heat flux value, increases for increasing value of G for q">5 kW/m^2. From Figure 104 the HTC, estimated at a fixed wall superheat value, increases for increasing value of G for G= 50 kg/m^{2}s and G= 115 kg/m^{2}s while it has a trend that is not regular for the other G values. From the figures above it emerges that the difference in the HTC between the different G values increases a lot passing from the single phase to the two phase region

8.4 R-134a VERSUS R-245fa HEAT TRANSFER COEFFICIENT

The R-245fa HTC obtained for G = 50,80,100 and 115 kg/m^{2}s are compared with those obtained with R-134a for the same mass fluxes. In the next figures there are these comparisons. In order to avoid the overlapping of the experimental data in a same plot, in the next figures the R-245fa and R-134a HTC values are presented for G=50 kg/m^{2}s and G=100 kg/m^{2}s and then for G=80 kg/m^{2}s and G=115 kg/m^{2}s.

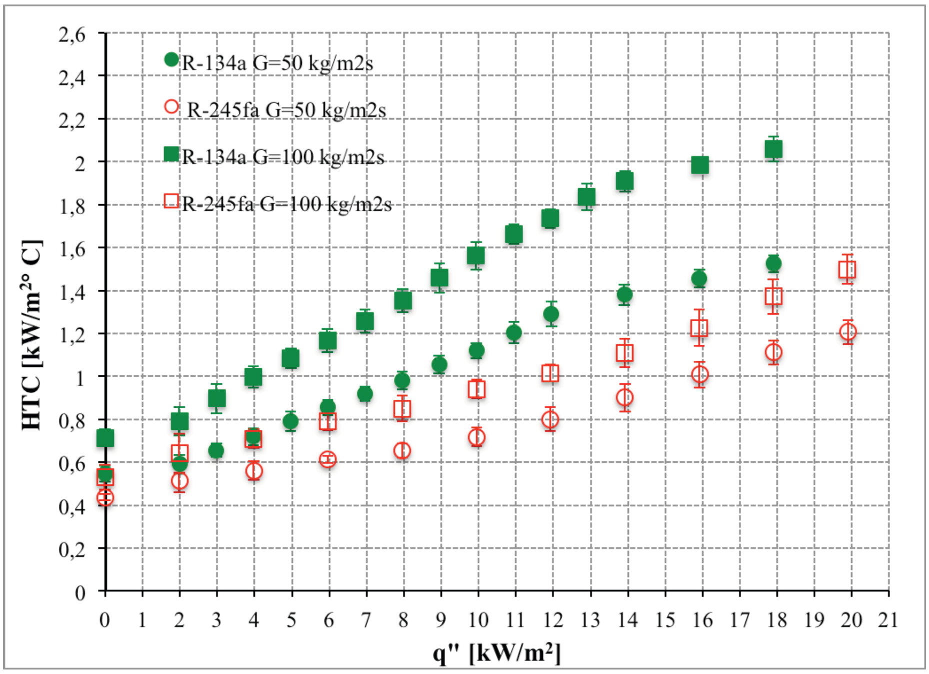

Figure 106 The heat transfer coefficient as function of the heat flux for G=50 kg/m^{2}s and G=100 kg/m^{2}s during the experimental campaign with R-245fa and R-134a.

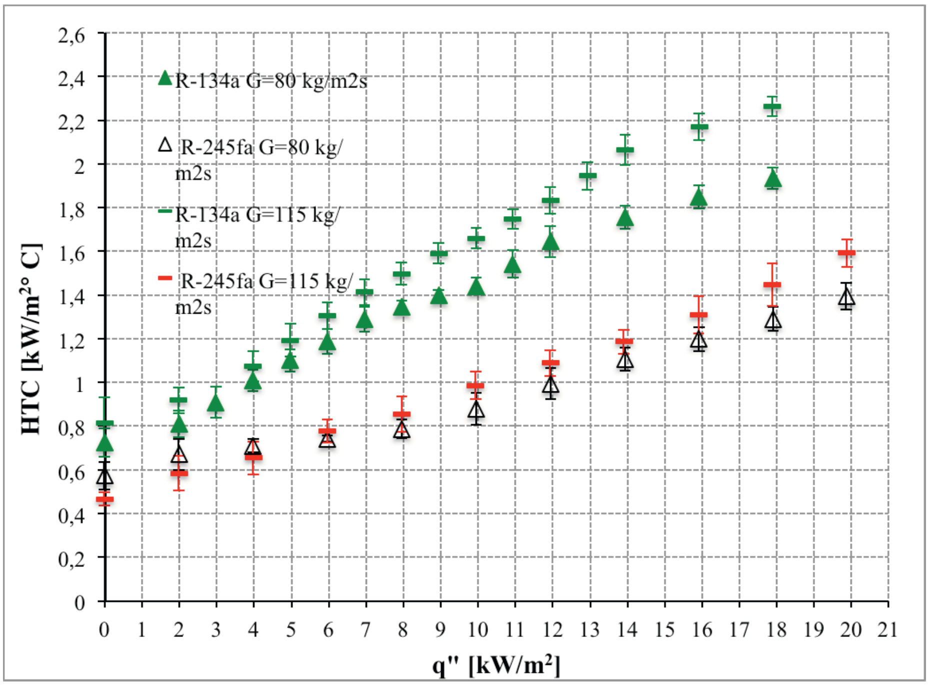

Figure 107 The heat transfer coefficient as function of the heat flux for G=80 kg/m^{2}s and G=115 kg/m^{2}s during the experimental campaign with R-245fa and R-134a.

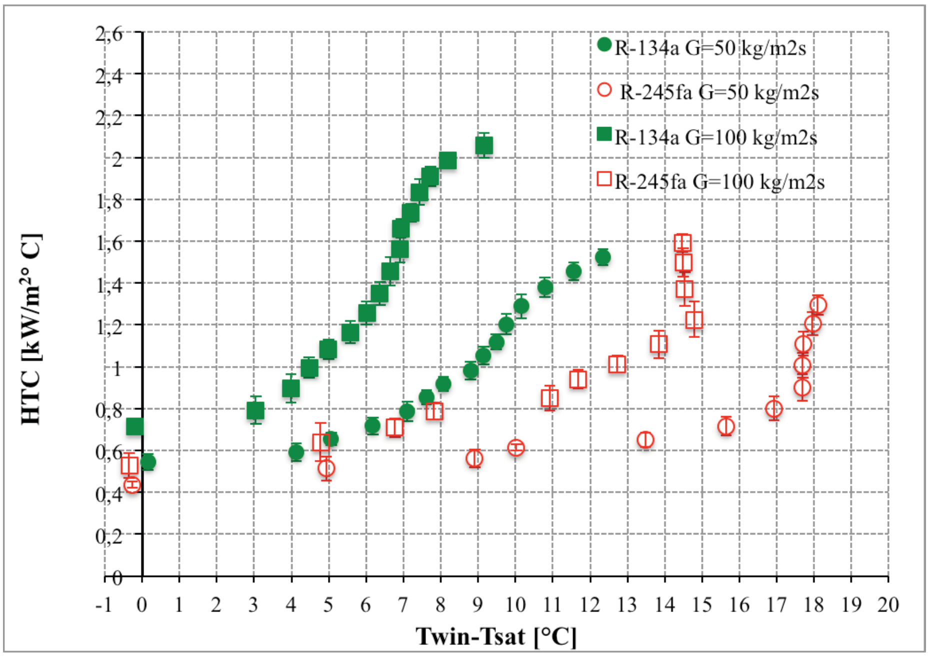

Figure 108 The heat transfer coefficient as function of the wall superheat for G=50 kg/m^{2}s and G=100 kg/m^{2}s during the experimental campaign with R-245fa and R-134a.

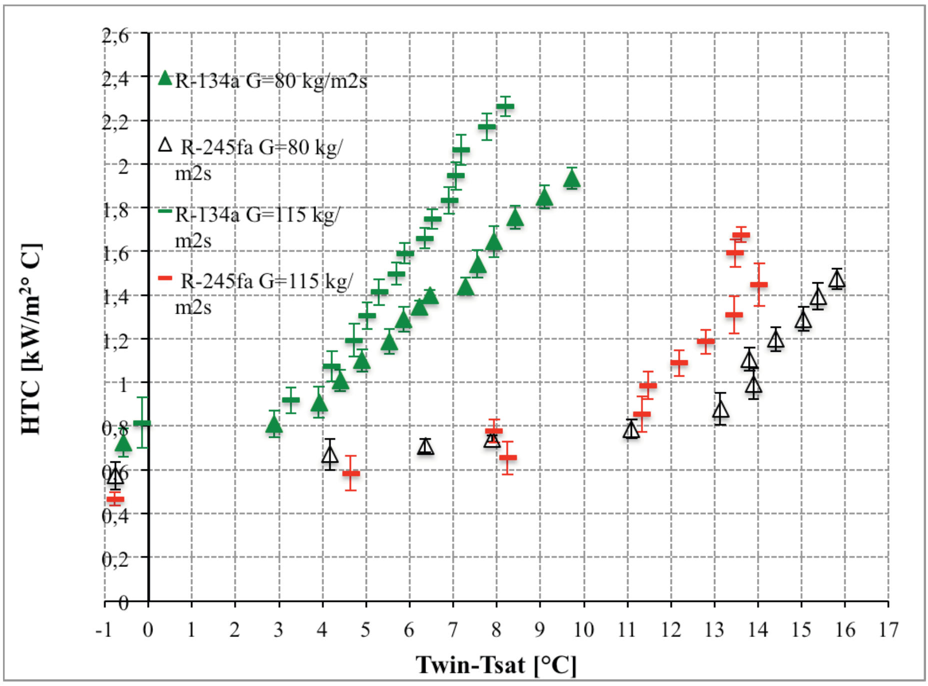

Figure 109 The heat transfer coefficient as function of the wall superheat for G=80 kg/m^{2}s and G=115 kg/m^{2}s during the experimental campaign with R-245fa and R-134a.

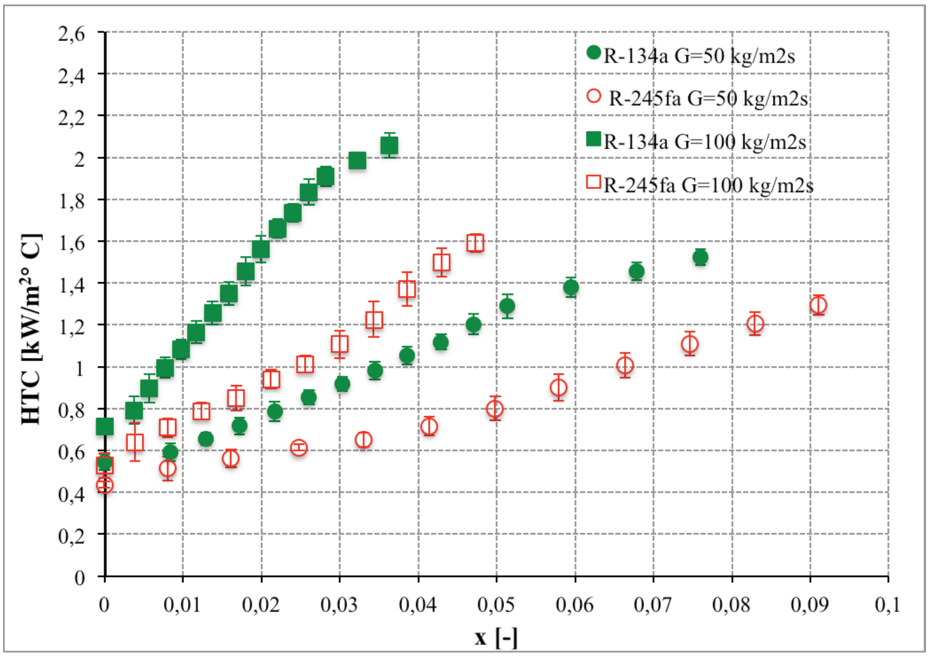

Figure 110 The heat transfer coefficient as function of the vapor quality for G=50 kg/m^{2}s and G=100 kg/m^{2}s during the experimental campaign with R-245fa and R-134a.

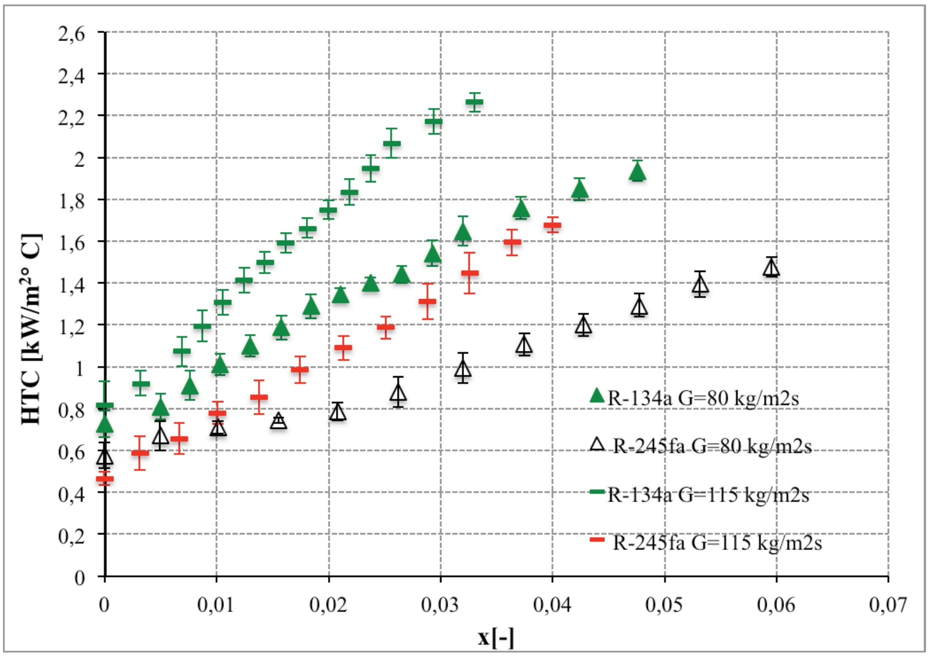

Figure 111 The heat transfer coefficient as function of the vapor quality for G=80 kg/m^{2}s and G=115 kg/m^{2}s during the experimental campaign with R-245fa and R-134a.

8.5 CONCLUSIVE CONSIDERATIONS ON R-245fa EXPERIMENTS

Flow boiling of R-245fa has been experimentally investigated at four different mass flux levels with particular emphasis on the onset of nucleate boiling. These experiments confirm that the nucleation always starts in the upper side of the heater, as already underlined in the previous chapter with R-134a. Then the nucleation starts also in the lower part of the heater. When there is the “upper side” ONB, there is a correspondent temperature drop while no temperature drop is associated to the nucleation from the lower side of the heater. This absence of temperature drop may be associated to the fact that the nucleation from the lower side starts very gradually. Also fort this refrigerant the tests were repeated after the rotation of 180° of the mnichannel and revealed that the boiling always starts in the upper side of the heater.

The heat transfer coefficient was estimated as function of the heat flux and of the wall superheat for all the mass fluxes tested; it emerges that the HTC values increases with G for fixed heat flux values. The general trend of HTC as function of the wall superheat increases with G but this is not true for each wall superheat values.

GENERAL CONSIDERATIONS AND CONCLUSIONS

9.1 CONCLUSIVE CONSIDERATIONS ON PART I

A large number of studies exist on two-phase flow in microchannels and microgravity and this thesis wants to be a critical guide to discover the good points, the uncertainties and the misconceptions of the literature. The boiling flow in microchannels is interesting and complex, and the research needs further experimental data for flow patterns, heat transfer coefficients and for the validation of the boiling models. A new consideration on the effect of wettability is introduced together with the concept of a “drag length”, i.e. a scale to define when the drag forces can move the growing bubbles from a boiling surface. This number could be particularly interesting for microgravity experiments. Critical considerations on the non-dimensional numbers are given, such as for the so-called Kandlikar numbers, K1 and K2. Maps of the dimensionless number ranges spanned by the literature data are given, together with a thorough discussion on the necessity to cover particular unexplored ranges, even with hypergravity experiments. A comparison among the different criteria for the transition from macro to microscale phenomena is proposed, together with the rare considerations on the effect of pressure drop along the tube, the vapour quality and the issue of the microgravity environment. This part of the thesis is discussing the heat transfer mechanism and the strong debate that is stirring the scientific community about the dominant phenomena in flow boiling. Instead of sitting on one side of such dispute, the authors give all the elements to judge and compare, finally considering that there are still experimental uncertainties, misconcepts and weaknesses. A brief and partial excursus in the field of boiling model is helping to address the main problem of understanding the physical mechanisms and the difficulty to compare the different results. A resume of the heat transfer coefficients is tabelled together with the most interesting and feasible results. The open issue of the heat transfer coefficient as a function of the wall temperature is also discussed. A critical review of the flow patterns and the quality of the observations is offered as stimulus for a more homogeneous approach, which may give the impulse for round-robin activities in order to define all the parameters. Finally a comprehensive analysis of the few research work in the field of flow boiling in microgravity conditions is given with the last results, both for flow patterns and for heat transfer mechanisms. A first tempative to resume and compare the results in form of tables is suggested.

A vast amount of comparable and robust data from independent laboratories are necessary to obtain objective results, and better characterized experimental data, including heat transfer data associated to flow pattern visualization and void fraction, are necessary to improve a coherent knowledge in this field. There is still a lack of a systematical evaluation of errors and statistical accuracy in the presentation of the experimental results. The starting of a round-robin activity in many laboratory worldwide using similar and certified test rigs, critically looking at the most important physical parameters, is absolutely urgent.

Defining the right length scale for which a transition between macroscale to microscale phenomena should occur is only a mere exercise of categorization. Noteworthy, the distinction between a macroscale and a microscale regime is misleading, since it could bring to consider a drastical variation of the physical phenomena, which is in fact not occurring until extremely low values of the channel dimension. Instead there is a typical flow pattern, the confined bubble flow, which is the dominant flow mechanism in small channels and in microgravity. Studying for which values and combinations of the dimensionless numbers such pattern appears is the main issue of the present researches. Noteworthy, the meaning of “micro” is here used, as in the present literature, in a broad sense, not strictly linked to the actual size of the channel, but to a change of patterns (and other physical characteristics) linked to a given dimensionless scale. Therefore it is better to speak about different patterns, rather than focusing on a feeble distinction linked to the channel size. Of course, like for single phase flows, going toward very small tubes of few microns size or even nanoscale diameters, the physical phenomena can really change, since many classical hypotheses on continuum, on viscous dissipation and so on, may ceased to be completely valid.

Som necessary future experiments should fill the open questions of the field:

- compare experimental results, having the same Eötvos number, obtained in different gravity conditions;

- collect experimental data having Eo near 1.6 to improve the knowledge of the influence of Eötvos number on the macro to microscale transition;

- study boiling in microgravity and especially hypergravity conditions for channel having dh≤ 3 mm because there is a critical lack of data in the Eötvos number map of the existing literature

- the void fraction should be more largely evalutated since it is one very important and it is still a neglected parameter. Even if its measurement is very difficult, the comparison of the different results appears weak without its proper evaluation.

- future works are necessary to find the threshold for which gravity level does not affect heat transfer and to clarify the increasing or decreasing of heat transfer coefficient in microgravity

- study the effect of drag on bubble detachment and sliding together with the effect of surface wettability both in terrestrial and in microgravity conditions

9.2 CONCLUSIVE CONSIDERATIONS ON PART II

From the experimental analysis on R-134a and on R-245fa, it emerges that the nucleation always starts from the upper side of the heater. Three hypothesis were made by the authors to explain why the nucleation always starts in the upper side of the heater:

- the hydrostatic difference of pressure between the upper side and the lower side of the heater could cause a difference of temperature that could be the responsible for the non uniform boiling;

- the roughness of the glass could influence the beginning of the nucleation;

- the ITO coating could be non homogeneous

These possible causes were investigated and it was found that:

- the hydrostatic difference of pressure in a channel having 4 mm internal diameter at 20°C is forty times lower than the pressure needed to increased the R-134a temperature of 1°C;

- the surface roughness of the glass is in the order of the nanometers and no scratch is optically present on the surface;

- the “upper side” and “lower side” ONB were observed repeating the experiment using eight different ITO heaters in different positions along the tubes. The plasma coating procedure can originate the fact that the ITO thickness presents the same non-uniformity for all the 8 heaters. So the minichannel was rotated of 180° and the experiments were repeated. They showed that the nucleation always start from the upper side of the heater. So the three hypothesis were not succesfull and a further possibility to explore is that, because of presence of gas inside the refrigerants, a number of gas molecules will accumulate in form of nanobubbles on the inner tube surface [117,118, 119]. Due to buoyancy forces the number of such nanobubbles will be higher on the top side with respect to the bottom side. These pre-existing vapor embryos entrapped in the flow and concentrated in the upper side of the mini-channel could be the responsibles for the starting of the nucleation in the upper side; future works would confirm or deny this hypothesis. Saturated heterogeneous non uniform flow boiling of R-134a in horizontal mini-channel has been experimentally investigated at five different mass flux levels (50, 80, 100, 115 and 137 kg/m^{2}s) and the boiling curves evidenced two different temperature drops that flow pattern visualizations showed to be linked to the onset of nucleate boiling from the upper and then the lower side of the heater. Saturated heterogeneous non uniform flow boiling of R-245fa in horizontal mini-channel has been experimentally investigated at four different mass flux levels (50, 80, 100, 115 kg/m^{2}s) and the boiling curves evidenced only one temperature drop associated to the onset of nucleate boiling from the upper side of the heater. Only increasing the heat flux, activating more nucleation sites, the boiling start also in the lower part of the heater but, differently from the R-134a experiments, this is not associated to a temperature drop. The reasons for this different behaviour is still under investigation and, so far, the only qualitative explanation could be that R-245fa boiling starts very gradually from the lower side of the heater and, because of this, is not associated to any temperature drop. The R-134a and R-245fa heat transfer coefficients were estimated as function of the heat flux, of the wall superheat and of the vapor quality for all the mass fluxes tested. It emerges that usually the HTC values increase with G for a fixed heat flux, wall superheat or quality value.

9.3 FUTURE WORKS

This thesis confirm that the boiling process is very intesting and that there are still open issues that must be investigated and clarified:

- in order to better understand the existence of the “upper side” and of the “lower side” ONB, it is important to investigate in detail the distribution of the temperature on the ITO coating. The idea is to map the temperature profile along the circumference of the minichannel using several thermocouples instead of only one and using liquid crystal thermography. With these supplementary data it would be possibile to compare the results with those obtained from an inverse method in steady state;

-it would be interesting to compare the experimental HTC data with correlations available in literature;

- experimental R245fa subcooled boiling would be experimentally investigated in order to study the variation of the wall superheat correspondent to ONB for different subcooling degrees;

- to investigate the gravity effects, the minichannel orientation should be changed;

- after the characterization of the 4 mm internal diameter channel, the experimental tests will be performed with the 1 mm diameter channel.

List of figures

Figure 84 **Boiling curve obtained for G = 100 kg/m^{2}s.**Figure 84 **Boiling curve obtained for G = 100 kg/m^{2}s.**

Figure 90 **Flow patterns associated to point A2, B1, B2 and to q″=16 kW/m^2 for G = 80 kg/m^{2}s.**

Figure 94 **The heat transfer coefficient as function of the vapor quality for the different mass fluxes tested during the experimental campaign with R-134a.**

List of tables

REFERENCES

---

[1] CROWE, C.T., *Multiphase Flow Handbook*, (2006) Taylor and Francis Group.

[2] SHAH, M.M., Chart correlations for saturated boiling heat transfer: equations and further study. *ASHRAE Trans. 88*, Part. I (1982), 185-96.

[3] KANDLIKAR, S.G., Heat transfer mechanisms during flow boiling in microchannels. *Journal of Heat Transfer 126* (2004), 8-16.

[4] RAVIGURURAJAN, T.S., CUTA, J., MCDONALD, C.E., and DROST, M.K., Effect of heat flux on two-phase flow characteristics of refrigerant flows in a micro-channel heat exchanger. *Proceedings of National Heat Transfer Conference*, ASME, HTD-329(7) (1996), 167–178.

[5] LUCIANI, S., BRUTIN, D., LE NILIOT, C., RAHLI, O., and TADRIST, L., Flow boiling in minichannels under normal, hyper and microgravity: local heat transfer analysis using inverse methods. *Journal of Heat Transfer 130* (2008), 101502-1/13.

[6] LUCIANI, S., BRUTIN, D., LE NILIOT, C., TADRIST, L., and RAHLI, O., Boiling heat transfer in a vertical microchannel: local estimation during flow boiling with a non intrusive method. *Multiphase science and technology 21(4)* (2009), 297-328.

[7] HINZE, J.O., Fundamentals of the hydrodynamic mechanism of splitting in dispersion processes. *AIChE Journal 1(3)* (1955), 289-295.

[8] STEINKE, M.E., and KANDLIKAR, S.G., Flow Boiling and Pressure Dropin Parallel Microchannels. *Proceedings of first International Conference on Microchannels and Minichannels*, April 24-25 (2003), Rochester, New York, 567–579.

[9] YAN, Y., and LIN, T., Evaporation Heat Transfer and Pressure Drop of Refrigerant R-134a in a Small Pipe. *Int. J. Heat Mass Transfer 41* (1998), 4183–4194.

[10] WAMBSGANSS, M.W., FRANCE, D.M., JENDRZEJCZYK, J.A., and TRAN, T.N., Boiling Heat Transfer in Horizontal Small-Diameter Tube. *ASME Journal of Heat Transfer 115* (1993), 963–972.

[11] LIN, S., KEW, P.A., and CORNWELL, K., Flow Boiling of Refrigerant R141B in Small Tubes. *Transactions of IchemE 79(A)* (2001), 417-424.

[12] YEN, T.H., KASAGI, N., and SUZUKI Y., Forced Convective Boiling Heat Transfer at Low Mass and Heat Fluxes. *Proceedings of the International Symposium on Compact Heat Exchangers* (2002), Grenoble, Edizioni ETS, 190.

[13] KAMIDIS, D.E., and RAVIGURURAJAN, T.S., Single and Two-Phase Refrigerant Flow in Mini-Channels. *Proceedings of 33rd National Heat Transfer Conference,* August 15-17 (1999) Albuquerque, New Mexico.

[14] HUO, X., CHEN, L., TIAN, Y.S., and KARAYIANNIS, T.G., Flow Boiling and Flow regimes in small diameter tubes. *Applied Thermal Engineering 24 (*2004), 1225-1239.

[15] SHIFERAW, D., HUO, X., KARAYANNIS, T.G., and KENNING, D.B.R., Examination of heat transfer correlations and a model for flow boiling of R134a in small diameter tubes. *International Journal of Heat and Mass Transfer 50* (2007), 5177-5193.

[16] CHEN, L., TIAN, Y.S., and KARAYIANNIS, T.G., The effect of tube diameter on vertical two-phase flow regimes in small tubes. *Int. J. Heat Mass Transfer 49* (2006), 4220-4230.

[17] ULLMANN, A., and BRAUNER, N., The prediction of flow pattern maps in minichannels. *Multiphase Science and Technology 19(1)* (2007), 49-73.

[18] OHTA, H., Review of reduced gravity boiling heat transfer: Japanese research. *J. Jpn. Soc. Microgravity Appl. 20(4)* (2003), 272-285.

[19] OHTA, H., Experiments on microgravity boiling heat transfer by using transparent heaters. *Nuclear Engineering and Design 175* (1997), 167-180.

[20] CELATA, G.P., CUMO. M., GERVASI, M., and ZUMMO. G., Flow pattern analysis of flow boiling in microgravity. *Multiphase Science and Technology 19*(2) (2007), 183-210.

[21] CELATA, G.P., and ZUMMO, G., Flow boiling heat transfer in microgravity: recent progress. *Multiphase Science and Technology 21(3)* (2009), 187-212.

[22] MORINI, G.L., Single- phase convective heat transfer in laminar and transitional regime in microchannels. *ECI International conference on Heat Transfer and Fluid Flow in Microscale,* September 21-26 (2008), Whistler.

[23] CELATA, G.P., LORENZINI, M., MCPHAIL, S.J., MORINI, G.L., and ZUMMO, G., Experimental analysis of liquid forced convection in rough microtubes. *Proc. of 5th Eurotherm European Thermal Science Conference,* May 19-22 (2008), Eindhoven.

[24] KANDLIKAR, S.G., *Two-phase flow patterns, pressure drop and heat transfer during boiling in minichannel and microchannel flow passages of compact heat exchanger.* Compact heat exchangers and enhancement technology for the process Industries, (2001), Begell house, New York, 319-334.

[25] THOME, J.R., Boiling in microchannels: a review of experiment and theory. *International Journal of heat and Fluid Flow 25* (2004), 128-139.

[26] THOME, J.R., DUPONT, V., and JACOBI, A.M., Heat transfer model for evaporation in microchannels, part I: presentation of the model. *International Journal of Heat and Mass Transfer 47* (2004), 3375-3385.

[27] THOME, J.R., *Wolverine Engineering Data Book III.*

[28] KEW, P.A., and CORNWELL, K., Correlations for the prediction of boiling heat transfer in small diameter channels. *Applied Thermal Engineering 17* (1997), 705-715.

[29] RIBATSKI, G., and WOJTAN, L., and THOME, J.R., An analysis of experimental data and prediction methods for two-phase frictional pressure drop and flow boiling heat transfer in micro-scale channels. *Experimental Thermal and Fluid Science 31* (2006), 1–19.

[30] LI, J.M., and WANG, B.X., Size effect on two-phase regime for condensation in micro/mini tubes. *Heat transfer asian res. 32* (2003), 65-71.

[31] CHENG, P., and WU, H.Y., Mesoscale and Microscale Phase Change Heat Transfer. *Advances in Heat Trasfer 39* (2006), 461-563.

[32] HARICHIAN, T., and GARIMELLA, S., A comprehensive flow regime map for microchannel flow boiling with quantitative transition criteria. *International Journal of Heat and Mass Transfer 53* (2010), 2694-2702.

[33] LOCKHART, R.W., and MARTINELLI, R.C., Proposed correlation of data for isothermal two-phase, two component flow in pipes. *Chem. Eng.Prog. 45* (1949), 39–48.

[34] CHISHOLM, D., A theoretical basis for the Lockhart–Martinelli correlation for two-phase flow. *Int. J. Heat Mass Transfer 10* (1967) 1767–1778.

[35] REVELLIN, R., and THOME, J.R., A new type of diabatic flow pattern map for boiling heat transfer in microchannels. *Journal of Micromechanics and Microengineering 17* (2007), 788-796.

[36] VADGAMA, B., and HARRIS, D.K., Measurements of the contact angle between R134a and both aluminum and copper surfaces. *Experimental Thermal and Fluid Science 31* (2007), 979-984.

[37] GAO, L., and MCCARTHY, T.J., Contact Angle Hysteresis Explained. *Langmuir 22* (2006), 6234-6237.

[38] CELATA, G.P., Single and two-phase flow heat transer in micropipes. *5th European Thermal-Sciences Conference* (2008), The Nederlands.

[39] LEE, J., and MUDAWAR, I., Two-phase flow in high-heat-flux micro-channel heat sink for refrigeration cooling applications: Part II-heat transfer characteristics. *International Journal of Heat and Mass Transfer 48* (2005), 941-955.

[40] BAO, Z.Y., FLETCHER, D.F., and HAYNES, B.S., Flow boiling heat transfer on Freon R11 and HFCFC123 in narrow passages. *International Journal of Heat and Mass Transfer 43* (2000), 3347-3358.

[41] LIN, S., KEW, P.A., and CORNWELL, K., Two-phase heat transfer to a refrigerant in a 1 mm diameter tube. *6th UK Heat Transfer Conference* (1999), Edinburgh.

[42] YEN, T.H., SHOJI, M., TAKEMURA, F., SUZUKI, Y., and KASAGI, N., Visualization of convective boiling heat transfer in single microchannels with different shaped cross-sections. *International Journal of Heat and Mass Transfer 49* (2006), 3884–3894.

[43] JACOBI, A.M., and THOME, J.R., Heat transfer model for evaporation of elongated bubble flows in microchannels. *J. Heat Transfer 124 (*2002), 1131–1136.

[44] CHENG, P., WANG, G., and QUAN, X., Recent work on boiling and condensation inmicrochannels. *ASME J. Heat Transfer 131(4)* (2009).

[45] HARIRCHIAN, T., and GARIMELLA, S.V., The critical role of channel cross-sectional area in microchannel flow boiling heat transfer. *Int. J. Multiphase flow 35* (2009), 904-913.

[46] HUH, C., and KIM, M.H., Pressure Drop, Boiling Heat Transfer and Flow Patterns during Flow Boiling in a Single Microchannel. *Heat Transfer Engineering 28(8–9)* (2007), 730-737.

[47] REVELLIN, and R., THOME, J.R., Experimental investigation of R-134a and R-245fa two-phase flow in microchannels for different flow conditions. *ECI International Conference on Heat Transfer and Fluid Flow in Microscale*, 25-30 September (2005), Castelvecchio Pascoli, Italy.

[48] HARIRCHIAN, T., and GARIMELLA, S.V., Boiling heat transfer and flow regimes in microchannels - a comprehensive understanding. *Journal of Electronic Packaging 133* (2011), 011001-1/10.

[49] DUPONT, V., THOME, J.R., and JACOBI, A.M., Heat transfer model for evaporation in microchannels, part II: comparison with the database. *International Journal of Heat and Mass Transfer 47* (2004), 3387-3401.

[50] REVELLIN, R., DUPONT, V., URSENBACHER, T., THOME, J.R., and ZUN, I., Characterization of diabatic two-phase flows in

microchannels: Flow parameter results for R-134a in a 0.5 mm channel. *Int. J. Multiphase Flow 32* (2006), 755-774.

[51] AGOSTINI, B., and THOME, J.R., Comparison of an extended database for flow boiling heat transfer coefficients in multi-microchannels elements with the three-zone model. *ECI Heat Transfer and Fluid Flow in Microscale*, Sept. 25-30 (2005), Castelvecchio Pascoli, Italy.

[52] HARIRCHIAN, T., and GARIMELLA, S., Flow regime-based modeling of heat transfer and pressure drop in microchannel flow boiling. *International Journal of heat and Mass Transfer 55* (2012), 1246-1260.

[53] COOPER, M.G., Saturated nucleate pool boiling- a simple correlation. *IChemE Symposium Series 86(2), 1st UK National Heat Transfer Conference* (1984), 785-793.

[54] WHAN NA, Y., and CHUNG, J.N., Two-phase annular flow and evaporative heat transfer in a microchannel. *International Journal of Heat and Fluid Flow 32* (2011), 440-450.

[55] CIONCOLINI, A., and THOME, J.R. Algebraic turbulence modeling in adiabatic and evaporating annular two-phase flow. *International Journal of Heat and Fluid Flow 32* (2011), 805-817.

[56] CIONCOLINI, A., and THOME, J.R., Prediction of the entrained liquid fraction in vertical annular gas–liquid two-phase flow. *Int. J. Multiphase Flow 36-4* (2010), 293-302.

[57] CIONCOLINI, A., THOME, J.R., and LOMBARDI, C., Unified macro-to-microscale method to predict two-phase frictional pressure drops of annular flows. *Int. J. Multiphase Flow 35-12* (2009), 1138–1148.

[58] THOME, J.R., State of the art overview of boiling and two-phase flows in microchannels. *Heat transfer engineering 27-9* (2006), 4-19.

---

[59] SHIFERAW, D., KARAYANNIS, T.G., and KENNING, D.B.R., A comparison with the three-zone model for flow boiling heat transfer in small diameter tubes. *13th International heat transfer conference* (2006), Sydney, Australia.

[60] SHIFERAW, D., KARAYANNIS, T.G., and KENNING, D.B.R., Flow boiling in a 1.1 mm tube with R134a: Experimental results and comparison with model. *International Journal of Thermal Sciences 48* (2009), 331-341.

[61] CONSOLINI, L., and THOME, J.R., A heat transfer model for evaporation of coalescing bubbles in micro-channel flow. *International Journal of Heat and Fluid Flow 31* (2010), 115-125.

[62] LIU, T.J., TIAN, Y., and PENG, X.F., Bubble characteristics during boiling microchannels. *3rd International Conference on Microchannels and Minichannels,* June 13-15 (2005), Toronto, Ontario, Canada.

[63] ONG, C.L., THOME, J.R., Flow boiling heat transfer of R134a, R236fa and R245fa in a horizontal 1.030 mm circular channel. *Experimental Thermal and Fluid Science 33* (2009), 651-663.

[64] LAZAREK, G.M., and BLACK, S.H., Evaporative heat transfer, pressure drop and criticalheat flux in a small vertical tube with R-113. *International Journal of Heat and Mass Transfer 25-7* (1982), 945-960.

[65] TRAN, T.N., WAMBSGANSS, M.W., and FRANCE, D.M., Small circular- and rectangular channel boiling with two refrigerants. *International Journal of Multiphase Flow 22-3* (1996), 485-498.

[66] KANDLIKAR, S.G., and BALASUBRAMANIAN, P., An extension of the flow boiling correlation to transition, laminar and deep laminar flows in mini-channels and micro-channels. *Heat Transfer Engineering 25-3* (2004), 86–93.

[67] ZHANG, W., HIBIKI, T., and MISHIMA, K., Correlation for flow boiling heat transfer in mini-channels. *International Journal of Heat and Mass Transfer 47* (2004), 5749-5763.

[68] BERTSH, S.S., GROLL, E.A., and GARIMELLA, S.V., Review and comparative analysis of studies on saturated flow boiling in small channels. *Nanoscale and Microscale Thermophysical Engineering 13-3* (2008), 187-227.

[69] BERTSCH, S.S., GROLL, E.A., and GARIMELLA, S.V., Effects of heat flux, mass flux, vapor quality, and saturation temperature on flow boiling heat transfer in microchannels. *Int. J. Multiphase flow 35* (2009), 142-154.

[70] CONSOLINI, L., and THOME, J.R., Micro-channel flow boiling heat transfer of R-134a, R-236fa and R-245fa. *Microfluid Nanofluid 6* (2009), 731-746.

[71] DUPONT, V., and THOME, J.R., Evaporation in microchannels: influence of the channel diameter on heat transfer. *Microfluid nanofluid 1* (2005), 119-127.

[72] LIN, S., KEW, P.A., and CORNWELL, K., Two-phase heat transfer to a refrigerant in a 1 mm diameter tube. *Int. J. Refrigeration 24* (2001), 51-56.

[73] KANDLIKAR, S.G., MIZO, V., CARTWRIGHT, M., and IKENZE, E., Bubble nucleation andgrowth characteristics in subcooled flow boiling of water. *ASME National Heat Transfer Conference 4* (1997), 11-18.

[74] ZEITOUN, O., and SHOUKRI, M., Bubble behavior and mean diameter in subcooled flow boiling. *ASME J. Heat Transfer 118* (1996), 110-116.

[75] CHANG, S.H., BANG, I.C., and BAEK, W.P., A photographic study on the near-wall bubble behavior in subcooled flow boiling. *Int. J. Thermal Sci. 41* (2002), 609-618.

[76] YIN, C.P., YAN, Y.Y., LIN, T.F., and YANG, B.C., Subcooled flow boiling heat transfer of R-134a and bubble characteristics in a horizontal annular duct. *Int. J. Heat MassTransfer 43* (2000), 1885-1896.

[77] CHEN, C.A., CHANG, W.R., LI, K.W., LIE, Y.M., and LIN, T.F., Subcooled flow boiling heat transfer of R-407C and associated bubble characteristics in a narrow annular duct. *International Journal of Heat and Mass Transfer 52* (2009), 3147-3158.

[78] ZHUAN, R., and WANG, W., Simulation of subcooled flow boiling in a micro-channel. *International Journal of Refrigeration 34* (2011), 781-795.

[79] CELATA, G.P., CUMO, M., and MARIANI, A., Experimental evalutation of the onset of subcooled flow boiling at high liquid velocity and subcooling. *Int. J. Heat Mass transfer 40(12)* (1997), 2879-2885.

[80] HARIRCHIAN, T., and GARIMELLA, S.V., Effects of channel dimension, heat flux, and mass flux on flow boiling regimes in microchannels. *Int. J. Multiphase flow 35* (2009), 349-362.

[81] CORNWELL, K., and KEW, P.A., Boiling in small Channels. *Proceedings of Conference on Energy Efficiency in Process Technology* (1992), Elsevier, 624-638.

[82] LIN, S., KEW, P.A., and CORNWELL, K., Two-phase Flow regimes and heat transfer in small tubes and channels. *Proceedings of 11th international heat transfer conference 2* (1998), Kyongju, Korea, 45-50.

[83] REVELLIN, R., and THOME, J.R., Experimental investigation of R-134a and R-245fa two-phase flow in microchannels for different flow conditions. *International Journal of Heat and Fluid Flow 28(1)* (2007), 63-71.

[84] ZHANG, L., KOO, J.M., JIANG, L., ASHEGHI, M., GOODSON K.E., SANTIAGO, J.G. et al. Measurements and modeling of two-phase flow in microchannels with nearly constant heat flux boundary conditions. *Journal of Microelectromechanical systems 11(1)* (2002), 12-19.

[85] REVELLIN, R., AGOSTINI, B., and THOME, J.R., Elongated bubbles in microchannels, Part II: experimental study and modeling of bubble collision. *Int. J. Multiphase flow 34* (2008), 602-613.

[86] AGOSTINI, B., REVELLIN, R., and THOME, J.R., Elongated bubbles in microchannels, Part I: experimental study and modeling of elongated bubble velocity. *Int. J. Multiphase flow 34* (2008), 590-601.

[87] CELATA, G.P., Flow boiling heat transfer in microgravity: recent results. *Microgravity Science Technology vol XIX-3/4* (2007), 13-17.

[88] MCQUILLAN, K.W., and WHALLEY, P.B., Flow patterns in vertical two-phase flow. *Int. J. Multiphase Flow 11* (1985), 161-175.

[89] COLIN, C., FABRE, J.A., and DUKLER, A.E., Gas-Liquid flow at microgravity conditions-I. Dispersed bubble and slug flow. *Int. J. Multiphase Flow 17* (1991), 533-544.

[90] DUKLER, A.E., FABRE, J.A., MCQUILLEN, J.B., and VERNON, R., Gas-Liquid flow at microgravity conditions: flow patterns and their transitions. *Int. J. Multiphase Flow 14* (1988), 389-400.

[91] ZHAO, L., and REZKALLAH, K.S., GA-Liquid flow patterns at microgravity conditions. *Int. J. Multiphase flow 19* (1993), 751-763.

[92] JAYAWARDENA, S.S., BALAKOTAIAH, V., and WITTE, L.C., Pattern transition maps for microgravity two-phase flows. *AIChE J. 43* (1997), 1637-1640.

---

[93] RITE, R.W., and REZKALLAH, K.S., Heat transfer in forced-convective two-phase flows under microgravity conditions: analysis. *Multiphase Science and Technology 13* (2001), 113-137.

[94] PAPELL, S.S., An instability effect on two-phase heat transfer for subcooled water flowing under conditions of zero gravity. *American Rocket Society 17th Annual Meeting and Space Flight Exposition* (1962).

[95] FELDMANIS, C.J., Pressure and temperature changes in closed loop forced convection boiling and condensing processes under zero gravity conditions. *Institute of environmental sciences 1966 annual technical meeting proceedings*.

[96] REINARTS, T.R., BEST, F.R., and HILL, W.S., Definition of condensation two- phase flow behaviors for spacecraft design. *AIP conference, Proc. No. 246* (1992), M. S. EL-Genk and M.D. Hoover, eds, American Institute of Physics, New York 1, 1216-1225

[97] OHTA, H., FUKIYAMA, H., INOUE, K., YAMADA, Y., ISHIKURA, S., and YOSHIDA, S., Microgravity flow boiling in a transparent tube. *10th international heat transfer conference* (1994) Brighton (England).

[98] OHTA, H., Microgravity heat transfer in flow boiling. *Advances in heat transfer vol.37* (2003).

[99] ONG, C.L., THOME J.R., Macro-to-microchannel transition in two-phase flow: Part 1 – Two-phase flow patterns and film thickness measurements, *Experimental Thermal and Fluid Science 35* (2011) 37–47.

[100] DALL’OLIO, S., MARENGO, M., Boiling of R134a inside a glass minichannel. A new statistical approach of flow pattern characterization based on flow visualization, *Int. J. Heat Mass Transfer*, *Vol. 55* (2012), 1048-1065.

[101] DALL’OLIO, S., Boiling of R134a inside a glass minichannel. A new approach of flow pattern characterization based on flow visualization, *Doctoral Dissertation* (2009), Università degli studi di Bergamo.

[102] GHIAASIAAN, S.M., CHEDESTER, R.C. Boiling incipience in microchannels. *Int. J. Heat Mass Transfer,* 45 (2002), 4599–4606.

[103] BANG, C., CHANG, S. H., BAEK, W.P. Visualization of the subcooled flow boiling of R-134a in a vertical rectangular channel with an electrically heated wall. *Int. J. of Heat and Mass Transfer, 47* (2004), 4349–4363.

[104] CALLIZO, C.M., PALM, B. P., OWHAIB, W. Subcooled flow boiling of R-134a in vertical channels of small diameter. *International Journal of Multiphase Flow*, 33 (2007), 822– 832.

[105] LIU, D., LEE, P.S., GARIMELLA, S. V. Prediction of the onset of nucleate boiling in microchannel flow. *International Journal of Heat and Mass Transfer, 48* (2005), 5134–5149.

[106] HONG, G., YAN, X., YANG, Y.H., LIU, S., HUANG, Y.P. Experimental study on onset of nucleate boiling in narrow rectangular channel under static and heaving conditions. *Annals of Nuclear Energy, 39* (2012), 26–34.

[107] COPETTI, J.B., MACAGNAN, M.H., ZINANI, F., KUNSLER, N.L.F. Flow boiling heat transfer and pressure drop of R-134a in a mini tube:an experimental investigation, *Experimental Thermal and Fluid Science, vol. 35* (2011), 636-644.

[108] KANDLIKAR, S.G., BALASUBRAMANIAN, P., An extension of the flow boiling correlation to transition, laminar, and deep laminar flows in minichannels and microchannels, *Heat Transfer Engineering* , vol. 25 (2004), 86–93.

[109] SAISORN, S., KAEW-ON, J., WONGWISES, S., Two-phase flow of R-134a refrigerant during flow boiling through a horizontal circular mini-channel, *Exp. Therm. Fluid Sci., vol. 35* (2011), 887–895

[110] SAISORN, S., KAEW-ON, J., WONGWISES, S., An experimental investigation of flow boiling heat transfer of R-134a in horizontal and vertical mini-channels, *Experimental Thermal and Fluid Science* (2013).

[111] DA SILVA LIMA, R.J., QUIBÉN J.M., THOME J.R., Flow boiling in horizontal smooth tubes: New heat transfer results for R-134a at three saturation temperatures, *Applied Thermal Engineering 29* (2009), 1289-1298.

[112] TIBIRIÇÁ, C.B., RIBATSKI, G., Flow boiling heat transfer of R134a and R245fa in a 2.3 mm tube, *International Journal of Heat and Mass Transfer* 53 (2010), 2459–2468.

[113] LIU, Z., WINTERTON, R.H.S., A general correlation for saturated and subcooled flow boiling in tubes and annuli based on a nucleate pool boiling equation, *Int. J. Heat Mass Transfer* 34 (1991), 2759–2766.

[114] ZHANG, W., HIBIKI, T., MISHIMA, K., Correlation for flow boiling heat transfer in mini-channels, *Int. J. Heat Mass Transfer* 47 (2004), 5749–5763.

[115] SAITOH, S., DAIGUJI, H. HIHARA, H., Correlation for boiling heat transfer of R-134a in horizontal tubes including effect of tube diameter, *Int. J. Heat Mass Transfer* 50 (2007), 5215–5225.

[116] AGOSTINI, B., THOME, J.R., FABBRI, M., MICHEL, B., CALMI, D., KLOTER, U., High heat flux flow boiling in silicon multi-microchannels –Part II: Heat transfer characteristics of refrigerant R245fa, *International Journal of Heat and Mass Transfer* 51 (2008), 5415–5425.

[117] SEDDON, J.R.T., ZANDVLIET, H.J.W., LOHSE, D., Knudsen Gas Provides Nanobubble Stability, *Phys. Rev. Lett.*, *107* (2011), 116101.

[118] SEDDON, J.R.T., KOOIJ, E.S., POELSEMA, B., ZANDVLIET, H.J.W., LOHSE, D., Surface Bubble Nucleation Stability , *Phys. Rev. Lett. 106* (2011), 056101.

[119] CHAN, C.U., OHL, C.D., Surface Nanobubble Nucleation Visualized with TIRF Microscopy, *arXiv* (2012), 1204.2633.